

# **Properties of laser-crystallized polycrystalline SiGe thin films**

vorgelegt von  
Diplom-Physiker  
Moshe Weizman  
aus Jerusalem

Von der Fakultät II - Mathematik und Naturwissenschaften  
der Technischen Universität Berlin  
zur Erlangung des akademischen Grades  
Doktor der Naturwissenschaften  
Dr. rer. nat.

genehmigte Dissertation

Promotionsausschuss:

Vorsitzender: Prof. Dr. rer. nat. Christian Thomsen  
Erstgutachter: Prof. Dr. rer. nat. Michael Kneissl  
Zweitgutachter: Dr. rer. nat. Norbert H. Nickel

Tag der wissenschaftlichen Aussprache: 06.06.2008

Berlin 2008  
D 83



# Zusammenfassung

Im Rahmen dieser Arbeit wurden die strukturellen, elektrischen und optischen Eigenschaften von dünnen laserkristallisierten polykristallinen  $\text{Si}_{1-x}\text{Ge}_x$ -Filmen mit  $0 < x < 1$  untersucht. Die wichtigsten Ergebnisse und Schlussfolgerungen sind im Folgenden zusammengefasst:

- Die Laserkristallisation von dünnen amorphen  $\text{Si}_{1-x}\text{Ge}_x$ -Filmen mit  $0.3 < x < 0.7$  kann zur Ausbildung einer selbstorganisierten Hügel- bzw. Wellenstruktur auf der Oberfläche der Filme führen, die direkt mit einer periodischen Variation der Legierungszusammensetzung verknüpft ist. Die erhöhten Bereiche der Hügel und Wellen sind dabei mit Ge angereichert, wohingegen die tiefer liegenden Bereiche an Ge verarmt sind.
- Nach einem Laserpuls zeigen die amorphen SiGe-Proben eine Wellenstruktur, aus der sich mit zunehmender Anzahl von Laserpulsen eine Hügelstruktur entwickelt. Die vom Ge-Gehalt, der Schichtdicke und der Energieflussdichte abhängige Periodizitätslänge der Strukturen beträgt nach einem Laserpuls 0.3 bis 1.1  $\mu\text{m}$  und nimmt mit zunehmender Anzahl an Laserpulsen stark zu. Des Weiteren wurde keine Korrelation zwischen der Periodizitätslänge und der Korngröße, die in den Schichten typischerweise 0.1  $\mu\text{m}$  betrug, gefunden.
- Als Hauptmechanismus der Strukturbildung wird eine Instabilität an der Grenzfläche zwischen fester und flüssiger Phase während der Erstarrung vorgeschlagen. Berechnungen für  $\text{Si}_{1-x}\text{Ge}_x$  mit  $x < 0.5$  entsprechend der Mullins-Sekerka-Theorie zeigen, dass für Kristallisationsgeschwindigkeiten im Bereich von 0.02 bis 3 m/s und hinreichendem Ge-Gehalt der Legierung eine Instabilität des Systems zu erwarten ist. Dieses Ergebnis stimmt gut mit den in dieser Arbeit für SiGe-Filme auf Glas experimentell ermittelten Kristallisationsgeschwindigkeiten überein. Darüber hinaus kann mit Hilfe dieses Modells auch das Verschwinden der Selbstorganisation bei SiGe-Filmen auf Edelstahl und auf molybdänbeschichtetem Glas mit der höheren thermischen Leitfähigkeit dieser Substrate und der damit verbundenen höheren Kristallisationsgeschwindigkeit erklärt werden.
- Die Untersuchung von Defekten mittels Elektronenspinresonanz (ESR) zeigte, dass dünne laserkristallisierte Poly- $\text{Si}_{1-x}\text{Ge}_x$ -Filme mit  $0 < x < 0.84$  unabhängig vom verwendeten Kristallisationsverfahren und dem Ge-Gehalt der Legierung eine Dangling-Bond-

Konzentration von etwa  $N_s = 4 \times 10^{18} \text{ cm}^{-3}$  haben. Die Defektdichte von thermisch kristallisierten SiGe-Filmen war dagegen geringer und betrug nur  $N_s = 7 \times 10^{17} \text{ cm}^{-3}$ .

- Ge-reiche laserkristallisierte Poly-SiGe-Filme zeigten in einigen Fällen ein nicht typisches, breites Elektrisches-Dipol-Spin-Resonanz-Signal (EDSR), das von einer nahezu temperaturunabhängigen elektrischen Leitfähigkeit im Bereich 20 – 100 K begleitet wurde. Die Analyse der Winkelabhängigkeit des EDSR-Signals deutet darauf hin, dass dieser Effekt von einer großen metallischen Leitfähigkeit entlang der Korngrenzen hervorgerufen wird.
- Die Korngrenzenleitung ist mit großer Wahrscheinlichkeit auf Dangling-Bond-Defekte und nicht auf extrinsische Verunreinigungen zurückzuführen. Metallische Leitung tritt dabei für Dangling-Bond-Defektkonzentrationen oberhalb einer kritischen Größe von  $N_C \approx 10^{18} \text{ cm}^{-3}$  auf. Unterhalb dieses kritischen Wertes nimmt die Korngrenzenleitfähigkeit stark ab, findet aber wahrscheinlich weiterhin mittels Hopping über lokalisierte Defektzustände statt. Das Auftreten einer metallischen Leitfähigkeit vorzugsweise bei Ge-reichen laserkristallisierten Poly-SiGe Proben wird als intrinsische Eigenschaft von Ge im Vergleich zu Si angesehen und nicht auf die Details der Korngrenzenstruktur zurückgeführt.
- Optische Untersuchungen an laserkristallisierten Poly-Si<sub>1-x</sub>Ge<sub>x</sub>-Filmen mit  $x \geq 0.5$  zeigen ein für ungeordnetes SiGe typisches Absorptionsverhalten, welches auf eine vorwiegend an den Korngrenzen stattfindende Absorption hindeutet. Beim laserkristallisierten Poly-Si<sub>0.5</sub>Ge<sub>0.5</sub>-Film wurde zudem ein Absorptionspeak innerhalb der Bandlücke beobachtet, der einem optischen Übergang zwischen  $D^+/D^0$  Dangling-Bond-Zuständen und dem Leitungsbandminimum zugeordnet werden kann.
- Die Nachbehandlung der laserkristallisierten Poly-SiGe-Filme in einem Wasserstoffplasma führt zu einer bemerkenswerten Änderung der Materialeigenschaften. Auf der einen Seite wird ein Übergang von metallischer Leitfähigkeit zu isolierendem Verhalten, sowie eine Reduktion des ESR-Signals und der Absorption unterhalb der Bandlücke beobachtet, was auf eine Passivierung der Dangling-Bond-Defekte an den Korngrenzen hindeutet. Auf der anderen Seite deutet die Abnahme der Photoleitfähigkeit auf die Bildung einiger neuer, elektrisch aktiver Defekte hin. Als mögliche Defekte werden hierbei zusammenhängende  $\text{H}_2^*$ -Komplexe, so genannte Platelets, vorgeschlagen.

# Contents

<b>1</b>	<b>Introduction .....</b>	<b>7</b>
<b>2</b>	<b>Experimental methods .....</b>	<b>11</b>
2.1	Sample preparation.....	11
2.2	Characterization methods.....	14
<b>3</b>	<b>Experimental results .....</b>	<b>19</b>
3.1	Laser-induced self organization in SiGe thin films.....	19
3.1.1	Pattern formation.....	19
3.1.2	Melting and solidification.....	26
3.1.3	Potential for cold cathode applications.....	29
3.2	Defect characterization.....	31
3.2.1	Electron spin resonance measurements.....	31
3.2.2	Electrical conductivity and hydrogen post-treatment.....	38
3.2.3	Optical absorption .....	44
<b>4</b>	<b>Discussion.....</b>	<b>49</b>
4.1	Pattern formation based on the Mullins-Sekerka instability.....	49
4.2	Defects and electrical transport.....	57
4.2.1	Transport along grain boundaries.....	57
4.2.2	Hydrogen-induced defects.....	66
<b>5</b>	<b>Summary.....</b>	<b>71</b>
<b>6</b>	<b>References.....</b>	<b>73</b>

**List of abbreviations**

**List of author publications**

**Acknowledgements**



# 1 Introduction

In the last 30 years the field of laser crystallization and laser annealing of semiconductors has opened new possibilities for crystal growth, alloying, and novel structure formation. The use of laser processing techniques offers a unique temporal and spatial control of the heat flow into the material. Different beam delivery systems can be used to achieve a desired beam shape and laser fluence profile, which significantly influence the resulting microstructure of the material [1, 2, 3]. A variety of both continuous-wave and pulsed lasers, ranging from excimer lasers emitting light in the ultra violet (UV) range to Nd:YAG lasers operating in the infra red (IR) range at a wavelength of 1064 nm, have been used for laser processing. Depending on the laser being used, cooling rates can vary over many orders of magnitude in the course of the laser treatment [4].

Much of the initial interest in laser annealing arose from the fact that pulsed lasers could be used for the activation of implanted dopants [5]. With this technique, activated dopant concentrations in silicon well above the solid solubility limit were achieved. During the laser annealing process, the re-growth from the melt occurs at high velocities that can reach 4 m/s [6]. It has been shown that the incorporation and activation of high dopant concentrations is due to the insufficient time dopant atoms have to diffuse, before they are trapped by the rapidly solidifying matrix [5, 6, 7].

At the early research stage, special emphasis was placed on the vertical epitaxial re-growth of thin layers on single crystal silicon (c-Si) [4]. Initially, amorphous silicon (a-Si) layers were formed on the surface of single crystal substrates either by ion implantation or by different deposition techniques such as chemical vapour deposition (CVD) and molecular beam epitaxy (MBE). In a second step, the a-Si layers were irradiated and transformed into c-Si layers, which under some laser parameters were nearly defect free [4].

At present, the most active area in the field of laser processing is the use of lasers for the crystallization of a-Si on insulating substrates such as plastic, sapphire, silicon nitride, quartz, and glass. This crystallization process forms polycrystalline silicon, which is considered an attractive material for thin film transistors (TFT's) in active matrix liquid crystal displays (AMLCD's) [8] and for thin film solar cells [9]. Most common is the use of

pulsed excimer lasers because of the strong absorption of the UV light in the near surface region that prevents possible damage to the substrate. Laser crystallization offers several advantages in comparison to other competitive techniques such as solid phase crystallization (SPC) [10, 11], metal induced crystallization (MIC) [12], and pulsed magnetron sputtering [13]: (i) laser crystallization is a rapid process that is appropriate for industrial use, (ii) the total amount of deposited energy needed to melt the layer is low, and (iii) the dopant concentration can be well controlled.

This work focuses on the investigation of laser-crystallized polycrystalline silicon-germanium (poly-SiGe) thin layers on foreign substrates (mostly quartz). The interest in poly-SiGe for solar cell applications has several reasons. For one, poly-SiGe exhibits an enhanced optical absorption in the infrared and the visible spectral range in comparison to poly-Si [14, 15]. This enhanced optical activity enables a poly-SiGe layer to be about 10 times thinner and still absorb the same amount of light as a poly-Si layer [14]. Moreover, the band-gap of SiGe alloys can be adjusted between 0.67 eV (Ge) [16] and 1.1 eV (Si) [17] in order to match specific demands. This makes poly-SiGe particularly suitable for the bottom cell of a multi-junction solar cell. In addition, poly-SiGe alloys have a lower melting temperature than poly-Si, thus requiring a lower thermal budget for their fabrication. It should be noted that the production techniques of SiGe alloys are completely compatible with the well-established silicon technology.

A great deal of work has been invested in elucidating the nucleation and crystal growth behavior of polycrystalline silicon thin films on foreign substrates under laser irradiation conditions [1, 18, 19, 20, 21, 22, 23, 24, 25, 26, 27, 28, 29]. It has been found that the crystallization process can be roughly divided into three regimes: partial melting, partial-complete transition, and complete melting of the film. As can be seen in Fig. 1.1, at the partial melting regime, which corresponds to low laser fluences, the nucleation and crystal growth occurs from the unmelted under-layer. Since the nucleation density at the solid-liquid interface is high, the grain size is relatively small ( $\approx 100$  nm). At the complete melting regime, which corresponds to high laser fluences, the layer is completely melted and the nucleation is believed to occur homogeneously in the liquid layer [28, 29]. The grain size in this case is similar to that in the partial melting regime. At the partial-complete melting transition, which occurs at a narrow energy fluence range of about  $100 \text{ mJ/cm}^2$ , nucleation is probably triggered from the interface between the substrate and the silicon layer. This occurs

either through unmelted islands or heterogeneous nucleation on the interface. In this regime, grains larger than ten times the thickness of the layer can be formed [2], and therefore it is also known as the super lateral growth regime [30].

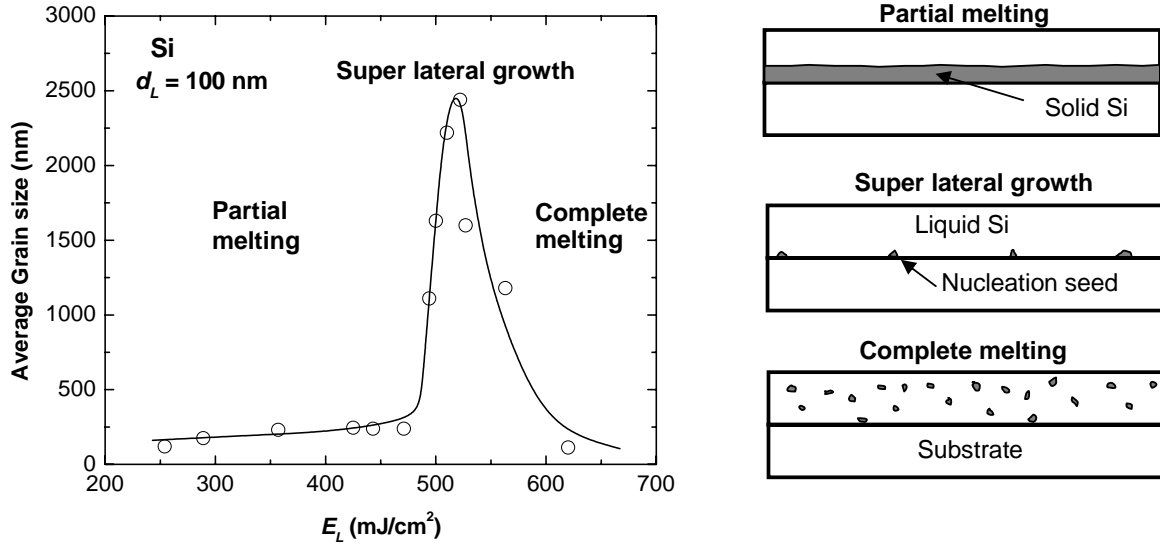


**Fig. 1.1:** Average grain size in laser-crystallized poly-Si thin film on glass as function of the laser fluence  $E_L$ . The thickness of the films was  $d_L = 100$  nm. Data was taken from Lengsfeld [2]. Nucleation in the three crystallization regimes follows the illustrations on the right.

The results that will be presented in this thesis show that laser crystallization of SiGe thin films can result in the appearance of self-organized hillocks or ripples on the surface of the sample that are not governed by nucleation and crystal growth according to the crystallization regimes described above. In fact, the periodicity length of the self-organized structure is on the scale of  $1 \mu\text{m}$  whereas the grain size is about  $100$  nm. Moreover, the structure appears in all three crystallization regimes despite the intuitive notion that homogeneous nucleation in the complete melting regime should kill the coherence of the phenomenon and thus suppress the self organization. A solidification model based on the Mullins-Sekerka instability theory [31] is suggested to account for the experimental findings. According to this model the self organization can be explained, independent of the crystallization regime, by the existence of an initially planar solid-liquid interface that becomes periodically modulated (unstable) during solidification.

Another central topic of this study is the characterization of defects in the laser-crystallized poly-SiGe thin films. It will be shown that the grain boundaries in poly-SiGe play

a more crucial role than in poly-Si, and in some cases can completely dominate the electrical transport and optical absorption of the material. Unlike for poly-Si, where electrical transport along grain boundaries is mostly attributed to impurities such as copper and iron [32, 33, 34], for the poly-SiGe specimens investigated here the effect is attributed merely to dangling-bond defects.

Since the performance of devices such as thin film solar cells and displays critically depends on the passivation of dangling-bond defects by hydrogen, this issue was investigated. The results of remote plasma post-hydrogenation experiments that will be presented here show that the passivation of dangling-bond defects is accompanied by the simultaneous generation of new electrically active defects. The possibility that these defects might be large two-dimensional hydrogen clusters known as platelets that were found in n-type crystalline and polycrystalline Si [35, 36] is also discussed.

## 2 Experimental Methods

This chapter reviews briefly the experimental methods used in the course of this study. Section 2.1 describes how the polycrystalline silicon-germanium (poly-SiGe) samples were prepared and Section 2.2 describes the methods used to characterize the samples. The description of the characterization methods concentrates on the experimental details rather than on the underlying physical principals of these methods.

### 2.1 Sample preparation

The poly-SiGe thin films on foreign substrates that were investigated in this work were produced by two main steps. Firstly, hydrogenated amorphous SiGe films (a-SiGe:H) were deposited on quartz, stainless steel, and molybdenum (Mo) coated quartz substrates. Secondly, these amorphous films were crystallized either by a step-by-step or a single step laser crystallization process or in a few cases, for the sake of comparison, by a solid phase crystallization process. These preparation procedures will be described in the following.

#### *Deposition of the amorphous starting material (a-SiGe:H)*

Hydrogenated amorphous silicon-germanium thin films with a Ge concentration between 0 and 100 at. % were deposited by glow discharge decomposition of a mixture of disilane ( $\text{Si}_2\text{H}_6$ ), germane ( $\text{GeH}_4$ ), and hydrogen ( $\text{H}_2$ ) on foreign substrates. This deposition method is known as plasma enhanced chemical vapor deposition (PECVD). The thickness  $d_L$  of the layers varied between 100 nm and 500 nm. The substrate temperature during deposition was 300 °C. The composition of the alloys was determined from the gas mixture and in some cases reconfirmed by elastic recoil detection analysis (ERDA) measurements. The ratio of the Ge concentration to the total Ge plus Si concentration is given by the atomic fraction  $x$  that will be simply referred to as Ge content throughout this thesis. All the a-Si<sub>1-x</sub>Ge<sub>x</sub>:H samples were produced in United Solar Ovonic Corp. USA and can be considered as solar-cell-grade material. The details of the a-Si<sub>1-x</sub>Ge<sub>x</sub>:H samples used in this thesis are summarized in Table 2.1.

**Tab. 2.1:** An overview of the a-Si<sub>1-x</sub>Ge<sub>x</sub>:H samples used in the course of this study as the starting material for the crystallization experiments.  $x$  is the Ge content,  $d_L$  is the sample thickness, and  $C_H$  is the hydrogen concentration in the samples given in atomic percent.

$x$	$d_L$ (nm)	$C_H$ (at. %)	Substrate
0	100	-	Quartz
0.19	130	12.8	Quartz
0.22	135	11.4	Quartz
0.3	110	-	Stainless steel
0.3	300	-	Stainless steel
0.3	100	-	30 nm Mo on quartz
0.3	100	-	160 nm Mo on quartz
0.3	100	-	500 nm Mo on quartz
0.33	160	10.8	Quartz
0.45	160	9.9	Quartz
0.5	100	-	Quartz
0.5	240	-	Stainless steel
0.5	100	-	30 nm Mo on quartz
0.5	100	-	160 nm Mo on quartz
0.5	100	-	500 nm Mo on quartz
0.7	165	5.4	Quartz
0.84	250	3.6	Quartz
1	100	-	Quartz
1	500	-	Quartz

### *Step-by-step laser crystallization*

Laser crystallization of the a-SiGe:H samples was done with a pulsed XeCl excimer laser (Lambda Physik, Compex 205i). The principal setup of the laser crystallization apparatus is shown in Fig. 2.1. The laser operates at a wavelength of 308 nm, a pulse time length of approximately 30 ns, and a maximum laser fluence of  $\approx 900$  mJ/cm<sup>2</sup>. The maximum laser pulse repetition rate used in the crystallization experiments was 20 Hz. The laser fluence,  $E_L$ , was tuned with an optical attenuator. An optical homogenizer, consisting of two "fly's-eye" lens arrays, was used to create a uniformly illuminated  $6 \times 6$  mm<sup>2</sup> laser spot. The samples were crystallized in a vacuum chamber, which was mounted on an x-y translation stage. Crystallization of large areas was achieved by moving the sample under the laser beam. However, most crystallization experiments in this work were performed on a fixed  $6 \times 6$  mm<sup>2</sup>

spot. The pressure in the vacuum chamber was typically about  $10^{-4}$  mbar and the experiments were mostly performed at room temperature.

As shown in Table 2.1, the a-SiGe:H samples contained high amounts of hydrogen. The crystallization of such samples with laser irradiation, if not handled cautiously, might result in severe damage to the samples due to explosive out-diffusion of hydrogen. One possible approach to overcome this problem is to utilize a step-by-step crystallization [22, 24]. In this crystallization procedure the laser fluence is successively increased so that out-diffusion of hydrogen is controlled and does not cause damage to the samples. The process used in this study started with an initial laser fluence close to the surface melting threshold of  $E_L = 100 \text{ mJ/cm}^2$ . In each subsequent step the laser fluence was increased by a small amount  $\Delta E_L = 20 \text{ mJ/cm}^2$  until the desired final laser fluence was reached. Each step consisted of 100 laser pulses per unit area. One of the interesting properties of the step-by-step crystallization method is that high amounts of hydrogen still remain in the sample ( $\approx 1 \text{ at. \%}$ ) after the crystallization and can be activated upon annealing [37].

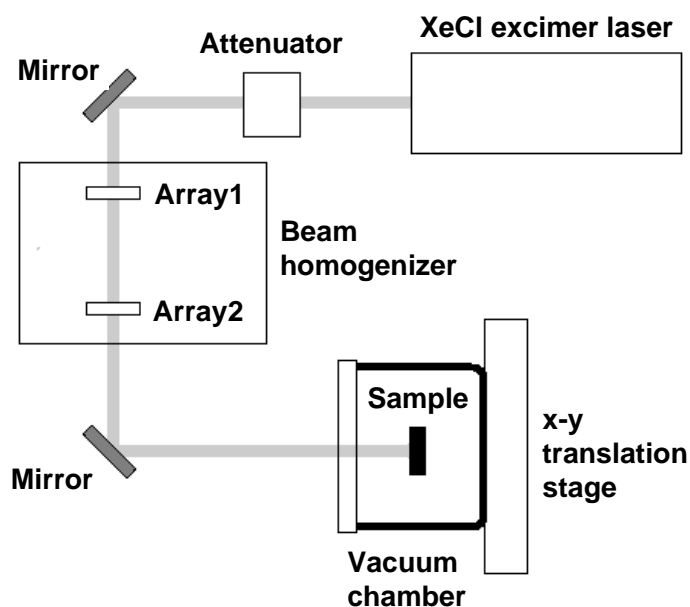


**Fig. 2.1:** A schematic illustration of the setup used for the laser crystallization.

### *Single step laser crystallization*

A different approach to overcome the problem of damage during crystallization is to remove the hydrogen prior to the crystallization. This was achieved by annealing the SiGe specimens in a standard furnace at 450 °C for several hours. Raman backscattering measurements were performed after the anneal to confirm that the sample remained amorphous. The dehydrogenated samples were then exposed to laser pulses with the desired laser fluences in a single step. Mostly the crystallization with this procedure was done just with a single laser pulse but also varying numbers of pulses between 1-100 were utilized to investigate structural changes with increasing number of laser pulses.

### *Solid phase crystallization*

For comparison purposes, some of the amorphous SiGe samples were thermally crystallized by a several-hour furnace anneal at a temperature increasing from 470 °C (for pure Ge) up to 550 °C (for Si<sub>0.5</sub>Ge<sub>0.5</sub>). It was not possible with this method to crystallize a-Si<sub>1-x</sub>Ge<sub>x</sub> films with  $x < 0.5$  without causing severe damage ranging from large holes till the complete disappearance of the films. This damage occurs probably due to the huge difference in the thermal expansion of the quartz substrate and the SiGe layer. The linear thermal expansion coefficient for SiGe is in the range  $2.6 \times 10^{-6} - 5.8 \times 10^{-6} \text{ K}^{-1}$  compared to  $0.5 \times 10^{-6} \text{ K}^{-1}$  for quartz [38]. Raman backscattering measurements were performed after the anneal to confirm that the samples were crystallized.

## **2.2 Characterization methods**

### *Scanning electron microscopy*

Information concerning the grain size and surface morphology of the laser-crystallized poly SiGe samples was obtained from scanning electron microscopy (SEM) micrographs. Some SEM micrographs were taken over large areas to investigate the formation of patterns and self organization. The measurements were performed using a REM S-4100 (Hitachi) with

a cold field emission cathode. To obtain a good contrast between grains and grain boundaries, defect etching was applied. Some of the poly-SiGe samples were etched with a Secco etch solution [39] that consists of one volume part 0.15 molar  $K_2Cr_2O_7$  and two volume parts 10 % HF. The etching time with this solution was 8 sec. Other poly-SiGe samples with a high Ge content were etched with a CP6 solution [40] that consists of two volume parts 65 %  $HNO_3$ , one volume part 96 %  $CH_3COOH$ , and one volume part of 50 % HF, diluted by adding two volume parts  $H_2O$ . The etch time for this solution was between 8-30 sec.

### *Energy dispersive X-ray*

The SEM device was also equipped with a Si (Li) detector (Noran) for energy dispersive X-ray (EDX) microanalysis. Alloy compositions were measured with EDX by detecting the characteristic spectral lines for Si ( $K\alpha_1$ ) and for Ge ( $L\alpha_1$ ). The primary electron energy was set to 4 keV since this low energy ensured that no significant contribution to the measured signal was created from the quartz substrate. Single crystal SiGe was used to calibrate the intensities of the characteristic spectral lines. A good agreement between the EDX and the elastic recoil detection analysis (ERDA) measurements was found for the average composition values.

### *Atomic force microscopy*

Surface roughnesses as well as other properties of the surface of the laser-crystallized SiGe samples were obtained by atomic force microscopy (AFM). The AFM measurements were performed with a Topometrix Explorer 2000 in the contact mode. Root mean square (RMS) surface roughness values were obtained from  $2 \times 2 \mu m^2$  and  $5 \times 5 \mu m^2$  micrographs.

### *Raman backscattering spectroscopy*

Raman spectroscopy is a standard method for the characterization of phonon properties in poly-Si thin films. Raman measurements were performed in the backscattering configuration using a DILOR/ISA LabRAM 010 equipped with an HeNe laser that operates at a wavelength of  $\lambda = 632.8$  nm. The intensity of the HeNe laser was reduced to about 0.2 mW

by applying a grey filter. An objective with a magnification of 100 was used to focus the laser to a spot with a diameter of about 1  $\mu\text{m}$ . The setup contained a single monochromator with a diffraction grating of 1800 grooves/mm that yielded a spectral resolution of about 1  $\text{cm}^{-1}$ .

### *Electron spin resonance*

One of the most widely used methods to characterize paramagnetic defects in the band-gap of semiconductors is electron spin resonance (ESR). The ESR measurements were performed on a commercial Bruker Elexsys 580 X-band spectrometer using a rectangular  $\text{TE}_{102}$  cavity at temperatures ranging from 4 to 300 K. An illustration of the experimental setup is shown in Fig. 2.2. The sample is exposed to a static magnetic field  $B_0$  and to microwave irradiation generated by a gunn-diode (9-10 GHz) in the microwave bridge. The magnetic field  $B_0$  is swept in some range between 0 and 0.6 Tesla and absorption changes of the microwave are being monitored. When the magnetic field reaches a value that together with the microwave frequency matches an electron spin resonance, microwave radiation is absorbed. The absorption signal is detected using a lock-In technique and therefore the resonance has the typical first derivative shape shown in Fig. 2.2. The Lock-In technique involves modulating  $B_0$  with a small magnetic field, which in this study had an amplitude of 0.4 mT and a frequency of 100 KHz.

The magnetic field  $B_0$  interacts with the spin of the electrons and lifts the twofold degeneracy of the electron states according to the Zeeman effect. Electron spin resonance between these states follows

$$\Delta E = h\nu = g\mu_B B_0 \quad , \quad (2.1)$$

where  $\Delta E$  is the Zeeman splitting,  $h\nu$  is the microwave energy,  $\mu_B$  is Bohr magnetron constant and  $g$  is the Lande factor which is 2.0023 for a free electron. In solids the  $g$  factor can vary according to the local surrounding of the electron thus, providing information about the possible existence of different kind of paramagnetic defects. The absorption signal intensity can be used to deduct the concentration of these defects.

The same experimental setup was also used to measure electric dipole spin resonance (EDSR). In contrast to ESR where the signal is caused by the absorption of the magnetic field of the microwave, EDSR is caused by the absorption of the electric field of the wave. The details concerning the appearance of the EDSR signal will be presented in Sec. 3.2.1.

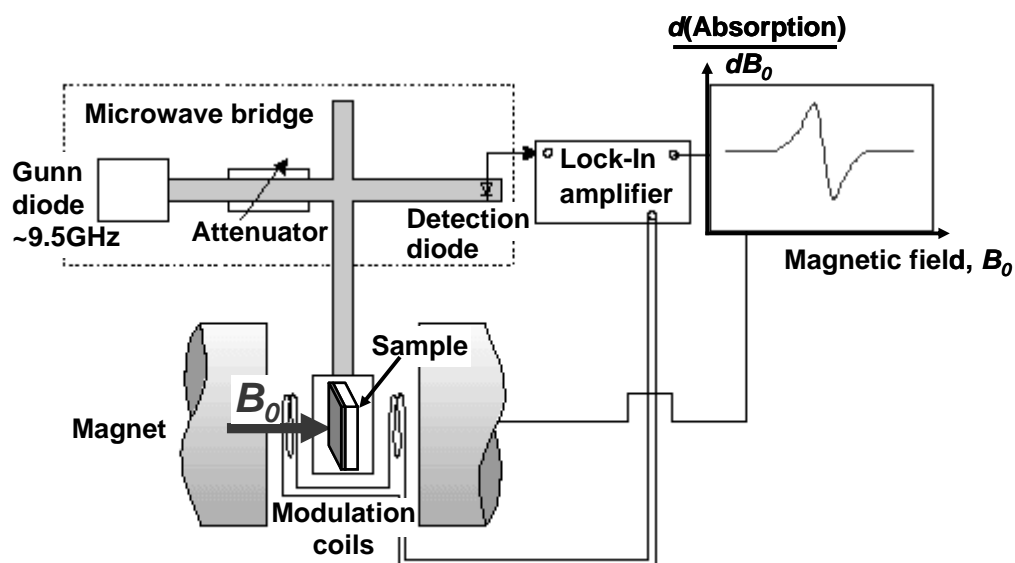


Fig. 2.2 Schematic illustration of the electron spin resonance (ESR) setup

### *Conductivity and photoconductivity measurements*

The conductivity and photoconductivity of the laser-crystallized poly-SiGe samples were measured in the Van der Pauw configuration [41] at temperatures ranging from 20 to 300 K. After testing different metals, titanium was used for the contacts because it revealed ohmic behavior in the entire temperature range. The photoconductivity was measured under white light illumination that had a characteristic spectrum of a black body at 3000 K.

### *Photothermal deflection spectroscopy*

To study optical absorption properties of laser-crystallized poly-SiGe, photothermal deflection spectroscopy (PDS) measurements were performed. The experimental setup is

illustrated in Fig. 2.3. The sample is positioned in a cavity filled with some liquid that in our case was Tetradecafluorohexane ( $C_6F_{14}$ ). The absorption of monochromatic light in the sample induces a temperature gradient in the liquid at the near-surface region of the sample. This temperature gradient corresponds to a refraction index gradient. Therefore, when a probe laser beam travels near the surface through this region, it deflects. The deflection signal, measured as the displacement of the laser spot on a position sensing detector, is proportional in first approximation to the absorption coefficient  $\alpha$ .

It should be noted that the PDS method is especially useful in measuring the sub-band-gap absorption where conventional transmission and reflection measurements of absorption coefficients are unreliable. It has been shown that the sub-band-gap absorption coefficient of a-Si:H measured with PDS directly correlates to the dangling-bond concentration in this material [42].

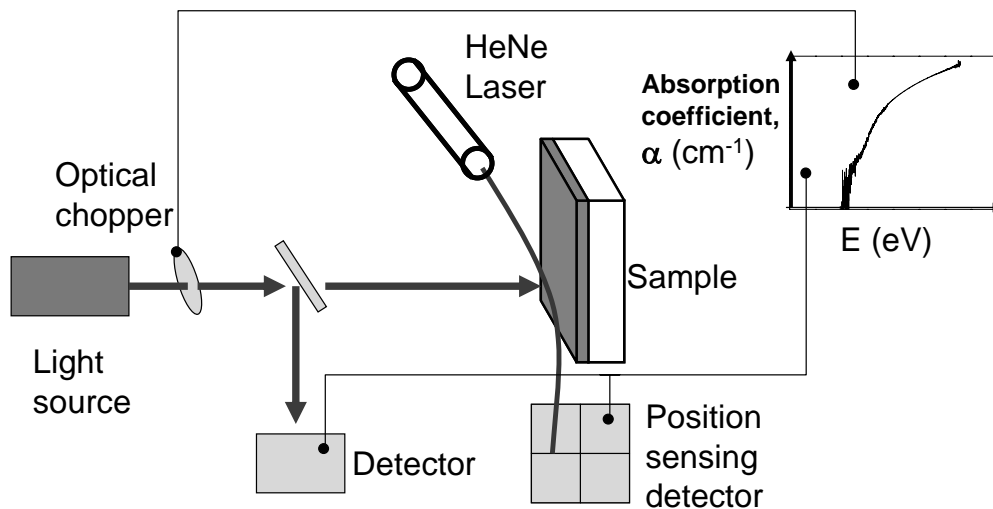


**Fig. 2.3** Schematic illustration of the photothermal deflection spectroscopy (PDS) setup

## 3 Experimental results

In this chapter, the structural, electrical, and optical properties of laser-crystallized silicon-germanium ( $\text{Si}_{1-x}\text{Ge}_x$ ) thin films with  $0 < x < 1$  are reported. Sec 3.1 concentrates on the surprising appearance of a self-organized structure on the surface of the samples upon laser irradiation. Special emphasis is placed on the conditions under which this phenomenon appears. It is also shown that field emission devices are a promising application for the self-organized structure. In Sec. 3.2, the focus changes to defect properties in the poly-SiGe films. Electron spin resonance (ESR) measurements show that increasing the Ge content in the sample causes, at a critical concentration of about 70 at. %, a transition from an ESR signal to an electric dipole spin resonance (EDSR) signal. Samples that exhibit EDSR signals exhibit an unusually high conductivity at low temperatures that is nearly temperature independent (metallic-like). Incorporating hydrogen into these samples by plasma post-treatments changes this behavior and causes the conductivity to decrease and ultimately to become activated. It is shown that these results are intimately related to defects at the grain boundaries of the material. The influence of defects and disorder at the grain boundaries can also be seen in the optical absorption results presented in this section.

### 3.1 Laser-induced self organization in SiGe thin films

#### 3.1.1 Pattern formation

Laser irradiation of smooth amorphous  $\text{Si}_{1-x}\text{Ge}_x$  thin films on glass substrates with a germanium content of  $0.3 < x < 0.7$  resulted in the formation of periodic surface structures. A typical SEM micrograph of a poly- $\text{Si}_{1-x}\text{Ge}_x$  sample with an average Ge content of  $x = 0.45$  that was crystallized using a step-by-step process with a final laser fluence of  $E_L = 600 \text{ mJ/cm}^2$  can be seen in Fig. 3.1(a). The white spots in the image are hillocks that are significantly elevated above the sample surface. Fig 3.1(b) shows a SEM micrograph of the typical grain structure between hillocks. The average grain size is about 100 nm and does not change significantly when varying the number of laser pulses or the laser fluence. Fig 3.1(c) shows the result of a two dimensional fast Fourier transformation of Fig. 3.1(a). The appearance of a circle in the reciprocal space indicates that hillocks are formed at a strikingly well defined distance from each other. The distance between hillocks, which defines the

periodicity length of the structure, can be simply calculated as  $d = 1/r = 1.2 \mu\text{m}$ , where  $r$  is the radius of the circle shown in Fig. 3.1(c). The cross section SEM micrograph of a single hillock is shown in Fig. 3.1(d). The hillock reaches a height of more than 100 nm above the surface, which was found to be in agreement with atomic force microscopy (AFM) measurements. It is interesting to note that the grain size is about one order of magnitude smaller than the periodicity length of the self-organized structure, which demonstrates that there is no correlation between the grain structure and the self organization.

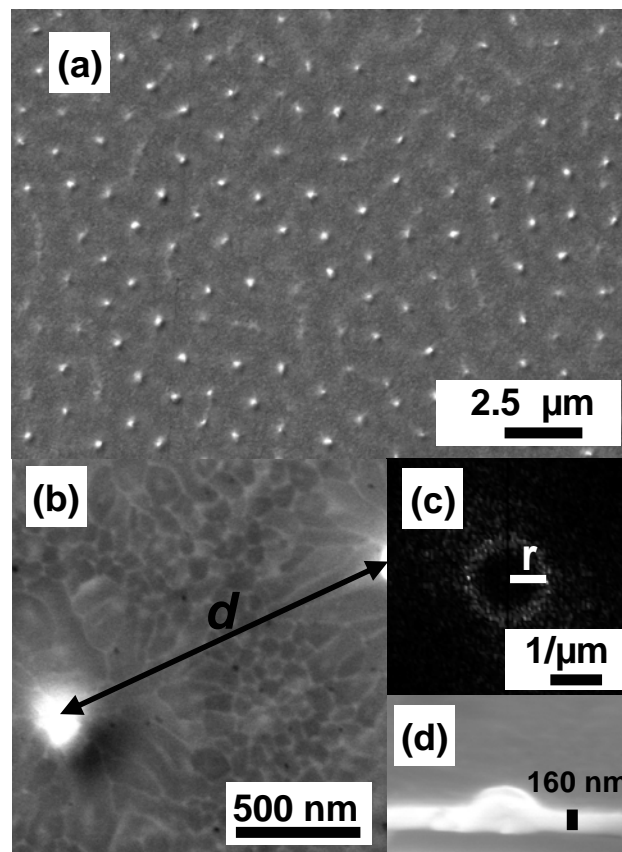


**Fig. 3.1** Surface morphology of a laser-crystallized poly-Si<sub>0.55</sub>Ge<sub>0.45</sub> thin film on glass. The film had a thickness of 160 nm and was crystallized employing a step-by-step crystallization process with a final laser fluence of  $E_L = 600 \text{ mJ/cm}^2$ . (a) shows a SEM image of the surface. The laser crystallized film exhibits a self-organized structure of hillocks on the surface. (b) shows a SEM image of the grain structure between hillocks. (c) depicts the power spectrum of a two-dimensional Fourier analysis of the sample surface and (d) shows the cross section of a single hillock.

Compositional variations in the laser-crystallized poly-SiGe samples were studied with energy dispersive X-ray (EDX) measurements. Fig. 3.2 shows the result of an EDX line scan carried out on a poly-Si<sub>1-x</sub>Ge<sub>x</sub> sample with an initial Ge content of  $x = 0.36$  that was crystallized with a step-by-step process and a final laser fluence of  $E_L = 550 \text{ mJ/cm}^2$ . The line

superimposed on the surface micrograph in Fig. 3.2(a) shows where the EDX line scan was performed. The Ge content of the poly-SiGe sample is plotted in Fig. 3.2(b) and exhibits a sinusoidal variation between  $x = 0.49$  at the hillocks and  $x = 0.28$  between hillocks. It should be noted that the sinusoidal variation is due to the finite resolution of the EDX system. According to Raman measurements previously performed on the same samples, the actual variation of the Ge content is expected to be more abrupt [43]. The data clearly establish that the self-organized hillock structure is in accordance with the lateral variation of the Ge content. For SiGe films with a Ge content outside the range  $0.3 < x < 0.7$  neither structure formation nor lateral segregation was observed.

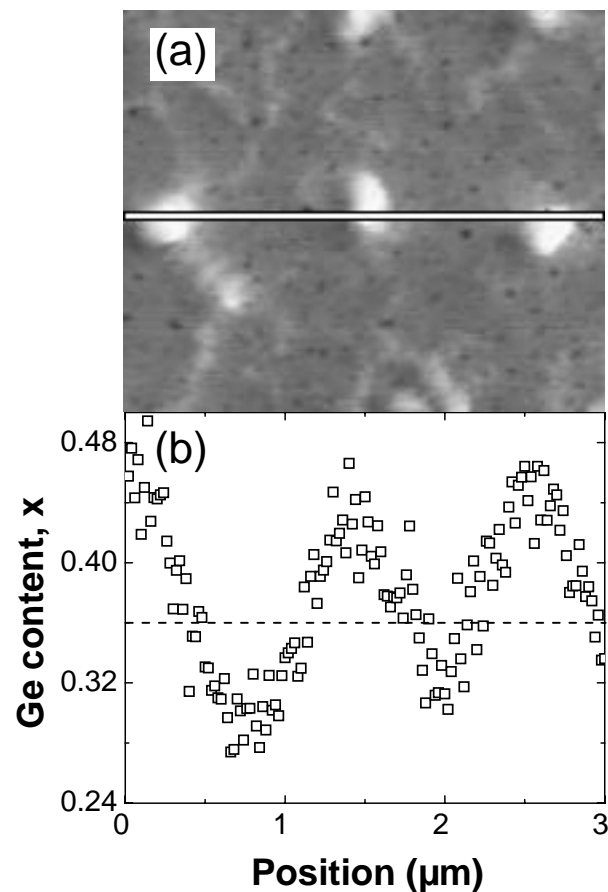


**Fig. 3.2** Energy dispersive X-ray (EDX) line scan. (a) Scanning electron microscopy (SEM) micrograph of a laser crystallized poly-Si<sub>0.64</sub>Ge<sub>0.36</sub> thin film on glass. The film had a thickness of 160 nm and was crystallized employing a step-by-step crystallization with a final laser fluence of  $E_L = 550 \text{ mJ/cm}^2$ . (b) shows the germanium content  $x$  along the line indicated in (a). The dashed line at  $x = 0.36$  represents the average Ge content in the laser-crystallized specimen that is identical with the Ge content in the amorphous starting material.

In order to determine how the self organization evolves with an increasing number of laser pulses, the single-step crystallization procedure with a varying number of laser pulses was used. Fig 3.3 shows SEM micrographs from poly-Si<sub>0.55</sub>Ge<sub>0.45</sub> films on glass substrates crystallized with a laser fluence of  $E_L = 570 \text{ mJ/cm}^2$  applying either 1, 3, or 60 laser pulses. Surprisingly, the sample crystallized with a single laser pulse exhibits a ripple structure rather than a hillock structure. The bright areas, as in Fig. 3.2, are elevated and contain a higher Ge content (about 47 at.%). As the number of laser pulses increases to 3, the ripples disappear altogether and hillocks start to show up. Applying 60 laser pulses causes the appearance of a well-pronounced hillock structure similar to the one produced with the step-by-step crystallization (see Fig. 3.1(a)). This evolution from ripples to hillocks was also found when the laser fluence was set to different values in the range of 320-620  $\text{mJ/cm}^2$ . With decreasing laser fluence, the transition from ripples to hillocks occurred at a higher number of laser pulses. In some cases, it was possible to observe at this transition a pattern containing a mixture of ripples and hillocks.

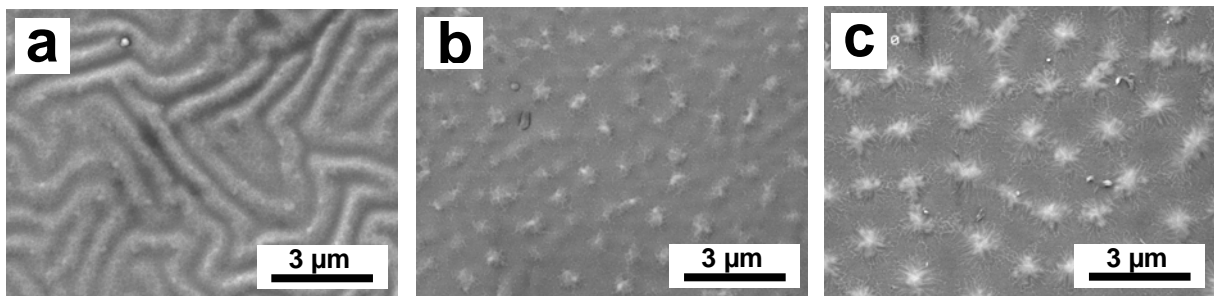


**Fig. 3.3** Scanning electron microscopy (SEM) micrographs of poly-Si<sub>0.55</sub>Ge<sub>0.45</sub> on a glass substrate crystallized with a laser fluence of  $E_L = 570 \text{ mJ/cm}^2$  applying (a) 1 laser pulse, (b) 3 laser pulses, and (c) 60 laser pulses.

The appearance of ripples, rather than hillocks, after a single laser pulse is related to the fact that the first laser pulse was introduced to an amorphous layer whereas subsequent laser pulses were introduced to a polycrystalline layer. To verify that the initial phase of the layer was the cause of the different patterns observed, an amorphous Si<sub>0.5</sub>Ge<sub>0.5</sub> sample was crystallized by annealing for 3 hours at 550°C and then exposed to a single laser pulse. Fig. 3.4(a) shows that this sample exhibited a hillock structure whereas a Si<sub>0.5</sub>Ge<sub>0.5</sub> sample that was irradiated under the same conditions but was initially amorphous (Fig. 3.4(b)), exhibited

a ripple structure. These experiments clearly demonstrate that upon irradiation, ripples appear for an initially amorphous layer whereas hillocks appear for an initially polycrystalline layer.

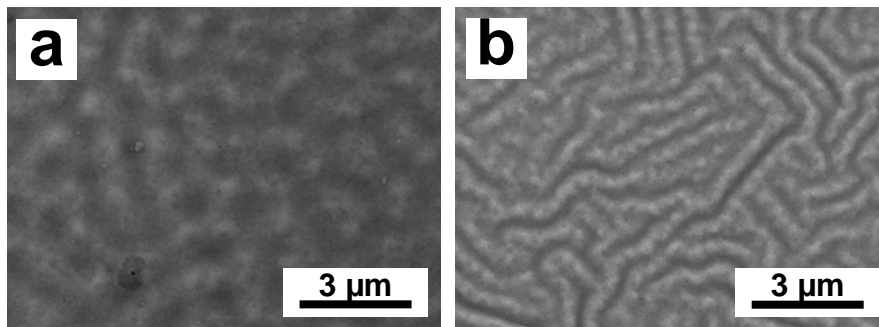


**Fig. 3.4** Scanning electron microscopy (SEM) micrographs of poly-Si<sub>0.5</sub>Ge<sub>0.5</sub> on a glass substrate crystallized with a single laser pulse and a laser fluence of  $E_L = 360 \text{ mJ/cm}^2$ . Sample (a) was annealed for 3 hours at 550°C and was polycrystalline prior to the laser irradiation. Sample (b) was annealed for 6 hours at 450°C to remove hydrogen and remained amorphous before exposure to the laser pulse. Raman backscattering spectroscopy was utilized after the annealing step and prior to laser irradiation to determine whether the sample was amorphous or polycrystalline.

Substituting the glass substrate with molybdenum (Mo) coated glass or with stainless steel substrates had a great impact on the structure formation. Fig. 3.5 shows SEM micrographs of three poly-Si<sub>0.5</sub>Ge<sub>0.5</sub> films on molybdenum coated glass. The molybdenum thickness was 30, 160, and 500 nm for the samples shown in Fig. 3.5(a), (b), and (c), respectively. The samples were crystallized with a step-by-step process and with a final laser fluence of  $E_L = 420 \text{ mJ/cm}^2$ . Self organization clearly occurred in the sample containing a 30 nm thick Mo layer (Fig. 3.5 (a)). However, as the thickness of the molybdenum layer increased, the self organization was partially suppressed and finally disappeared for the

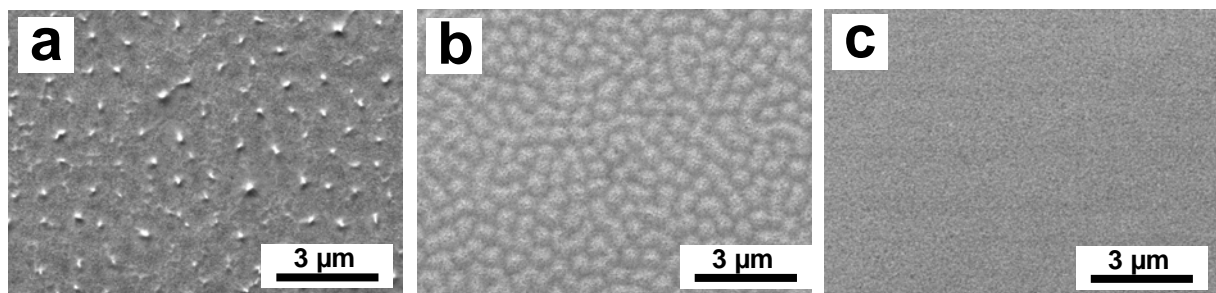


**Fig. 3.5** Scanning electron microscopy micrographs of laser-crystallized poly-Si<sub>0.5</sub>Ge<sub>0.5</sub> on molybdenum coated glass. The samples were crystallized with a step-by-step crystallization process using a final laser fluence of  $420 \text{ mJ/cm}^2$ . The thickness of the molybdenum layer was (a) 30, (b) 160, and (c) 500 nm.

samples with 500 nm of molybdenum. Similar structure suppression behavior was obtained for SiGe films on molybdenum coated glass that were crystallized with a final laser fluence varying from 220 to 500  $\text{mJ}/\text{cm}^2$ . In addition, poly-SiGe films on stainless steel substrates that were crystallized with a step-by-step process did not exhibit any self-organized structure. These observations are discussed in detail in Sec. 4.1 and are believed to be closely related to the modified thermal conductivity of the substrate, which affects the solidification velocity.

Further details concerning the emergence of the self organized structure after a single laser pulse are given in Fig. 3.6, which shows the periodicity length  $d$  as a function of the laser fluence  $E_L$ . The periodicity length  $d$  exhibits a maximum at a laser fluence  $E_L$  that corresponds to the transition between partial and complete melting of the layer. This result shows that  $d$  is sensitive to the crystallization regime (partial or complete melting) and does not correlate with the melt duration, which continuously increases with increasing  $E_L$ . In addition, Fig. 3.6 shows that the periodicity length  $d$  increases with increasing Ge content  $x$  and with layer thickness  $d_L$ .

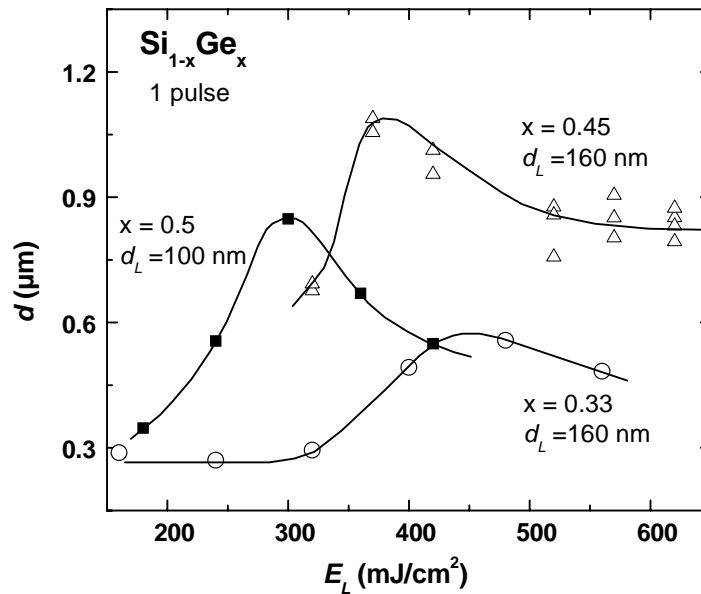


**Fig. 3.6** Periodicity length  $d$  of the self-organized structures that appear on the laser-crystallized poly-Si<sub>1-x</sub>Ge<sub>x</sub> surface after a single laser pulse as function of the laser fluence  $E_L$ . The corresponding Ge content  $x$  and the sample thickness  $d_L$  are indicated in the plot.

The structural evolution of the hillocks with increasing number of laser pulses was examined in detail with the two-dimensional Fourier analysis. Representative results for poly-Si<sub>0.55</sub>Ge<sub>0.45</sub> crystallized with  $E_L = 570 \text{ mJ}/\text{cm}^2$  are shown in Fig. 3.7. After a single laser pulse,

the periodicity length reaches a value of  $d \approx 0.9 \mu\text{m}$ . This value increases rapidly with the first several laser pulses and approaches a constant value of  $d \approx 1.6 \mu\text{m}$  after about 60 laser pulses. This observation clearly demonstrates that the self-organized structure develops successively as the number of laser pulses increases.

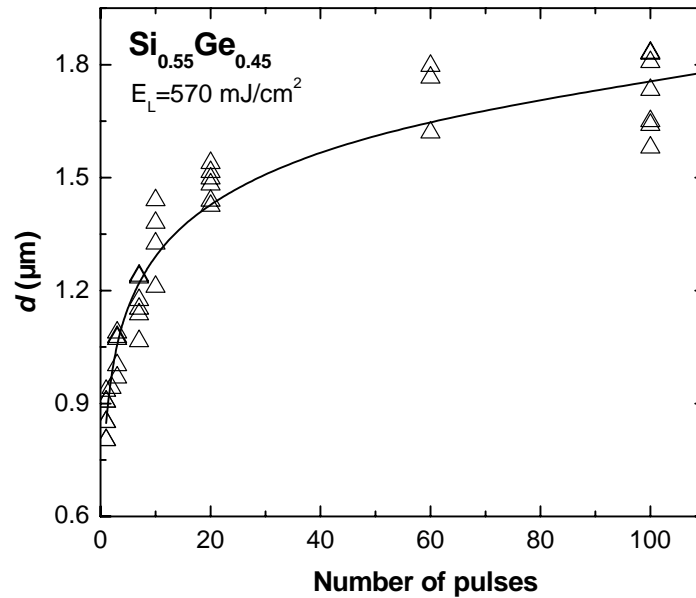


**Fig. 3.7** Periodicity length  $d$  of the self-organized structures that appear on the laser-crystallized poly-Si<sub>0.55</sub>Ge<sub>0.45</sub> surface as function of the number of laser pulses. The laser fluence employed was  $E_L = 570 \text{ mJ/cm}^2$ .

The periodicity length attained for Si<sub>0.55</sub>Ge<sub>0.45</sub> after a multiple number of laser pulses, applying a step-by-step crystallization process or a single step process with 100 laser pulses can be seen in Fig. 3.8. The periodicity length  $d$  obtained by the step-by-step process is in the range of 0.4-1.6  $\mu\text{m}$ , whereas for the single step process  $d$  is in the range of 1.2-2  $\mu\text{m}$ . The difference between these crystallization processes reveals that  $d$  does not depend only on the final step in the step-by-step process but on the entire irradiation history. After a structure is formed at the beginning of the step-by-step process ( $E_L \approx 100 \text{ mJ/cm}^2$  and  $d \approx 0.4 \mu\text{m}$ ), the periodicity length  $d$  exhibits small changes with each additional step, especially in the range  $E_L < 500 \text{ mJ/cm}^2$ , and does not reach the values obtained by the single step crystallization. It is interesting to note that the peak observed in Fig. 3.6 for a single pulse at  $E_L \approx 360 \text{ mJ/cm}^2$  is completely absent after 100 laser pulses in Fig. 3.8. These observations indicate that the structure evolution with multiple irradiations is complex, most probably non-linear, and difficult to characterize. Therefore, most of the theoretical work that will be presented in the discussion focuses on the emergence of a structure after a single laser pulse.

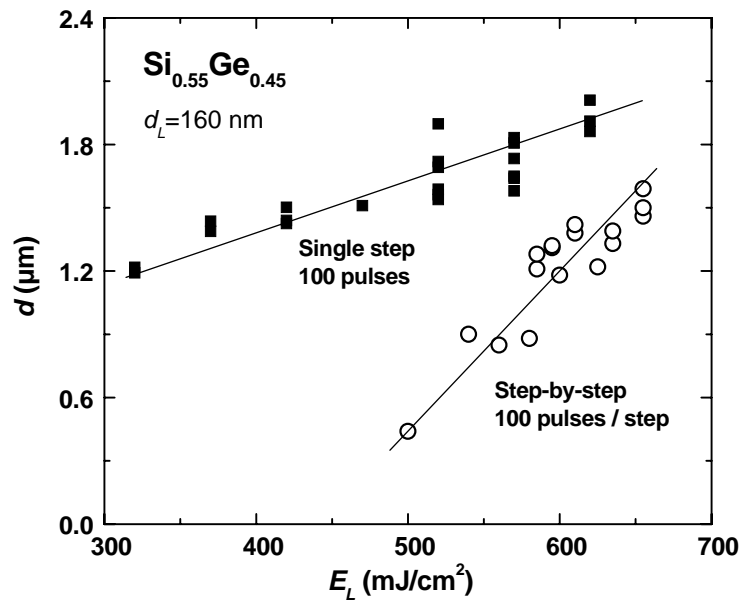


**Fig. 3.8** Periodicity length  $d$  of the self-organized structures that appear on the laser-crystallized poly-Si<sub>0.55</sub>Ge<sub>0.45</sub> surface as function of the final laser fluence  $E_L$  for step-by-step and single step processes.

### 3.1.2 Melting and solidification

The transient conductance measurement (TCM) technique was utilized to probe the melting and solidification of the SiGe layers under laser irradiation conditions. Fig. 3.9 shows the melt-depth signal for Si<sub>0.5</sub>Ge<sub>0.5</sub> on glass for laser fluences of 160, 280, and 400 mJ/cm<sup>2</sup> corresponding to the partial melting, partial-complete transition, and the complete melting regime, respectively. Melting of the surface of the Si<sub>0.5</sub>Ge<sub>0.5</sub> films begins at about  $E_L = 100$  mJ/cm<sup>2</sup>. The maximum melt depth increases with increasing  $E_L$  until it reaches the full depth of the layer (100 nm) for  $E_L = 280$  mJ/cm<sup>2</sup> at the transition between partial and complete melting. At higher laser fluences (complete melting regime) a significant increase in the melt duration and some oscillations in the average melt depth are observed due to the release of latent heat [29].

The average melt depth transients also provide information about the solidification velocity  $v$  in the crystallization process.  $v$  was calculated as the steepest slope of the average melt depth transient where a monotonic decrease was observed (arrows in Fig. 3.9). Some of the values measured for  $v$  are shown in Fig. 3.10. The data were obtained from crystallization

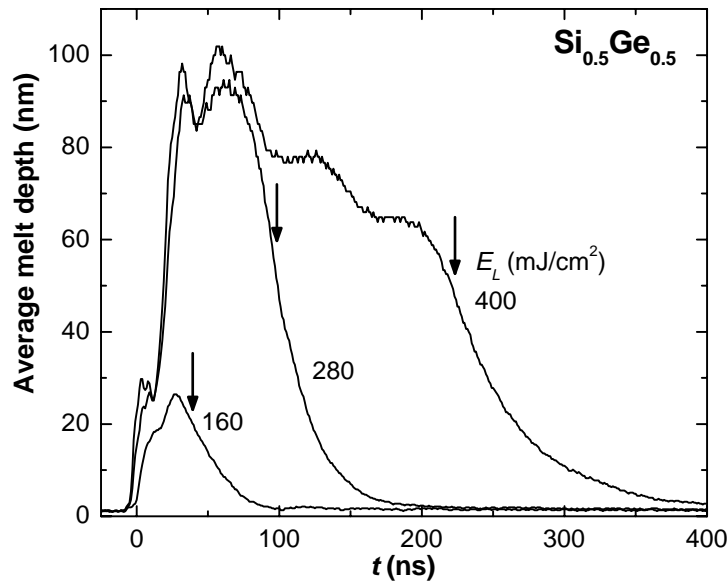


**Fig. 3.9** Average melt depth history derived from transient conductance measurements (TCM) for  $\text{Si}_{0.5}\text{Ge}_{0.5}$  on glass substrates. The transients shown correspond to the three different growth regimes: partial melting ( $E_L = 160 \text{ mJ/cm}^2$ ), partial-complete transition ( $E_L = 280 \text{ mJ/cm}^2$ ), and complete melting ( $E_L = 400 \text{ mJ/cm}^2$ ). The arrows indicate where the solidification is the fastest without taking into account the oscillatory range of the complete melting transient.

experiments of  $\text{Si}_{1-x}\text{Ge}_x$  with  $x = 0.33$  and  $x = 0.5$ . The laser fluence was varied within the range of 120 to 480  $\text{mJ/cm}^2$ . The circles represent solidification velocities that were taken from melt transients of an initially amorphous SiGe layer whereas the squares represent those taken from melt transients of an initially poly-SiGe layer. The peaks in the solidification velocity at  $E_L = 280 \text{ mJ/cm}^2$  for  $x = 0.5$  and  $E_L = 480 \text{ mJ/cm}^2$  for  $x = 0.33$  correspond to the transition between partial and complete melting of the layer. Solidification experiments performed on Si reveal that the solidification velocity is limited by diffusion of atoms in the liquid according to [44]

$$v(T) = \frac{f \cdot d_s \cdot D(T)}{\lambda^2} \cdot \left( 1 - \exp\left(\frac{\Delta G}{k \cdot T}\right) \right) \quad , \quad (3.1)$$

where  $\Delta G$  is the difference in Gibbs free energy per atom between the liquid and the solid,  $T$  is the solid-liquid interface temperature,  $k$  is the Boltzmann constant,  $D(T)$  is the diffusion coefficient of the liquid,  $\lambda$  is the mean free path in the liquid,  $d_s$  is the average distance over which the interface moves for a successful jump, and  $f$  is the fraction of active sites at the

interface. Under moderate super-cooling conditions,  $v$  increases as the degree of super-cooling increases due to the enhancement in the Gibbs free-energy difference. At higher super-cooling levels,  $v$  reaches a maximum and then decreases due to the reduction in the liquid diffusivity  $D(T)$  of the super-cooled melt. Since the solidification velocities derived from the melt transients are lower than the theoretical maximum expected for SiGe alloys ( $\approx 10$  m/s) [45], we can assume that moderate super-cooling conditions exist in our experiments. This would suggest that the increase in  $v$  in the partial melting regime is caused by the increase in the degree of super cooling with increasing  $E_L$ . In contrast, at the complete melting regime, as

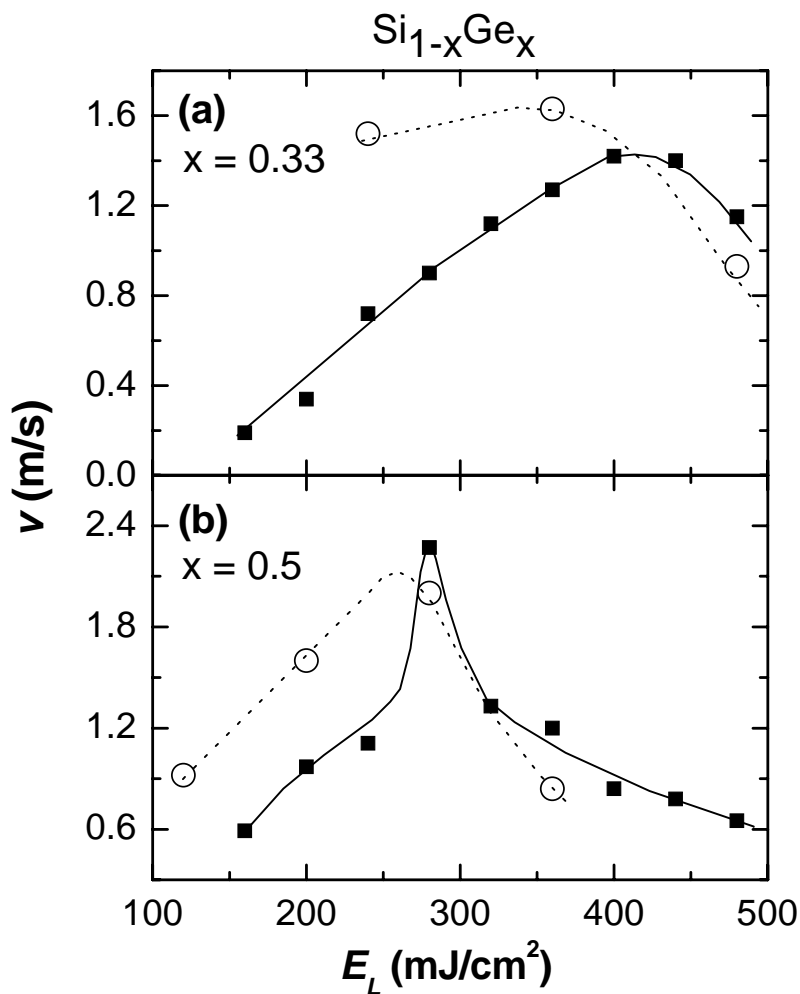


**Fig. 3.10** Solidification velocity  $v$  for Si<sub>1-x</sub>Ge<sub>x</sub> with  $x = 0.3$  (a) and  $x = 0.5$  (b) as a function of the laser fluence  $E_L$ . The velocity was taken as the steepest slope in the average melt depth transient where a non-oscillating decrease in the average melt depth is observed (see arrows in Fig.(6)). The maximum in  $v$  corresponds to the partial-complete melting transition. The open circles represent samples that were crystallized with a single laser pulse and were initially amorphous whereas the full squares were obtained on samples that were crystallized with several laser pulses and hence, were initially polycrystalline.

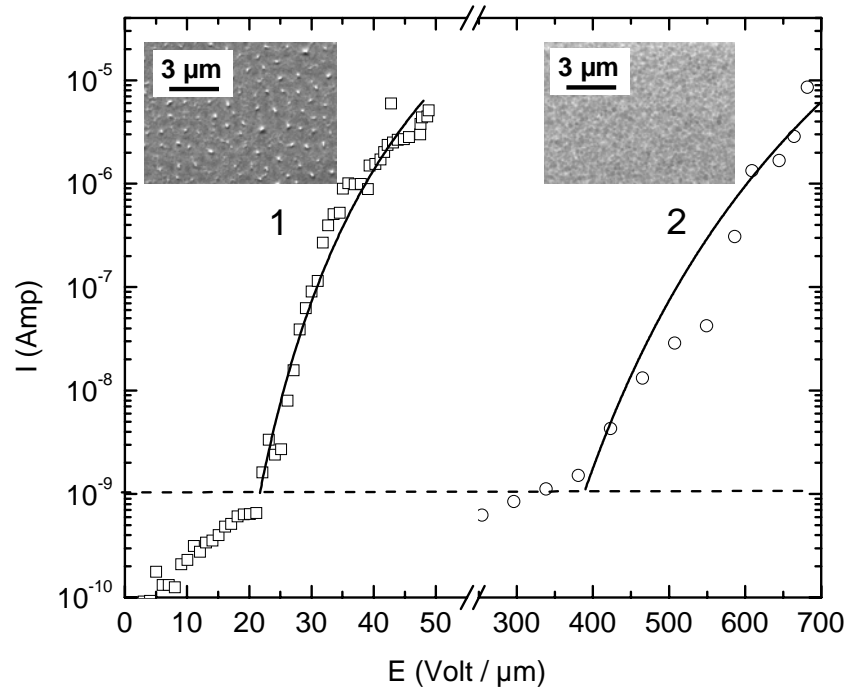
Moon et al. [46] have shown, the nucleation temperature does not change significantly as  $E_L$  varies. The decrease in  $v$  in this regime is probably due to a broadening of the thermal gradient into the glass.

Fig. 3.10 shows that  $v$ , extracted from melt transients of initially amorphous layers, is shifted to lower laser fluences. This shift is most probably due to the reduction in energy needed to melt an amorphous layer compared to a polycrystalline layer. Moreover, the initially amorphous samples exhibit more oscillations in the average melt depth transient. This might be due to explosive crystallization, a self containing process that occurs when the latent heat released upon solidification causes the melting of additional amorphous areas. The results shown in Fig. 3.10 indicate that it is not the solidification velocity which is responsible for the different self-organized structures observed (see Fig. 3.4). The appearance of ripples instead of hillocks when an initially amorphous layer is crystallized is probably related to the explosive nature of the crystallization.

### 3.1.3 Potential for cold cathode applications

The self-organized hillock structures have a great potential for cold cathode applications such as field emission displays. To demonstrate this, field emission measurements in a plane-to-plane configuration were performed. A stainless steel anode, 0.6 mm in diameter, was placed 1 to 20  $\mu\text{m}$  above the samples. Fig. 3.11 shows the emission current versus macroscopic electric field for laser-crystallized polycrystalline  $\text{Si}_{0.5}\text{Ge}_{0.5}$  on 30 nm (sample 1) and 500 nm (sample 2) molybdenum layers. Sample 1, which exhibited the self organization phenomenon, shows significantly better emission properties compared to sample 2 which did not contain a hillock structure. The electric field threshold to reach a current of 1 nA (dashed line in Fig. 3.11) is about 20  $\text{V}/\mu\text{m}$  for sample 1 as opposed to about 390  $\text{V}/\mu\text{m}$  for sample 2. The electron emission results are reproducible over several measurement cycles and independent of the vacuum gap. The emission threshold for sample 1 is similar to the one reported for single-crystal Si tips [47, 48], polycrystalline Si tips [47, 49, 50], Si nanowires [51], graphite films [52], and is higher than the typical values of 2-5  $\text{V}/\mu\text{m}$  reported for carbon nanotubes [53]. The lines in Fig. 3.11 are the fit to the data according to the Fowler-Nordheim

equation [54], assuming a work function of 4.4 eV [55]. The field enhancement factor derived from the fit for sample 1 amounts to  $\beta = 214$ . This value significantly exceeds the geometric field enhancement factor, which is defined as the ratio of the height to the radius of the hillocks [49] and amounts to  $\approx 2$ . Therefore, it can be concluded that the electron emission is greatly enhanced due to internal field enhancement.



**Fig. 3.11** Field emission current  $I$  as a function of macroscopic electric field  $E$  for two laser-crystallized polycrystalline  $\text{Si}_{0.5}\text{Ge}_{0.5}$  on molybdenum coated glass samples. Both samples were crystallized employing a step-by-step crystallization process. Sample 1 contained a 30 nm molybdenum layer and was crystallized with a final laser fluence of  $E_L = 380 \text{ mJ/cm}^2$ . The sample exhibited the self-organization phenomenon. Sample 2 contained a 500 nm molybdenum layer and was crystallized with a final laser fluence of  $E_L = 480 \text{ mJ/cm}^2$ . This sample did not exhibit self-organization.

Field emission display technology is considered promising [56], though it has not yet found its way into the display market. Much of the effort to produce appropriate cold cathode material for field emission displays has encountered difficulties with scaling to large areas [47], uniformity of emitting sites [50], screening by adjacent emitters [53], and emission stability [57]. The self-organized hillock structure has an advantage in that the emitters are formed at an easily tunable distance from each other with no need of a pre-structuring step, they can be produced with a good size uniformity, and the structure can be easily up-scaled to dimensions of  $1 \times 1 \text{ m}^2$ . Nevertheless, further investigation of the optimal distance between

emitters, the chemical stability of the SiGe layers, and the emission stability over time, is needed to ensure the performance of a display device.

## 3.2 Defect characterization

### 3.2.1 Electron spin resonance measurements

The study of paramagnetic defects in laser-crystallized polycrystalline SiGe thin films was carried out with the electron spin resonance (ESR) method. A typical ESR signal from a poly-Si<sub>0.5</sub>Ge<sub>0.5</sub> sample crystallized with a step-by-step process is shown in Fig. 3.12. The measurement was performed at 5 K since the signal to noise ratio increases significantly at low temperatures. Care was taken to choose the experimental parameters so that the ESR signal did not saturate. The main ESR resonance seen in Fig. 3.12 appears at a magnetic field of  $B_0 = 337$  mT and corresponds to  $g = h\nu/\mu_B B_0 = 2.0194$  (see Eq. 2.1). This resonance can clearly be identified as a Ge dangling-bond (DB) defect [58, 59]. The weaker resonance at  $B_0 = 337$  mT has a  $g$ -value of 2.003 and is most probably caused by the E' defect center [60] in the quartz substrate since this resonance was also observed when a bare quartz substrate was measured. This resonance, therefore, does not give any information about the SiGe layers. The Si dangling bond, which has a  $g$ -value of 2.0055 [61], was observed only in the laser-crystallized poly-Si. It was completely absent in Si<sub>0.67</sub>Ge<sub>0.33</sub>, which was the alloy with the lowest Ge content measured. The lack of a Si dangling-bond resonance for the SiGe alloys is not surprising since this resonance is expected to be weaker in intensity and not observable for  $x > 0.2$  [62].

The difference in the  $g$ -value of a Si DB compared to a Ge DB is related to the spin-orbit coupling. Such a coupling between the spin and the orbital angular momentum of the electron slightly modifies the Zeeman splitting and therefore causes  $g$  to differ from the value of a free electron  $g_e$ . The  $g$ -value variation follows approximately [63, 64]

$$\Delta g = g - g_e \propto \lambda_0, \quad (3.1)$$

where  $\lambda_0$  is the spin-orbit coupling factor. The large  $g$ -value for Ge is caused by a large spin-orbit coupling factor ( $940 \text{ cm}^{-1}$ ), which is about seven times larger than for Si ( $142 \text{ cm}^{-1}$ ) [58].

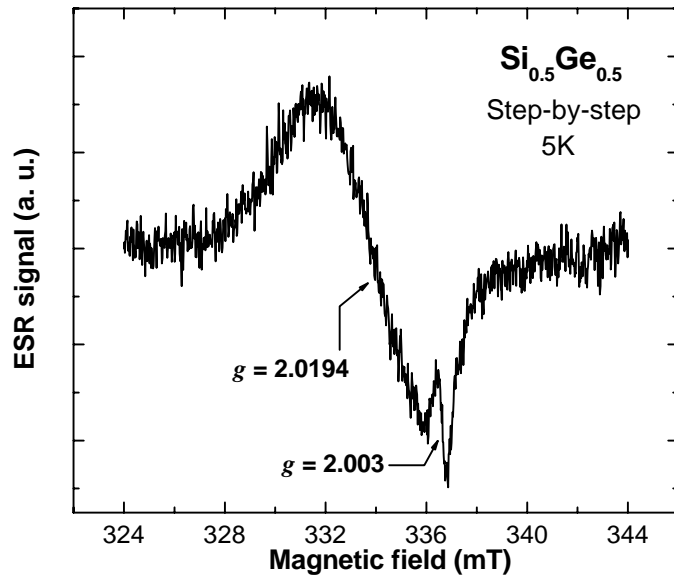


**Fig. 3.12** Electron spin resonance (ESR) signal measured on a laser-crystallized poly-Si<sub>0.5</sub>Ge<sub>0.5</sub> thin film on a quartz substrate. The measurement was performed at 5 K.

Although the main contribution of the dangling bond to the  $g$ -value stems from the central atom (Si or Ge) of the defect, the more distant surrounding of the defect may still have a significant influence. An indication for such an effect can be seen in Fig. 3.13, which shows the  $g$ -values of the Ge dangling-bond resonance of the laser-crystallized poly-SiGe films as a function of the Ge content  $x$ . The data exhibit a clear trend to higher  $g$ -values with increasing Ge content, which is consistent with results reported in the literature for amorphous SiGe [65, 66, 67]. The square data were taken from Lee et al. [66] and are included for comparison. Tight-binding calculations of a nine-atom Si cluster containing a dangling bond show that about 70 % of the wave function is localized on the central atom and about 10 % is localized at each of the three back-bond atoms [68]. Therefore, the contribution of the back-bond atoms to the ESR signal is not negligible. There are four different arrangements of back-bond atoms possible for a Ge dangling bond:  $-\text{Ge}\equiv\text{Si}_3$ ,  $-\text{Ge}\equiv\text{Si}_2\text{Ge}$ ,  $-\text{Ge}\equiv\text{SiGe}_2$ ,  $-\text{Ge}\equiv\text{Ge}_3$ . As the Ge content  $x$  in the SiGe alloy increases, the number of Ge atoms at the back bonding sites rises. This leads to an increase in the  $g$ -value due to the stronger spin-orbit coupling of Ge compared to Si.

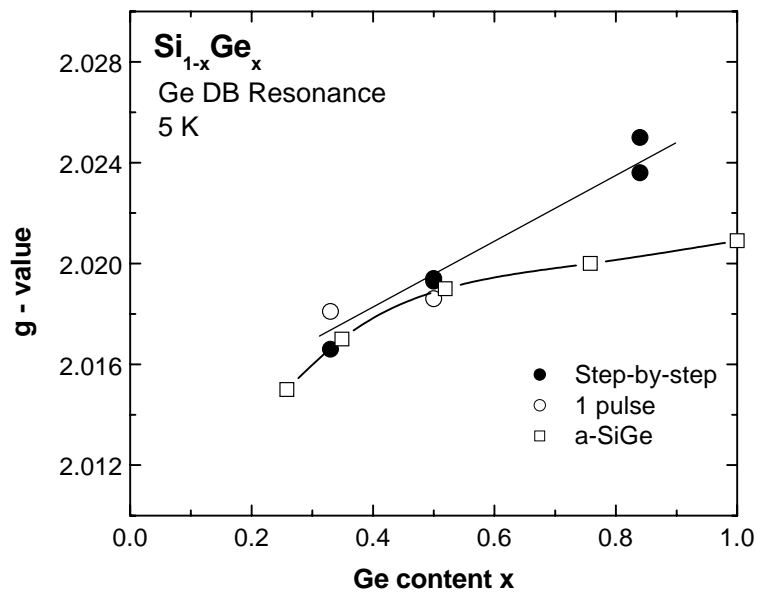


**Fig. 3.13** g-values of the Ge dangling bond as a function of Ge content  $x$  in  $\text{Si}_{1-x}\text{Ge}_x$ . The empty and full circles represent data from laser-crystallized poly-SiGe samples produced by a single pulse or a step-by-step process, respectively. The squares represent data from a-SiGe taken from Lee et al. [66].

The intensity of the ESR signal, if measured at sufficiently low microwave intensities, is proportional to the density of paramagnetic defects involved in the resonance. The proportionality factor in our case was derived by a comparison to an amorphous Si standard sample with a known number of dangling-bond defects. Fig. 3.14 shows the defect density  $N_s$  of dangling bonds as a function of the Ge content  $x$ . The full and empty circles represent poly-SiGe samples that were laser-crystallized with a step-by-step or a single pulse process, respectively. The empty squares represent poly-SiGe samples that were crystallized by annealing at 470 to 520 °C for several hours. The starting material for the solid phase crystallization was the same amorphous SiGe deposited on quartz that was used for the laser crystallization. It was not possible to thermally crystallize  $\text{Si}_{1-x}\text{Ge}_x$  with  $x < 0.5$  without severely damaging the samples.

Fig. 3.14 shows that laser-crystallized poly-SiGe samples exhibit a defect density of roughly  $N_s = 4 \times 10^{18} \text{ cm}^{-3}$ , whereas thermally crystallized samples have a defect density in the range of  $N_s = 7 \times 10^{17} \text{ cm}^{-3}$ . In both cases the defect density does not show a clear trend with varying Ge content  $x$ . The higher defect density of the laser-crystallized compared to the thermal-crystallized SiGe samples is in accordance with results reported for poly-Si by Nickel

et al. of  $N_s = 6 \times 10^{18} \text{ cm}^{-3}$  (laser crystallization) [69] and  $N_s = 2 \times 10^{18} \text{ cm}^{-3}$  (solid phase crystallization) [70].

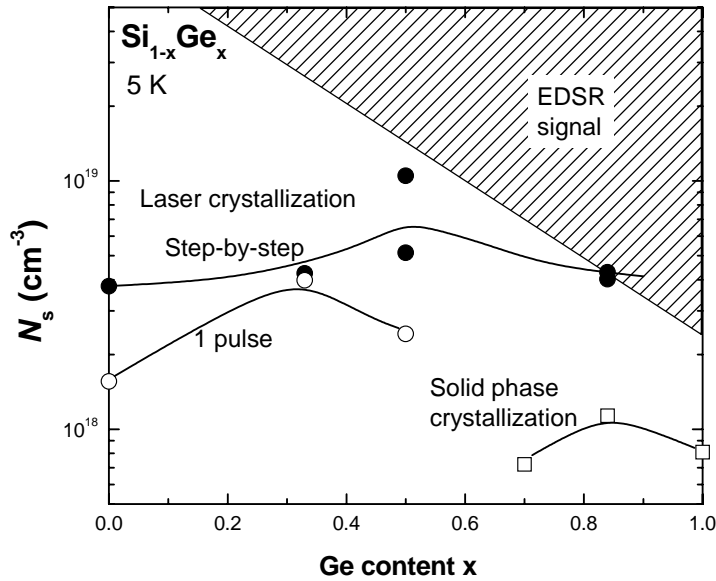


**Fig. 3.14** Defect density  $N_s$  as function of the Ge content  $x$  for laser-crystallized and thermally crystallized SiGe samples.  $N_s$  could not be determined in the dashed area where an electric dipole spin resonance (EDSR) signal was observed.

The dashed area in Fig. 3.14 represents the region where no typical ESR signal was observed for the laser-crystallized poly-SiGe samples and instead a broad asymmetrical signal appeared. An example is shown in Fig. 3.15. The width of this signal exceeds 50 mT, which is

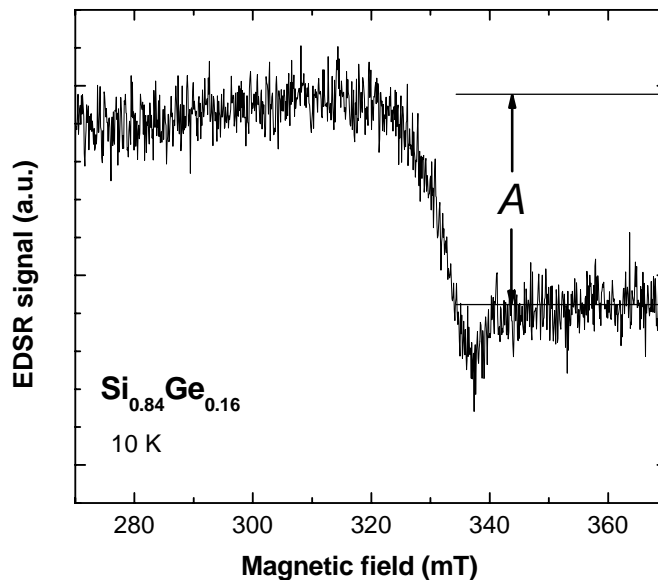


**Fig. 3.15** Electric dipole induced spin resonance (EDSR) signal measured on a laser-crystallized polycrystalline  $\text{Si}_{0.16}\text{Ge}_{0.84}$  thin film on a quartz substrate. The measurement was performed at 10 K.  $A$  is the step height of the signal

significantly larger than the value of  $\approx 4$  mT usually observed for the Ge dangling-bond resonance. In the following it will be shown that this signal is caused by electric dipole spin resonance (EDSR), which is a spin resonance between Zeeman levels caused by the electrical field of the microwave.

To demonstrate that the step-like signal shown in Fig. 3.15 originates from the electric field  $E_I$  instead of the magnetic field  $B_I$  of the microwave, measurements were performed with a sample positioned in the center (case 1) and at the edge of the sample holder (case 2). Fig. 3.16 shows the signal amplitude  $A$ , defined as the step height, as a function of the angle  $\varphi$  between the magnetic field  $B_0$  and the sample surface. Comparing the sample arrangements of case 1 and 2, a significant change in  $A$  can be seen especially for  $\varphi = 0^\circ$  and  $\varphi = 180^\circ$ . Since the sample is positioned in the middle region of the rectangular cavity operating in the  $TE_{102}$  mode, the gradient of  $E_I$  in this region is large compared to that of  $B_I$ . Therefore, the significant change in  $A$  observed upon a small shift in the position of the sample (about 1 mm) indicates that the signal is induced by  $E_I$  rather than  $B_I$ .

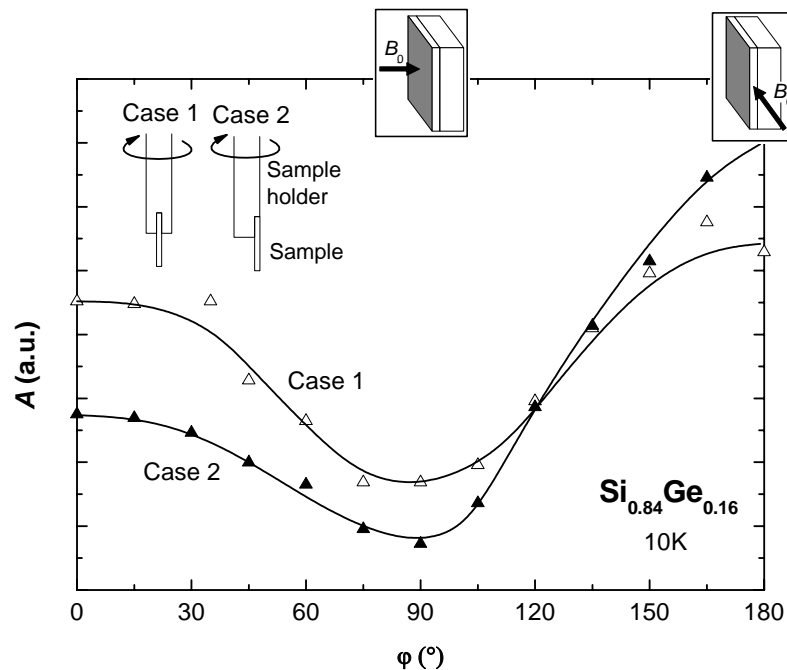


**Fig. 3.16** The step amplitude  $A$ , as defined in Fig. 3.15, of the electric dipole spin resonance (EDSR) signal of a laser-crystallized polycrystalline  $Si_{0.16}Ge_{0.84}$  thin film as function of the angle  $\varphi$  between the sample surface and the  $B_0$  field. Two cases are compared: sample positioned at (1) the center and at (2) the edge of the sample holder.

Fig. 3.17 shows the field distribution of  $E_I$  and  $B_I$  in the rectangular  $TE_{102}$  cavity. The sample holder was not positioned exactly at the 0-point in the cavity since in such a case no signal would have been observed in case 1 and the signal would have been equal in magnitude for  $\varphi = 0^\circ$  and  $\varphi = 180^\circ$  in case 2. Instead, as shown in Fig. 3.17, the sample holder is slightly off-center so that upon rotation, in case 1,  $A$  is equal for  $\varphi = 0^\circ$  and  $\varphi = 180^\circ$ , and in case 2,  $A$  is considerably smaller for  $\varphi = 0^\circ$  than for  $\varphi = 180^\circ$ .

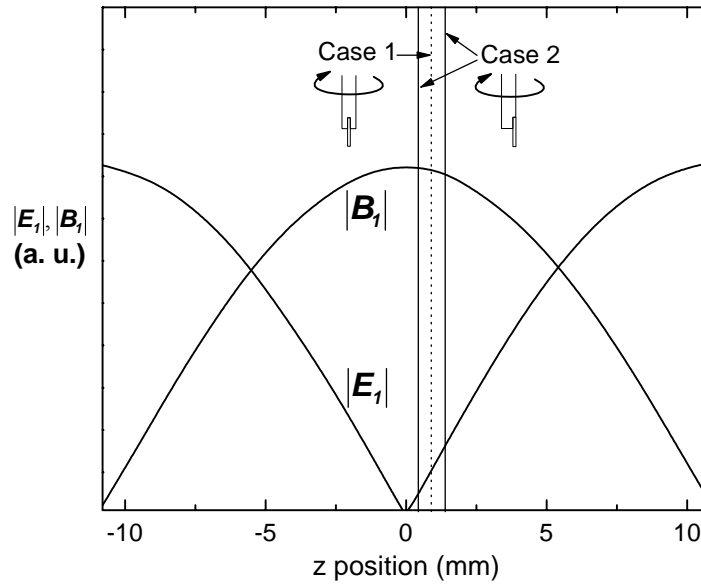


**Fig. 3.17** The distribution of the electric  $|E_I|$  and the magnetic  $|B_I|$  components of the microwave field in the rectangular  $TE_{102}$  cavity. The dashed line represents the position of the sample for case 1 and the solid lines for case 2 at  $\varphi = 0^\circ$  and  $\varphi = 180^\circ$ .

An electrically induced signal, such as the one shown in Fig. 3.15, can either originate from a cyclotron resonance [71] or from a spin resonance [72, 73, 74]. Since  $E_I$  is parallel to  $B_0$  in our experimental setup, the direct coupling of the electric field to the charge carrier motion, which is perpendicular to  $B_0$ , is not possible. This rules out the possibility that electron cyclotron resonance causes the observed signal. On the other hand, coupling of the  $E_I$  field to the charge carrier motion through the spin-orbit interaction follows the term in the spin Hamiltonian [75]

$$H_{SO} = \mu \cdot |\mathbf{E} \times \mathbf{P}| / 2m_0c \quad , \quad (3.2)$$

where  $\mu$  is the magnetic spin momentum,  $\mathbf{E}$  the electric field in which the electron moves,  $\mathbf{P}$  the momentum of the electron,  $m_0$  the mass of the electron and  $c$  the speed of light. In our case where  $\mathbf{P}$  is perpendicular to  $E_I$ , a non-vanishing spin-orbit interaction exists according to

Eq. 3.2, making it possible to attribute the signal in Fig 3.15 to an electric dipole spin resonance (EDSR).

An interesting detail that can be clearly seen in Fig. 3.16 is the appearance of a minimum for  $A$  at  $\varphi = 90^\circ$ . This minimum cannot be explained by a weaker  $E_I$  field for this sample orientation due to the off-center position of the sample holder in the cavity (see Fig. 3.17). Instead, it can be attributed to inhibited charge carrier motion for  $\varphi = 90^\circ$ . This can occur if the charge carriers do not move freely in the SiGe layer and are restricted to some specific areas such as the grain boundaries. The grain boundaries can be considered as two-dimensional surfaces that are perpendicular to the surface of the sample. For  $\varphi = 0^\circ$  and  $\varphi = 180^\circ$  carriers can cycle freely around the  $B_0$  vector in the plane of a grain boundary wall, as seen in Fig. 3.18 (a), whereas for  $\varphi = 90^\circ$  carriers are forced to move from one segment of a grain boundary to another (see Fig. 3.18 (b)). Since the radial motion of the carriers for  $\varphi = 90^\circ$  does not usually fit the grain boundaries structure, the motion is inhibited.

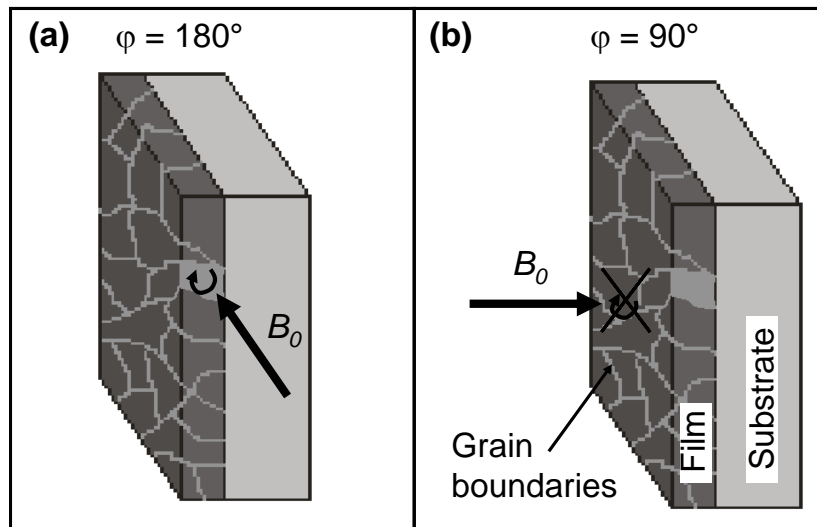


**Fig. 3.18** Schematic illustration of the charge carrier motion at the grain boundaries for (a)  $B_0$  parallel to the sample surface ( $\varphi = 0^\circ$  and  $\varphi = 180^\circ$ ) and (b)  $B_0$  perpendicular to the sample surface ( $\varphi = 90^\circ$ ). In case (b) the carrier motion is inhibited.

The interpretation that the EDSR signal arises from free carriers at the grain boundaries is supported by investigations performed on multicrystalline Si [73] and plastically deformed Si crystals [72, 74]. These studies observe EDSR signals and attribute them to highly conductive long defect lines and grain boundaries. Moreover, the conductivity measurements presented in the next section strengthen the conclusions derived here by

showing a dramatic increase in the conductivity across the sample when an EDSR signal is observed.

### 3.2.2 Electrical conductivity and hydrogen post-treatment

Conductivity measurements that were performed on laser-crystallized poly-SiGe samples showed a strong deviation from the behavior expected of a semiconductor material. Fig. 3.19 shows the dark conductivity  $\sigma_D$  as a function of the reciprocal temperature for poly-Si<sub>1-x</sub>Ge<sub>x</sub> with  $x = 0.5$  and  $x = 0.84$  crystallized with a step-by-step process. For  $x = 0.5$  the conductivity decreases from  $\sigma_D = 1.8 \times 10^{-1}$  S/cm to  $\sigma_D = 1.7 \times 10^{-5}$  S/cm by four orders of magnitude as the temperature decreases to 70 K. On the other hand, for  $x = 0.84$   $\sigma_D$  is nearly constant in the temperature range of 20 to 100 K and amounts to  $\sigma_D = 7 \times 10^{-1}$  S/cm. This nearly temperature-independent conductivity, typically seen in metals, is more likely to occur as the Ge content increases in the alloy. Moreover, it is inevitable for laser-crystallized poly-Ge films. Interestingly, the conductivity results directly correlate with the electron spin resonance results presented in Sec. 3.2.1. Samples that exhibit electric dipole spin resonance (EDSR) signal show metallic-like conductivity, whereas samples that exhibit an ESR signal show temperature-activated conductivity. It should also be noted that according to Hall effect measurements, the majority carriers are holes for all samples with a Ge content of  $x \geq 0.3$ .

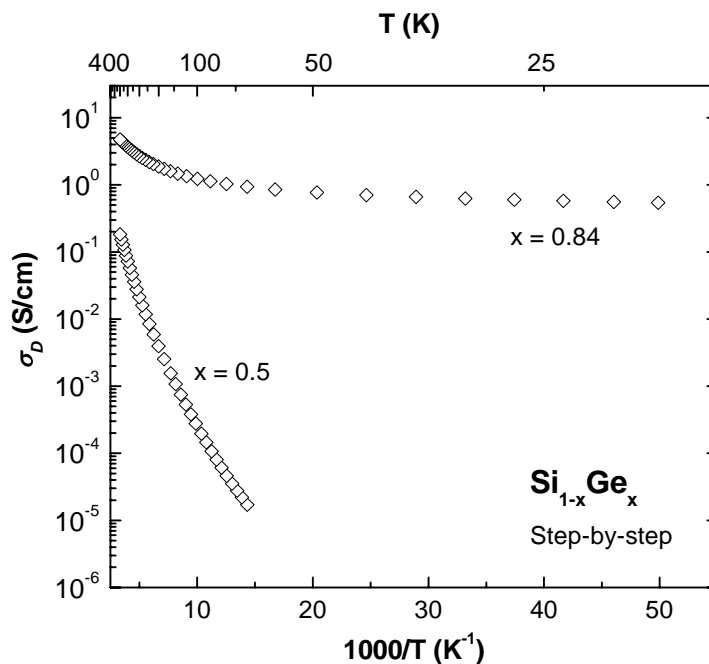


**Fig. 3.19** Electrical dark conductivity  $\sigma_D$  of poly-Si<sub>1-x</sub>Ge<sub>x</sub> films with  $x = 0.5$  and  $x = 0.8$ , crystallized with a step-by-step laser process, as function of the reciprocal temperature.

A well established approach to improving the electronic and structural properties of amorphous and polycrystalline silicon is to incorporate hydrogen into the material. In many cases, this results in the passivation and neutralization of electrically active defects, which is crucial for device applications. The influence of hydrogen on the electrical dark conductivity of a laser-crystallized poly-Si<sub>0.5</sub>Ge<sub>0.5</sub> film crystallized with a single pulse is shown in Fig. 3.20. The sample was heated to 266 °C and exposed to monatomic hydrogen plasma for a time  $t_H$  varying from  $1.8 \times 10^3$  to  $72 \times 10^3$  s. The unhydrogenated film shows a metallic-like conductivity with a saturation value of  $\sigma_D = 1.2 \times 10^{-1}$  S/cm at low temperatures. Post-hydrogenation for  $1.8 \times 10^3$  s results in a decrease of the conductivity of more than two orders of magnitude to  $\sigma_D = 5.9 \times 10^{-4}$  S/cm at 20 K. Longer hydrogenation times cause the conductivity to decrease further. Ultimately, for very long passivation times, the temperature dependence of  $\sigma_D$  approaches activated behavior. Similar changes in conductivity upon post-hydrogenation were also observed for poly-Si<sub>0.16</sub>Ge<sub>0.84</sub>, crystallized with a step-by-step laser process. These results demonstrate that H influences the electrical transport significantly and causes a transition from metal-like to semiconductor or insulator-like transport. It should be noted that the reduction in  $\sigma_D$  upon hydrogenation is contrary to the common observation in poly-Si of an increase in  $\sigma_D$  due to H incorporation [76].

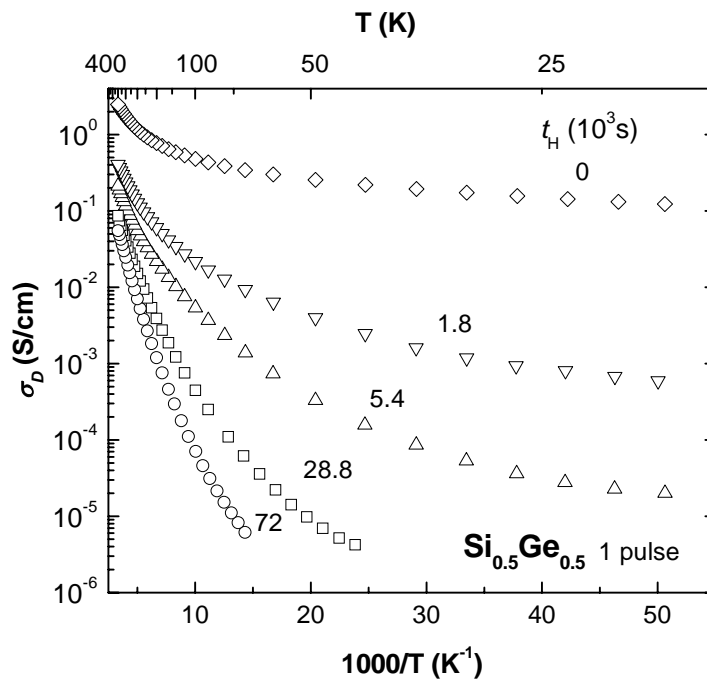


**Fig. 3.20** Temperature dependence of the electrical dark conductivity  $\sigma_D$  of a laser-crystallized poly-Si<sub>0.5</sub>Ge<sub>0.5</sub> film that was exposed to monatomic H at 266 °C for the indicated times  $t_H$ . The sample had a thickness of  $\approx 100$  nm.

In order to elucidate how H causes the decrease in conductivity shown in Fig. 3.20, the incorporation of deuterium ( $^2\text{H}$ ) into the thin film was studied with secondary ion mass spectrometry (SIMS). Deuterium is often used as a tracer element for SIMS experiments since it can be sensitively detected. Moreover, it allows one to differentiate between the residual H and the newly incorporated D. Most of the studies in this field agree that there is no significant difference in the diffusion and chemical bonding between deuterium and hydrogen and therefore they can be used interchangeably [77, 78, 79, 80]. Fig. 3.21 shows D concentration profiles obtained from hydrogenated amorphous germanium (a-Ge:H). The samples were exposed to monatomic D plasma for 1800 s at substrate temperatures ranging from 150 to 400 °C. Deuterium diffuses deeper into the layer with increasing substrate temperature. The near surface increase in the concentration is an artifact of the SIMS technique. The hydrogen concentration profile is given by the dashed line.

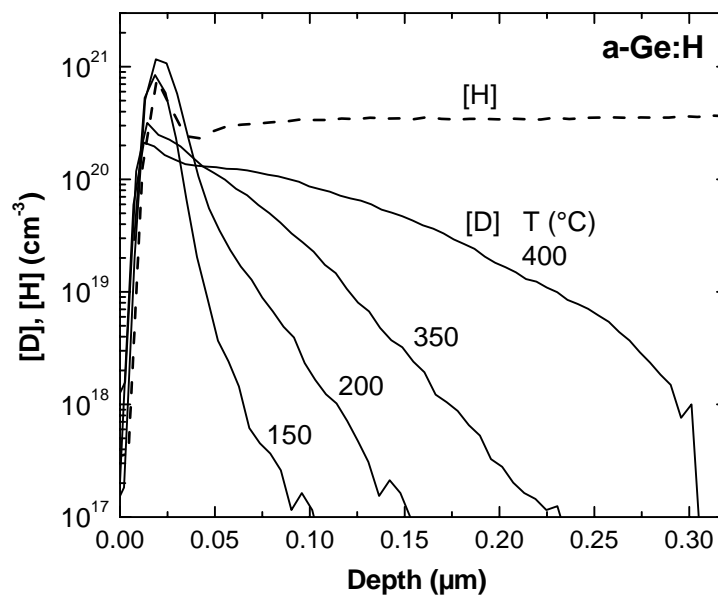


**Fig. 3.21** Deuterium and hydrogen concentration depth profiles of a-Ge:H thin films. The specimens were exposed to monatomic D for 30 min at the specified temperatures. The H concentration depth profile in the films prior to the deuteration treatment is given by the dashed line.

The depth profiles shown in Fig. 3.21 were analyzed by fitting the concentration values to a complementary error-function solution of the diffusion equation [81]

$$C(x, t) = C_0 \left( \operatorname{erfc} \left( \frac{x}{\sqrt{4D_{\text{eff}}t}} \right) \right) \quad , \quad (3.3)$$

where  $D_{\text{eff}}$  is the effective diffusion coefficient,  $C_0$  is the deuterium surface concentration,  $x$  is the distance from the surface, and  $t$  is the diffusion time. The diffusion coefficient derived from this analysis is considered to be an effective one since the hydrogen migration properties change during the exposure as the H concentration increases [82]. Additionally, the migration properties vary spatially in accordance with the local microstructure at the grains and at the grain boundaries [79]. Fig. 3.22 shows  $D_{\text{eff}}$  as a function of the reciprocal temperature for a-Ge:H and laser-crystallized poly-Si<sub>1-x</sub>Ge<sub>x</sub> with  $x = 0.22, 0.45,$  and  $1$ . The data can be fitted to the equation

$$D_{\text{eff}} = D_0 \cdot \exp\left(-\frac{E_A}{kT}\right) \quad (3.4)$$

where  $D_0$  is a prefactor,  $k$  is the Boltzmann constant,  $T$  is the temperature, and  $E_A$  is the slope of the curve and not the activation energy as explained below. The values obtained for  $E_A$  from the fit to the data in Fig. 3.22 are 0.07-0.16 eV for laser-crystallized poly-SiGe and 0.31 eV for a-Ge:H.  $E_A$  becomes smaller with increasing Ge content in the laser-crystallized poly-SiGe samples.

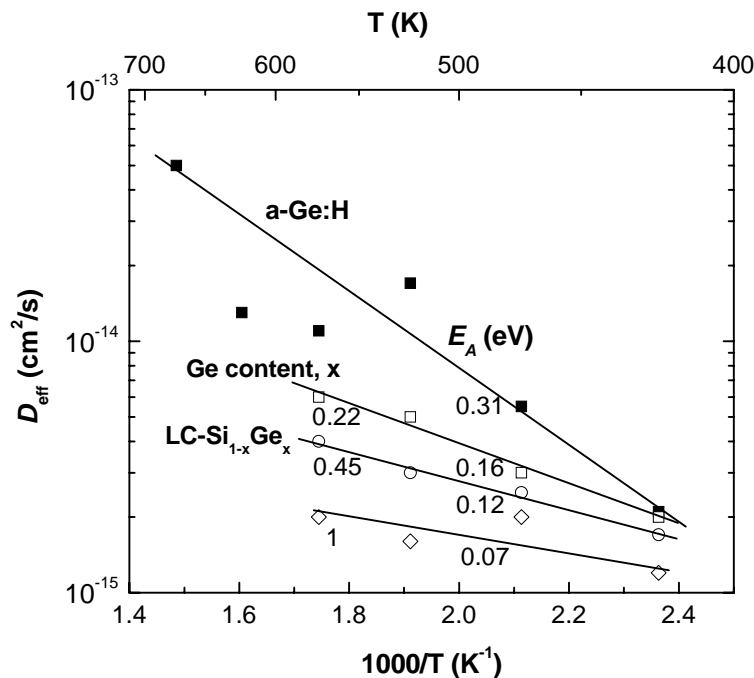


**Fig. 3.22** Effective diffusion coefficient of a-Ge:H and laser-crystallized poly-Si<sub>1-x</sub>Ge<sub>x</sub> films with  $x = 0.22, 0.45,$  and  $1$ , as function of the reciprocal temperature. The values  $E_A$  indicated in the figure were obtained from the slope of the lines.

Plotting  $D_0$  against  $E_A$  is a useful way to demonstrate why  $E_A$  cannot be considered as activation energy. Fig. 3.23 shows the results obtained in this study for  $D_0$  and  $E_A$ , which are given by the full symbols. The empty symbols represent results published for a-Si (squares),  $\mu\text{c-Si}$  (circles), and poly-Si (triangles) [83]. The prefactor  $D_0$  increases by more than 15 orders of magnitude with increasing  $E_A$ , and all data points follow a straight line independent of microstructure and chemical properties of the host material. This kind of a relation between  $E_A$  and  $D_0$  is known as Meyer-Neldel rule [84]. The fact that  $D_0$  depends on  $E_A$  indicates that  $E_A$  cannot be attributed directly to the energy separation between the H trapping sites and the H transport level. The observed Meyer-Neldel behavior suggests that  $E_A$  takes into account a temperature-dependent mechanism such as, perhaps, a statistical shift in the non-equilibrium occupation of the density of states [85].

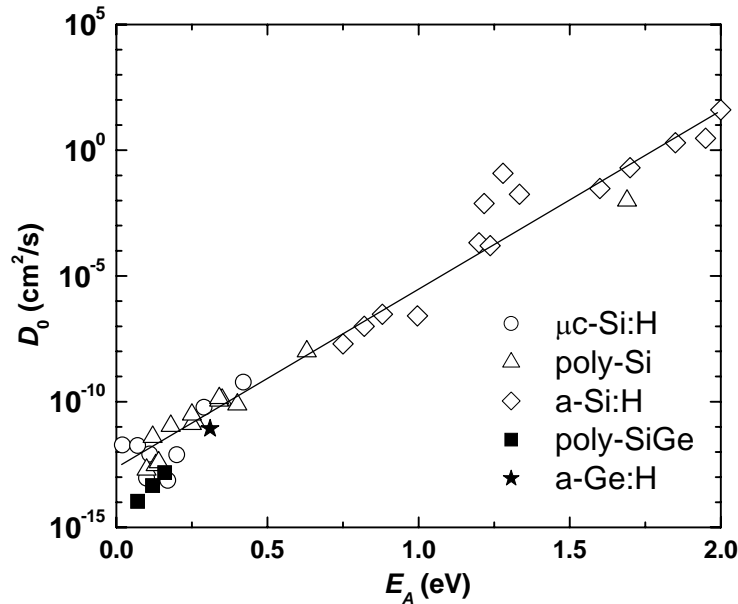


**Fig. 3.23** Diffusion prefactor  $D_0$  as function of  $E_A$ . The full star and squares represent the values obtained from this study for a-Ge:H and laser-crystallized poly-SiGe, respectively. The empty squares, circles, and triangles represent data reported for a-Si,  $\mu\text{c-Si}$ , and poly-Si, respectively [83].

For laser-crystallized poly-Si<sub>0.55</sub>Ge<sub>0.45</sub>, the analysis of the SIMS results presented above yields an effective diffusion coefficient of  $D_{\text{eff}} \approx 3.4 \times 10^{-15} \text{ cm}^2/\text{s}$  at 266 °C. Using this value to estimate the time it would take for hydrogen to penetrate all the way through a 100 nm thick Si<sub>0.5</sub>Ge<sub>0.5</sub> film, such as the one used for the conductivity measurements presented in Fig 3.20, results in a diffusion time of  $t_H \approx 6 \times 10^3 \text{ s}$ . This diffusion time fits quite well with the time needed to see a significant change in the conductivity behavior, going from metallic to insulator-like in character (see Fig. 3.20). Therefore, the SIMS analysis contradicts the idea

that the metallic-like conductivity is caused by surface conductance, as will be further discussed in Sec. 4.2.1. It will be suggested there that the mechanism behind the conductivity change is the passivation of dangling-bond defects at the grain boundaries by hydrogen. This mechanism fits the fact that upon hydrogenation, a reduction of the ESR Ge dangling-bond signal was observed. This reduction corresponds to a decrease in the spin density from  $N_s \approx 4 \times 10^{18}$  to  $\approx 6 \times 10^{17} \text{ cm}^{-3}$ .

On the other hand, photoconductivity measurements provide an indication that H incorporation might also induce non-beneficial effects for device applications. Fig. 3.24 presents the photoconductivity of a laser-crystallized poly-Si<sub>0.5</sub>Ge<sub>0.5</sub> thin film before and after hydrogen plasma treatment with the same parameters as before ( $T = 266 \text{ }^\circ\text{C}$  and  $t_H = 72 \cdot 10^3 \text{ s}$ ). The photoconductivity is defined here as  $\sigma_{\text{ph}} = \sigma_L - \sigma_D$ , where  $\sigma_L$  is the conductivity measured under white light illumination. The white light had the characteristic spectrum of a black body at 3000 K. The results in Fig. 3.24 show that the photoconductivity of the non-treated poly-Si<sub>0.5</sub>Ge<sub>0.5</sub> film is more than an order of magnitude larger than the treated one. For example, at the highest irradiation power of  $0.75 \text{ Watt/cm}^2$ ,  $\sigma_{\text{ph}} = 0.24 \text{ S/cm}$  for the non-treated film and  $\sigma_{\text{ph}} = 0.021 \text{ S/cm}$  for the hydrogenated sample. A similar photoconductivity reduction upon plasma hydrogenation was also observed for laser-crystallized poly-Si<sub>0.2</sub>Ge<sub>0.8</sub> films.

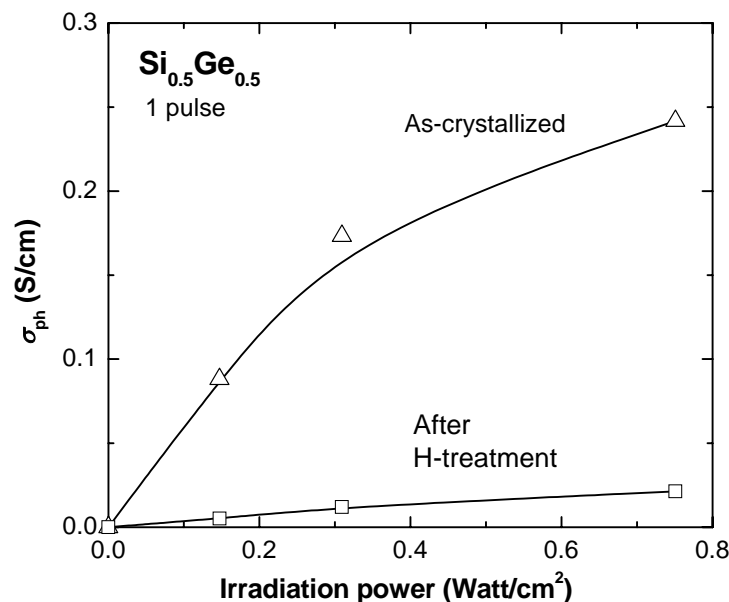


**Fig. 3.24** Photoconductivity  $\sigma_{\text{ph}}$  of laser-crystallized poly-Si<sub>0.5</sub>Ge<sub>0.5</sub> thin film before and after exposure to monatomic hydrogen plasma as function of the irradiation power. The measurements were performed at room temperature.

The photoconductivity can be assigned in many practical cases to the excited majority charge carriers (holes in our case) according to

$$\sigma_{\text{ph}} = eG\mu_p\tau_p \quad , \quad (3.5)$$

where  $e$  is the electron charge,  $G$  is the charge generation rate by light excitation,  $\mu_p$  is the mobility, and  $\tau_p$  is the life time of the holes. The decrease in  $\sigma_{\text{ph}}$  upon hydrogenation is therefore proportional to the decrease in the  $\mu_p\tau_p$  product. In Sec. 4.2.2 it is suggested that such a decrease might be attributable to the generation of large two-dimensional hydrogen clusters known as platelets during the hydrogen plasma treatment, which act as active recombination centers [36].

### 3.2.3 Optical absorption

One of the most attractive properties of SiGe alloys for opto-electronic devices is their enhanced optical absorption compared to Si. The study of the optical absorption in laser-crystallized poly-SiGe thin films was carried out with the photothermal deflection spectroscopy (PDS) method, which is particularly sensitive to sub-band-gap absorption. The optical absorption in the material is characterized by the absorption coefficient  $\alpha$ , defined by the equation (Beer's law)

$$I(x) = I_0 \exp(-\alpha x) \quad , \quad (3.6)$$

where  $I_0$  is the incident light intensity at the surface and  $I(x)$  is the light intensity at a distance  $x$  from the surface.

The results of the absorption coefficient  $\alpha$  for step-by-step laser-crystallized poly-Si<sub>1-x</sub>Ge<sub>x</sub> thin films with  $x = 0, 0.5, 0.8,$  and  $1$ , at the photon energy range  $0.6 < h\nu < 2.8$  eV, are plotted in Fig. 3.25(a). Interference fringes were analyzed carefully and smoothed out. For comparison, the absorption coefficient  $\alpha$  of crystalline germanium (c-Ge) [16], crystalline silicon (c-Si) [17], and hydrogenated amorphous silicon (a-Si:H) [86] are also shown. The absorption curves of the laser-crystallized poly-SiGe films fit well between the c-Si and the c-Ge references and exhibit the expected trend of increasing  $\alpha$  with increasing Ge content  $x$ .

However, the shape of these curves for  $x = 0.5, 0.8,$  and  $1$  deviate significantly from the crystalline samples. To make this difference in the shape of the absorption curve clearer, Fig. 3.25(b) shows the data in a Tauc plot  $((\alpha h\nu)^{0.5}$  vs.  $h\nu$ ) [87]. The absorption coefficient of many amorphous semiconductors exhibits in this plot a straight line at photon energies above the absorption edge, thus obeying the relation

$$\alpha(\nu) = \frac{B_m (h\nu - E_g)^2}{h\nu} \quad , \quad (3.7)$$

where  $B_m$  is a material specific constant and  $E_g$  is the optical band-gap. As can be seen from

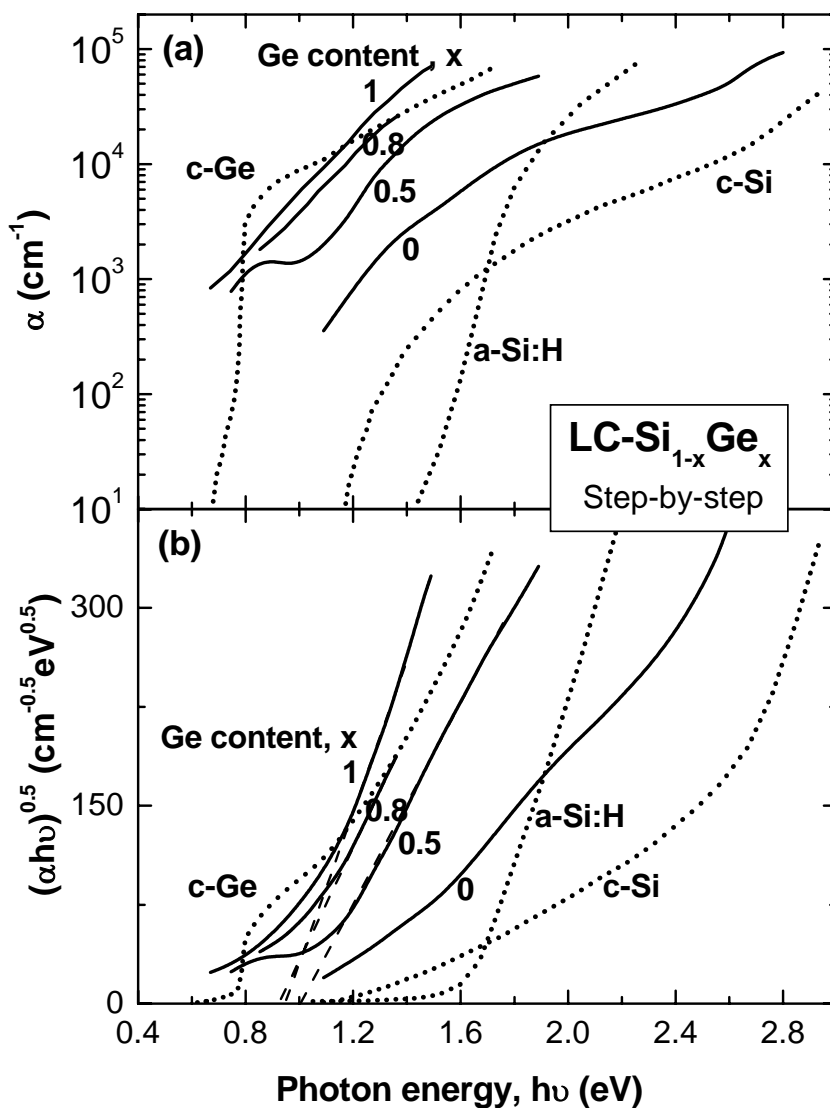


**Fig. 3.25** Optical absorption properties of laser-crystallized poly-SiGe thin films compared to c-Si [17], c-Ge [16], and a-Si:H [86]. The poly-Si<sub>1-x</sub>Ge<sub>x</sub> films were crystallized with a step-by-step process and their Ge content  $x$  is specified in the figure. (a) shows the absorption coefficient  $\alpha$  as function of the photon energy  $h\nu$ , and (b) shows a Tauc plot of the data (for details see text).

Fig. 3.25(b), a-Si:H follows Eq. 3.7 and exhibits a straight line for  $h\nu > 1.6$  eV whereas c-Si and c-Ge do not. More surprising, however, is the finding that the laser-crystallized poly-Si<sub>1-x</sub>Ge<sub>x</sub> films with  $x = 0.5, 0.8,$  and  $1$  exhibit a nearly straight line in the Tauc plot (marked with a dashed line in Fig. 3.25(b)). This result indicates that the absorption of the Ge-rich poly-SiGe films is probably dominated by the disordered areas in the layer, namely the grain boundaries. It should be noted that the first direct optical transition  $E_0$  of c-SiGe at the  $\Gamma$  point decreases from  $h\nu = 3.9$  eV for c-Si to  $h\nu = 0.83$  eV for c-Ge [88]. This transition that occurs in the crystalline grains might become significant for the laser-crystallized poly-Ge samples. Nevertheless, this transition is probably not the reason for the straight line in the Tauc plot for  $x = 1$  because it is expected to produce a different absorption curve shape and because it has a lower transition probability compared to direct transitions induced by disorder at the grain boundaries.

The optical band-gap  $E_g$  is often determined for amorphous semiconductors by extrapolating the straight line in the Tauc plot to  $(\alpha h\nu)^{0.5} = 0$ . This procedure mostly determines values somewhat smaller than for the mobility band-gap determined from electrical measurements. Davis and Mott [89] have argued that the optical band-gap is a little smaller than the mobility band-gap since it is determined by transitions from localized tail states in the valence (conduction) band to delocalized states in the conduction (valance) band. The mobility band-gap, in contrast, is determined by the energy separation between the delocalized states in the conduction and the valance band.

The optical band-gap of the laser-crystallized poly-Si<sub>1-x</sub>Ge<sub>x</sub> films with  $x \geq 0.3$  was determined from the Tauc plot and the results are summarized in Tab. 3.1. The fits for  $x = 0.3$  were less reliable indicating, possibly, that for  $x \lesssim 0.3$  the absorption is not as strongly dominated by the grain boundaries. The error of the estimated band-gap was about  $\pm 0.05$  eV for  $x = 0.3$  and about  $\pm 0.02$  eV for the other samples. Optical band-gap  $E_g$  values derived from the as-deposited a-SiGe:H films are also indicated in the table for comparison. The values of  $E_g$  for laser-crystallized SiGe films are somewhat smaller than for the a-SiGe:H films but much closer to them than to the indirect band-gap values of c-SiGe, which vary from 1.1 eV for c-Si to 0.67 eV for c-Ge. There is also a difference in  $E_g$  between laser crystallization with a step-by-step and with a single step process. The lower values of  $E_g$  obtained with the single pulse process might be related to the lower amount of hydrogen in these samples of about  $5 \times 10^{19}$  cm<sup>-3</sup> compared to about  $5 \times 10^{21}$  cm<sup>-3</sup> for the step-by-step

samples. The increase of the band-gap of a-Si upon hydrogen incorporation is a well known phenomenon [90, 91, 92] and the effect can also be seen in Tab 3.1 for the poly-Si<sub>0.5</sub>Ge<sub>0.5</sub> films that were exposed to monatomic hydrogen plasma. The hydrogen post-treatment was carried out at a substrate temperature of 266 °C for a duration  $t_H = 7.2 \times 10^4$  s and  $t_H = 5.4 \times 10^3$  s for the samples crystallized with a single pulse and a step-by-step crystallization technique, respectively.

**Tab. 3.1** Optical band-gap  $E_g$  of laser-crystallized poly-SiGe and as-deposited a-SiGe:H thin films.  $E_g$  was determined from a Tauc plot (see Fig. 3.25(b))

Ge content x	$E_g$ (eV)		
	Poly-SiGe Step-by-step	Poly-SiGe 1 pulse	a-SiGe:H
0.3	1.27	1.18	1.28
0.5	1.02	0.98	1.25
	H-treatment	1.16	1.12
0.84	0.93	0.91	0.98
1	0.95	0.95	0.92

Another detail in Fig. 3.25 that should be noted is the appearance of a sub-band-gap absorption peak for laser-crystallized poly-Si<sub>0.5</sub>Ge<sub>0.5</sub>. This absorption peak was closely examined before and after the hydrogen treatment. The results for the step-by-step and the single pulse crystallization processes can be seen in Fig. 3.26. Applying a hydrogen post-treatment causes the sub-band-gap peak to shift to higher photon energies and to decrease in magnitude.

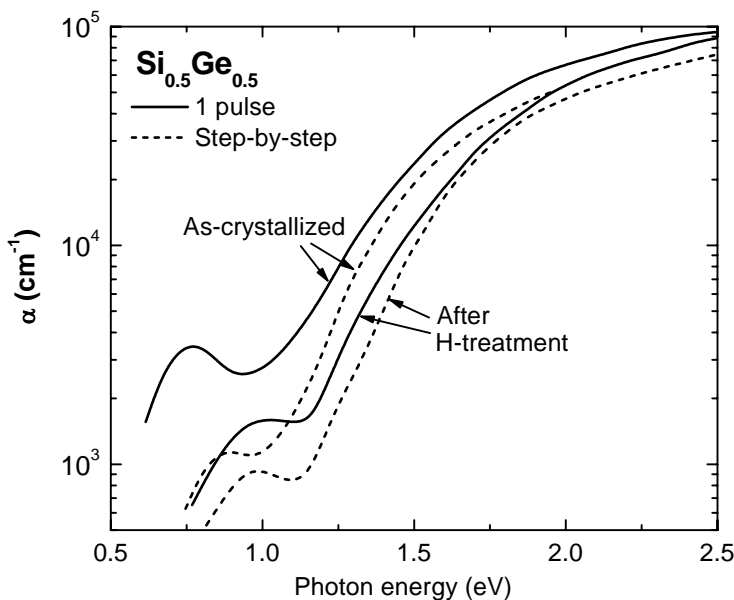


**Fig. 3.26** Absorption coefficient  $\alpha$  as function of the photon energy of poly-Si<sub>0.5</sub>Ge<sub>0.5</sub> before and after applying a hydrogen plasma treatment. Solid lines represent samples that were crystallized with a single laser pulse and dashed lines represent samples that were crystallized with a step-by-step process. The curves show an absorption peak below the absorption edge that upon hydrogenation shifts to higher energies and decreases in magnitude.

**Tab. 3.2** Properties of the sub-band-gap absorption peak in laser-crystallized poly-Si<sub>0.5</sub>Ge<sub>0.5</sub>.  $E_P$  represents the photon energy where the peak was observed and  $\Delta E$  is taken as  $E_g - E_P$ .

Sample details		$E_P$ (eV)	$\Delta E$ (eV)
Step-by-step	As-crystallized	0.88	0.14
	H post-treatment	0.97	0.19
1 pulse	As-crystallized	0.77	0.21
	H post-treatment	1.01	0.11

The data in Tab. 3.2 show that the sub-band-gap absorption observed for poly-Si<sub>0.5</sub>Ge<sub>0.5</sub> arises from optical transitions corresponding to an energy that is smaller by 0.11 to 0.21 eV than the optical band-gap energy. In Sec. 4.2.2 of the discussion, it will be suggested that these transitions are probably from dangling-bond states near the valance band to conduction-band states.

To conclude, in this chapter structural and defect properties of laser-crystallized poly-SiGe thin films have been presented. It has been shown that laser crystallization of Si<sub>1-x</sub>Ge<sub>x</sub> thin films with  $0.3 < x < 0.7$  can result in a self-organized pattern of hillocks or ripples, which is directly coupled to a periodic compositional variation. The elevated areas of the hillocks and ripples are enriched with Ge whereas the lowered areas are depleted of Ge. This phenomenon is sensitive to various experimental parameters such as laser fluence, number of laser pulses, Ge content, substrate choice, and initial state of the layer, e.g.: amorphous or crystalline. The study of defects with ESR showed that the Ge-rich SiGe thin films exhibit an atypical electric dipole spin resonance signal that can be attributed to a large number of free carriers at the grain boundaries. This result is consistent with the appearance of a nearly temperature-independent conductivity for these samples in the range of 20 - 100 K. Moreover, indications have been found that the optical absorption of the Ge-rich SiGe specimens occurs primarily at the grain boundaries. Finally, the incorporation of H into the SiGe films dramatically modified their electrical and optical properties, causing: (i) a transition from metallic to insulator-like conductivity, (ii) a reduction of the electron spin resonance signal of the Ge dangling bonds, (iii) a widening of the optical band-gap, (iv) a reduction in the sub-band-gap absorption, and (v) a reduction in the photoconductivity.

## 4 Discussion

The experimental results show that a compositional and topographic pattern appears after laser irradiation of  $\text{Si}_{1-x}\text{Ge}_x$  thin films with  $0.33 < x < 0.7$ . In addition, the electronic transport and optical absorption of the SiGe films are critically influenced by the grain boundaries and are sensitive to subsequent hydrogen incorporation treatment. A model that accounts for the pattern formation is discussed in Sec. 4.1. The electronic and optical properties of the films are treated in Sec. 4.2 where a model based on the formation of a defect band along grain boundaries at the vicinity of the Fermi level in the band-gap is presented. Finally, the effect of defect generation during the hydrogen treatment is discussed in Sec. 4.3.

### 4.1 Pattern formation based on the Mullins-Sekerka instability

This section aims to elucidate the mechanism behind the compositional and topographic pattern formation that is observed in laser-crystallized poly- $\text{Si}_{1-x}\text{Ge}_x$  with  $0.3 < x < 0.7$  (see Sec. 3.1.1). The formation of periodic structures on the surface upon laser irradiation has been primarily reported in the literature for silicon single crystals [5, 93, 94, 95, 96, 97, 98, 99]. In some cases [93, 94, 95], the structure formation was attributed to an interference between the incident laser light and the light scattered from the sample surface. The interference induces a periodic modulation of the temperature near the surface that gives rise to a surface structure due to lateral liquid flow or differential ablation. Interference on the surface can be excluded as an explanation for our observations since (i) it requires linear polarized laser light and our XeCl excimer laser emits unpolarized light, (ii) the structure appears at a laser fluence near the surface melting threshold whereas in our case it appears at a wide laser fluence range, and (iii) the wavelength of the structure is close to that of the laser whereas in our case the wavelength of the structure varies from 0.3 to 2  $\mu\text{m}$  compared to that of the laser (0.308  $\mu\text{m}$ ).

Another mechanism, based on the excitation of capillary waves on the surface, has recently been proposed to explain the formation of structures with periodicity lengths larger than the laser wavelength. According to this mechanism, capillary waves are excited shortly

after irradiation and are captured on the surface at the final stage of the solidification. The periodicity length of the structure one would expect in such a case can be roughly estimated from the dispersion relation for shallow waves as [100]

$$d = (\gamma \cdot h / \rho)^{1/4} (2\pi \cdot t_m)^{1/2}, \quad (4.1)$$

where  $\gamma$  is the surface tension coefficient,  $h$  is the melt depth,  $\rho$  is the density, and  $t_m$  is the melt duration. Eq. 4.1 is based on the assumption that the excitation with the longest possible wavelength is dominant due to the relaxation behavior of capillary waves [101]. According to this equation the periodicity length  $d$  increases with an increase in the melt duration  $t_m$ . However, this contradicts the experimental data presented in Fig. 3.6 where  $d$  decreases at the complete melting regime. Moreover, this model cannot account for the strong influence of the Ge content  $x$  on the periodicity length  $d$  (see Fig. 3.6) or for the suppression of the structure formation for  $x < 0.3$ . Thus, the excitation of capillary waves alone cannot explain the structure formation but in combination with the instability mechanism, as discussed below, may be able to do so.

The appearance of periodic cellular structures with a high dopant concentration on the cell wall, formed upon laser irradiation of silicon crystals implanted with Indium (In), Gallium (Ga), Iron (Fe), Antimony (Sb), and Tin (Sn), has been assigned to the instability of the solid-liquid interface [98, 102]. According to this model, originally developed by Mullins and Sekerka [31], the planar shape of the moving solid-liquid interface breaks down during solidification into a periodically modulated interface and causes the appearance of the structure during solidification.

In the following discussion, it is suggested that the instability mechanism dominates the pattern formation for laser-crystallized SiGe thin films. A schematic illustration of how this mechanism works is presented in Fig. 4.1. The solidification starts at time  $t_0$  shortly after the irradiation. At time  $t_1$  the solid-liquid interface exhibits a periodic modulation due to the instability of the system. The periodicity length and amplitude of the modulation grow rapidly until time  $t_2$  is reached. At the final stage, the SiGe liquid piles up in the last areas to solidify due to the trapping of capillary waves between coalescing solid boundaries. The volume difference between the solid and the liquid phase is most probably the source of excitation of the capillary waves [101].

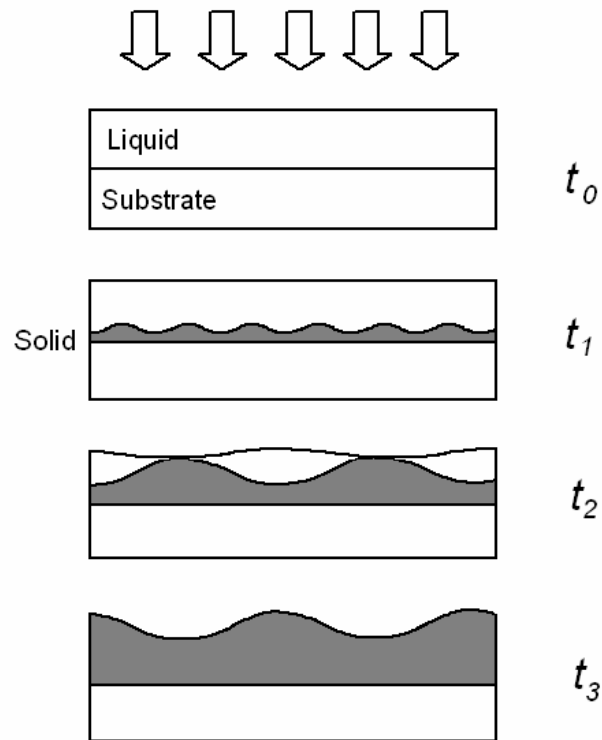


**Fig. 4.1** Schematic illustration of the structure formation on the film surface after a single laser pulse.

An attempt is now made to describe the onset conditions of the instability in terms of the Mullins-Sekerka perturbation theory [31]. This theory assumes that an infinitesimal sinusoidal perturbation of the form  $z = \delta(t)\sin(\omega X)$  is introduced to a planar solid-liquid interface that propagates with a constant velocity  $v$ .  $\delta(t)$  is the time dependent perturbation amplitude and  $\omega$  is the spatial frequency. The solid-liquid interface is unstable if there is a sinusoidal perturbation  $\omega$  for which  $\delta$  grows in time ( $\dot{\delta} = d\delta/dt > 0$ ). On the other hand, it is stable if all perturbations decay.

The assumption of a planar solid-liquid interface is justified since the grain size in our layers is typically smaller than the layer thickness and the crystal growth occurs mainly in the vertical direction. In addition, it has been shown that the periodicity length of the self-organized structure does not correlate with the grain size but is about one order of magnitude larger (see Fig. 3.1). Thus, even if there is some modulation in the solid-liquid interface during solidification in accordance with the periodicity length of the grain size, it does not destabilize the interface and can be disregarded in our analysis.

Mullins and Sekerka derived the following expression for  $\dot{\delta}$  by solving the steady-state heat flow and diffusion equations with the appropriate boundary conditions and the interface perturbation [31]

$$\dot{\delta} = \frac{\delta v \omega \left( -2T_m \Gamma \omega^2 \left( \tilde{\alpha}(\omega) - \frac{vp}{D} \right) - 2 \left( \frac{k_s G_s + k_L G_L}{k_s + k_L} \right) \left( \tilde{\alpha}(\omega) - \frac{vp}{D} \right) + 2mG_C \left( \tilde{\alpha}(\omega) - \frac{v}{D} \right) \right)}{2 \left( \frac{k_s G_s - k_L G_L}{k_s + k_L} \right) \left( \tilde{\alpha}(\omega) - \frac{vp}{D} \right) + 2\omega m G_C} \quad (4.2)$$

In this equation,  $G_S$ ,  $G_L$ ,  $k_S$ , and  $k_L$  are the temperature gradients in the solid and the liquid, and the thermal conductivity of the solid and the liquid, respectively.  $T_m$  is the melting temperature of the interface,  $\Gamma$  is the ratio of the solid-liquid surface energy to the latent heat of fusion per unit volume,  $m$  is the liquidus slope of the dilute alloy,  $k = x_S/x_L$  is the partitioning coefficient, where  $x_S$  and  $x_L$  are the interface solute concentration in the solid and the liquid, respectively.  $\tilde{\alpha}$ ,  $G_C$ , and  $p$  are given by

$$\begin{aligned} \tilde{\alpha}(\omega) &= (v/2D) + \left( (v/2D)^2 + \omega^2 \right)^{1/2}, \\ G_C &= vx_s(k-1)/Dk, \quad p = 1 - k. \end{aligned} \quad (4.3)$$

According to Narayan [98], who investigated the stability of various dopants in Si, the dependence of the Ge partitioning coefficient  $k$  on the solidification velocity  $v$  should be incorporated into the Mullins-Sekerka stability criterion. This dependence is known as the solute trapping function. For Ge poor alloys it is given by [6]

$$k(v) = \frac{k_e + v/v_D}{1 + v/v_D}, \quad (4.4)$$

where  $k_e$  is the partitioning coefficient at a quasi equilibrium growth and  $v_D$  is the ‘‘diffusive speed’’ parameter.

Another correction applied for instability calculations of Sn in Si by Høglund et al. [102] is the dependence of the liquidus slope  $m$  on the solidification velocity  $v$ . This dependence is known as the kinetic liquidus slope function and it is given by [103]

$$m(v) = m_e \left( 1 + \frac{k_e - k(v)(1 - \ln(k(v)/k_e))}{1 - k_e} \right), \quad (4.5)$$

where  $m_e$  is the liquidus slope at a quasi equilibrium growth.

According to Eq. 4.2,  $\dot{\delta}$  was calculated numerically as a function of  $\omega$  for a wide range of solidification velocities. A stability-instability crossover occurs if a critical  $x_S^*$  exists for which  $\dot{\delta} = 0$  for some  $\omega^*$ . The parameters used to calculate the curves are summarized in Table 4.1 [98]. The value for the liquidus slope of  $m_e = -210$  K/(atom fraction) in the range of  $x < 0.3$  was estimated from the phase diagram of  $\text{Si}_{1-x}\text{Ge}_x$  alloys [104].

**Tab. 4.1** The table shows the values used to calculate the instability curves plotted in Fig. 4.2 and 4.3.

$G_S$ (K/m)	$G_L$ (K/m)	$k_S$ (J/msK)	$k_L$ (J/msK)	$T_M\Gamma$ (Km)	$k_e$	$D$ (cm <sup>2</sup> /Vs)	$v_D$ (m/s)
$6.57 \times 10^8$	$1.33 \times 10^6$	22	70	$1.3 \times 10^{-7}$	0.4	$2.5 \times 10^{-4}$	2

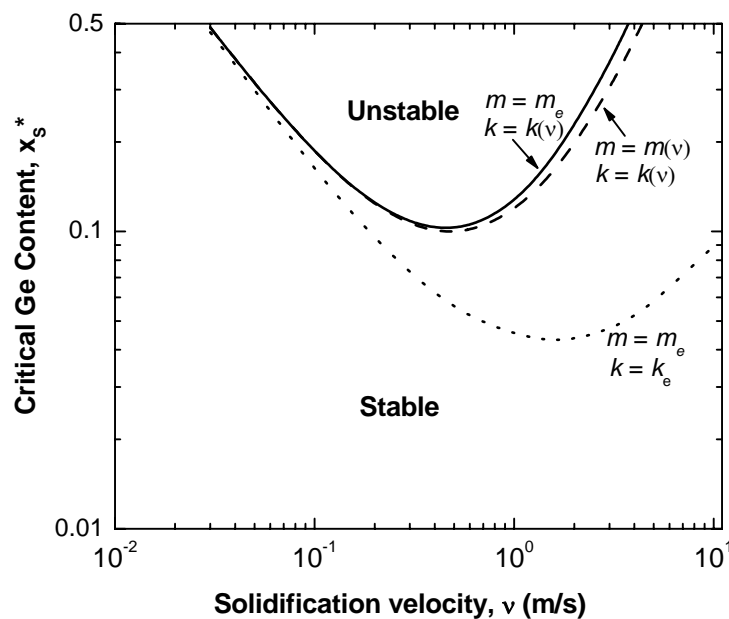


**Fig. 4.2** Comparison between different stability curve calculations for  $\text{Si}_{1-x}\text{Ge}_x$  with  $x < 0.5$ . The dotted line is the calculation according to the original model by Mullins and Sekerka [31] ( $m = m_e$ ,  $k = k_e$ ). The solid line takes into account the solute trapping correction according to Narayan [98] ( $m = m_e$ ,  $k = k(v)$ ). The dashed line is a calculation that takes into account solute trapping and kinetic liquidus slope corrections according to Høglund et al. [102] ( $m = m(v)$ ,  $k = k(v)$ ).

The dotted line in Fig. 4.2 shows the marginal stability curve derived from the original Mullins-Sekerka stability criterion, the solid line takes into account the solute trapping correction, and the dashed line takes into account both solute trapping and kinetic liquidus corrections. The comparison between the curves show that for SiGe alloys the effect of solute trapping strongly influences the stability curve whereas the kinetic liquidus slope correction is small and can be neglected. The theoretical instability calculations reveal that for samples with a Ge content larger than 12 % and for solidification velocities between 0.02 and 3 m/s, the solidification is expected to enter an instability growth regime.

Fig. 4.3 shows the theoretical instability curve (solid line in Fig. 4.2) in comparison to experimentally determined solidification velocities of SiGe samples on quartz substrates that exhibit self organization (full circles). Note that  $x$  in Fig. 4.3 represents the critical Ge content  $x_S^*$  for the theoretical curve. The comparison between theory and experiment shows a good agreement since all the experimental data fit well in the instability tongue. Moreover, this comparison shows that the solidification of SiGe thin films on quartz occurs close to the marginal line on the high velocity side. This proximity suggests that the structure suppression caused by utilizing molybdenum coated glass or stainless steel substrates (see Fig. 3.5) is due

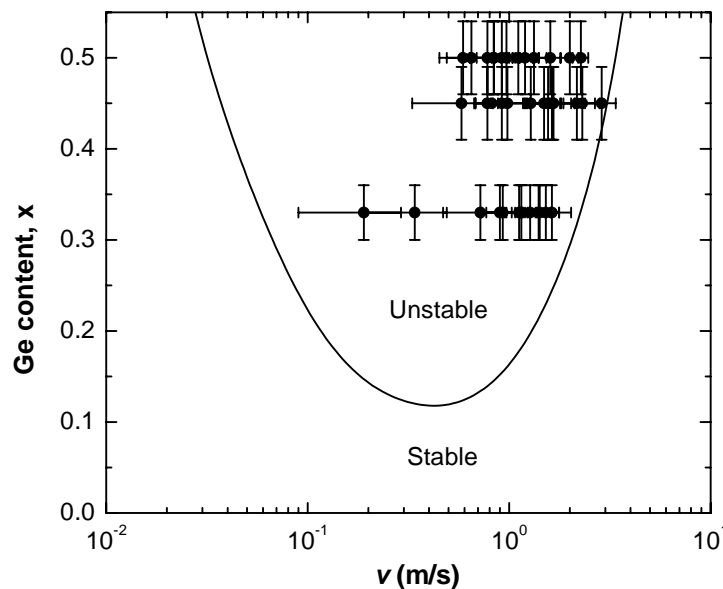


**Fig. 4.3** Germanium content  $x$  as a function of the solidification velocity  $v$ . The solid line represents a theoretical marginal stability curve calculated on the basis of the Mullins-Sekerka perturbation theory. Above the curve the solidification solid-liquid interface is expected to be unstable during solidification. The full circles represent measured data from laser-crystallized poly-SiGe thin films on glass that exhibit the self-organization phenomenon.

to an increase in the solidification velocity. Using such substrates with a higher thermal conductivity is expected to enhance the heat flow rate out of the SiGe layer during solidification and therefore, to cause an increase in the solidification velocity. Since the thermal conductivity of SiO<sub>2</sub> is lower than that of SiGe [38, 105, 106], the thermal conductivity of the substrate is expected to be the main limiting parameter for the solidification velocity. In agreement with this interpretation, solidification velocities of SiGe thin films on sapphire substrates were reported to reach  $\approx 4$  m/s [6], which is significantly higher than for SiGe on insulating substrates ( $\approx 1$  m/s).

The periodicity length of the structure that evolves from the instability can be estimated as  $d = 2\pi/\omega^*$ . This is a good approximation for a weak instability of the solid-liquid interface, where the amplitude of the fastest growing perturbation, in the vicinity of  $\omega^*$ , is still growing at a significantly slow rate. Fig. 4.4 shows the theoretical periodicity length for a weak instability compared to the experimental results of laser-crystallized poly-Si<sub>0.55</sub>Ge<sub>0.45</sub> films. The discrepancy in  $d$  between the experimental and theoretical results varies between a factor of 4 and 9. Moreover, the experimental data seem to show a tendency to a higher  $d$  with increasing  $v$ , which is contrary to the theoretical trend. These discrepancies indicate that the weak instability conditions used for the calculations are not fulfilled. Apparently, the structure undergoes rapid, nonlinear changes once the instability is triggered.

Another indication of the nonlinear nature of the self organization phenomenon is the large periodicity length observed compared to the diffusion length expected by a linear approach. The latter can be estimated using the expression  $(2Dt)^{0.5}$ . Typical parameters of  $t = 100$  ns and  $D = 2.5 \times 10^{-4}$  cm<sup>2</sup>/Vs yield a diffusion length of only 70 nm. This suggests that according to a linear model where the periodicity of the structure is determined by the diffusion field, the maximum periodicity length possible would be about 140 nm. This value, however, is considerably smaller than those presented in Fig. 4.4.

It should be noted that according to Eq. 4.1 the periodicity length  $d$  obtained from the excitation of capillary waves is in the range of 2  $\mu$ m for our experimental conditions. This gives rise to the idea that a coupling between the instability and the capillary waves on the surface may be contributing to the enhanced periodicity length observed.

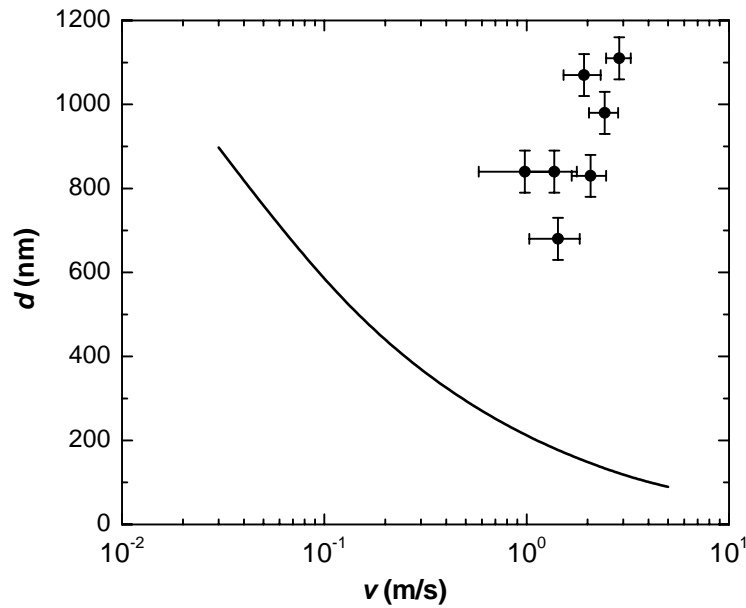


**Fig. 4.4** Periodicity length  $d$  of the self organized structure as function of the solidification velocity  $v$ . The solid line was derived from theory based on the Mullins-Sekerka instability analysis according to  $d = 2\pi/\omega^*$  (see text). The full circles depict experimental data that were obtained from poly-Si<sub>0.55</sub>Ge<sub>0.45</sub> samples crystallized with a single laser pulse.

In conclusion, the theoretical analysis presented in this section supports the pattern formation mechanism of an instability on the solid-liquid interface during solidification. The experimentally derived solidification velocities of SiGe films on glass fit well in the marginal instability tongue. Moreover, the suppression of the phenomenon, when using stainless steel or molybdenum coated glass substrates, can be explained as the result of a transition from instability to stability. The observation of an instability in SiGe alloys is unexpected since the equilibrium partitioning of Ge across the solid-liquid interface is much weaker than for In, Ga, Sb, and Sn [6, 7]. The SiGe interface is expected to be much more stable than in the case of other Si based alloys. Studies done on laser annealing of SiGe alloys with a Ge content of up to 20 at.% [6, 7, 107] have not observed lateral segregation or self organization phenomena.

In addition, the results are also surprising because of the fact that they were obtained using thin films on glass substrates. The studies mentioned above by Hoglund et al. [102] and Narayan [98] that show structure formation due to an interface instability were performed on single crystals. In that case, the condition of an initially planar solid-liquid interface, required

for the instability theory, is well satisfied. For thin films on foreign substrates, the nucleation and crystal growth are more complex [28] such a condition cannot be assumed, a priori, to be fulfilled. Nevertheless, the findings presented here are consistent with the existence of an initially planar interface and suggest that the instability mechanism overrides incoherent nucleation and crystal growth influences.

## 4.2 Defects and electrical transport

### 4.2.1 Transport along grain boundaries

In this section, the mechanisms dominating the electrical transport properties of laser-crystallized polycrystalline silicon-germanium thin films are discussed. The conductivity results presented in Sec. 3.2.2 showed that for most samples with a high Ge content, a nearly temperature-independent (metallic-like) conductivity in the range 20 – 100 K appears. These samples exhibited an atypical ESR signal that was identified as an electric dipole spin resonance (EDSR). The angle dependence of the EDSR signal suggests that the metallic-like conductivity is caused by charge carriers that are restricted to the grain boundaries (see Figs. 3.16 and 3.18).

The possibility that the metallic-like conductivity originates from the surface of the layer as, for example, has been reported for diamond [108], is inconsistent with the angle dependence of the EDSR signal. In the case of surface conductance, a maximum in the EDSR signal would have been observed for an angle of  $\varphi = 90^\circ$  between  $\mathbf{B}_0$  and the surface of the sample. Instead, the EDSR signal exhibits for  $\varphi = 90^\circ$  a minimum (see Fig. 3.16). Moreover, the change in conductivity upon plasma hydrogenation would have been abrupt (after a short exposure). The slow change in conductivity as a function of the hydrogenation time seen in Fig. 3.20 is consistent with the diffusion time needed for hydrogen to penetrate into the layer.

There have been many investigations showing that grain boundary conductance in polycrystalline and bicrystalline silicon [32], germanium [109, 110, 111, 112], and III-V semiconductors such as indium antimonide (InSb) [113] can dominate the electrical activity of the material. However, it is still a matter of controversy whether the electrical activity

originates from intrinsic defects like dangling or distorted bonds or from impurities trapped at the grain boundary. Impurities that are often unintentionally incorporated are copper (Cu), nickel (Ni), iron (Fe), and oxygen (O). For Ge, most of the studies point to the intrinsic source, namely dangling bonds [109, 110, 111], whereas for Si, the role of dangling bonds is less clear and the reports tend to assign the electrical activity to impurities [32, 33, 34]. It should be noted that the phrase electrical activity mostly stands here for the conductance of charge carriers, unless it appears in the context of charge recombination.

Since in our case the metallic-like conductivity was mostly observed for Ge-rich polycrystalline SiGe alloys, it is most likely that the electrical activity of the grain boundary is caused by dangling bonds. This is further supported by the different conductivity behavior observed for poly-SiGe films that originate from the same amorphous starting material but were crystallized with different procedures. For example, a poly-Ge film that was crystallized with a single laser pulse exhibited metallic conductivity, whereas a thermally crystallized poly-Ge film exhibited thermally activated behavior of the electrical dark-conductivity. Both films were annealed in the same furnace under similar conditions for several hours for the purpose of crystallization or hydrogen removal prior to the laser irradiation. Therefore, the only difference in the processing of the films was a short laser treatment on the time scale of  $t \approx 100$  ns, carried out under vacuum conditions. It seems unlikely that such a short treatment would have resulted in significant incorporation of impurities into the melt or segregation of pre-existing impurities to the grain boundaries during solidification. A rough estimation of the diffusion length on this time scale for an iron impurity with a diffusion coefficient of  $D = 7 \times 10^{-5}$  in Si-Fe liquid [114] yields a value of  $(2Dt)^{0.5} \approx 40$  nm. Therefore, the dangling-bond properties provide a more reasonable explanation for the different conductivity behavior observed in this case. Moreover, this explanation is consistent with the ESR results presented in Fig. 3.14, showing that the dangling-bond concentration of laser-crystallized poly-SiGe films is higher than of thermal-crystallized films. It should also be noted that the initially amorphous SiGe films were device-grade layers commonly used for tandem solar cells. Therefore they are not expected to contain high amounts of impurities.

In order to understand how electrical transport might occur along grain boundaries via dangling bonds, some properties of these defects are outlined here. Fig. 4.5 shows a schematic illustration of the band structure across and along a grain boundary. The band bending across the grain boundary is due to accumulated charge in this region. The Fermi level  $E_F$  is assumed

to be somewhere in the middle of the band-gap because the layers were undoped and the dangling-bond defects tend to pin  $E_F$  at mid gap. Dangling bonds can be found in non-occupied ( $D^+$ ), singly-occupied ( $D^0$ ), and doubly-occupied ( $D^-$ ) charge states. Adding a second electron to a singly occupied localized dangling-bond (DB) defect level requires extra energy due to the Coulomb repulsion between the two electrons. Therefore, the density of states  $N(E)$  diagram shown in Fig. 4.5 may be presented, in a simplified way, by two peaks corresponding to singly occupied  $D^+/D^0$  and doubly occupied  $D^0/D^-$  transition states that are separated by the correlation energy  $U$ . The state  $D^+/D^0$  is defined as unoccupied for a positively-charged dangling bond ( $D^+$ ) and occupied for a neutrally-charged dangling bond ( $D^0$ ), whereas  $D^0/D^-$  is defined as unoccupied for  $D^0$  and occupied for  $D^-$ . It should be mentioned that representing the dangling-bond states  $D^+/D^0$  and  $D^0/D^-$  in a single-electron density of states, though in some ways useful, imposes certain limitations. For example, it is not possible to shift the Fermi level in such a representation without changing the density of

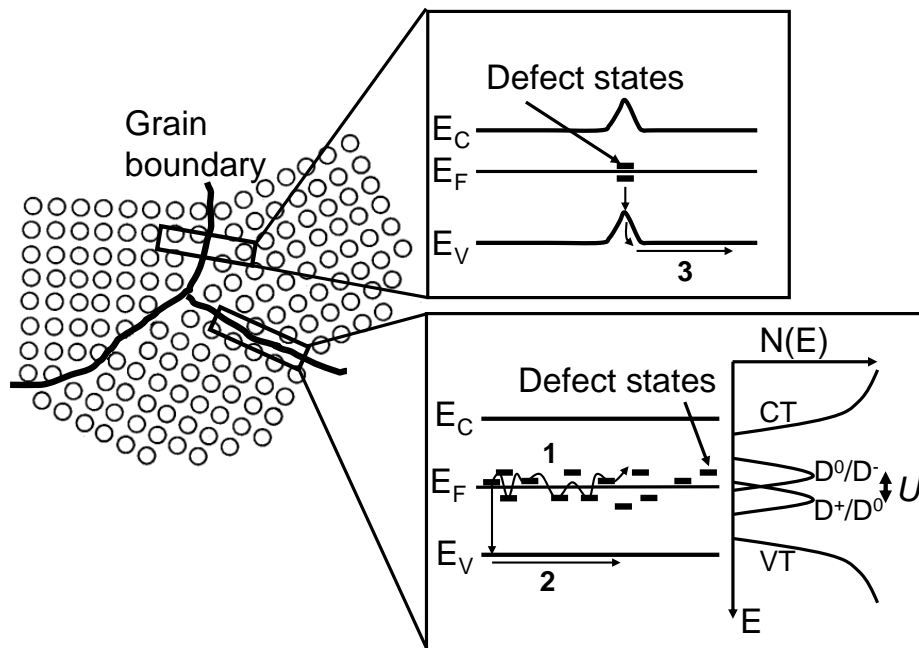


**Fig. 4.5** Schematic illustration of the band structure across and along a grain boundary.  $E_C$ ,  $E_V$ , and  $E_F$  represent the conduction band minimum, the valence band maximum, and the Fermi energy, respectively. The idealized density of states  $N(E)$  at the grain boundary shows two dangling-bond peaks  $D^+/D^0$  and  $D^0/D^-$  that are separated by the correlation energy  $U$ . CT and VT represent the conduction and valence tails. Possible transport paths are indicated by the arrows 1, 2, and 3.

states distribution. In addition, a well known property of dangling bonds in a-Si:H is that they do not have fixed energy levels and defect states may be created or destroyed from a pool of states in accordance with the preparation conditions [115, 116]. Often the DB system organizes itself in such a way that  $E_F$  is positioned in a local minimum of the density of states.

The way localized dangling-bond states can become delocalized and cause metallic-like conductance is illustrated in Fig 4.6 according to the Mott-Hubbard metal-insulator transition [117, 118]. The  $D^+/D^0$  and  $D^0/D^-$  states are associated with the lower and upper Hubbard band, respectively. As the mean distance between dangling bonds  $r$  is reduced, an overlap between the electron wave functions occurs and a band is formed. This is analogous to the way discrete atomic levels join together and form bands in solids according to the tight binding model [119]. The formation of bands, however, is not a sufficient condition for the insulator-metal transition since, if the lower Hubbard band is fully occupied and the upper one is empty, no transport can occur. The metal-insulator transition takes place when the distance between defects  $r$  becomes sufficiently small to assure an overlap between the lower

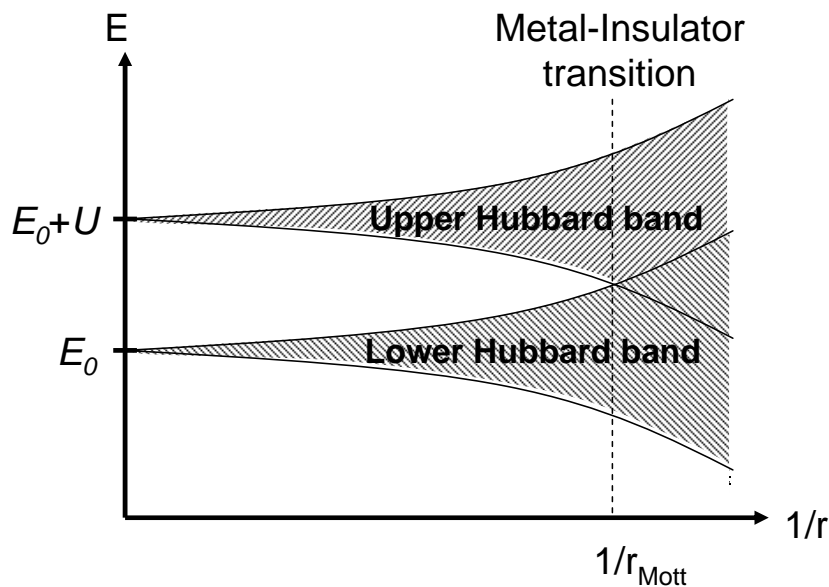


**Fig. 4.6** Formation of the lower and upper Hubbard bands from localized singly and doubly occupied defect states as the distance between defects  $r$  is reduced. The localized singly and doubly occupied states are separated by the correlation energy  $U$ . The Mott-Hubbard metal-insulator transition takes place at a critical distance between defects  $r_{\text{Mott}}$  where the Hubbard bands overlap.

and upper Hubbard band. The critical defect concentration  $N_{\text{Mott}} \approx 1/r_{\text{Mott}}^3$  for the transition for impurities in several semiconductors follows [118]

$$N_{\text{Mott}}^{1/3} \cdot \underbrace{\left( \frac{4\pi\epsilon_0\epsilon_r\hbar^2}{m^*e^2} \right)}_{a_B} \approx 0.26, \quad (4.6)$$

where  $\epsilon_r$  is the dielectric constant,  $m^*$  the effective mass, and  $a_B$  is the effective Bohr radius of the defect center. The critical defect concentration in Si and Ge was estimated according to Eq. 4.6 to be  $N_{\text{Mott}} \approx 4 \cdot 10^{18} \text{ cm}^{-3}$  and  $N_{\text{Mott}} \approx 2 \cdot 10^{17} \text{ cm}^{-3}$ , respectively [120]. The smaller  $N_{\text{Mott}}$  value obtained for Ge is due to its higher dielectric constant [38] and the smaller effective mass that can be associated with a DB defect in this material.

Indications that an additional mechanism to the one discussed above should be taken into account for metal-insulator transitions were found by investigations performed on compensated semiconductors such as Si:P,B [121] and Ge:Sb,Ga [122]. Experiments on such semiconductors that have a fixed compensation ratio of minority to majority impurities but

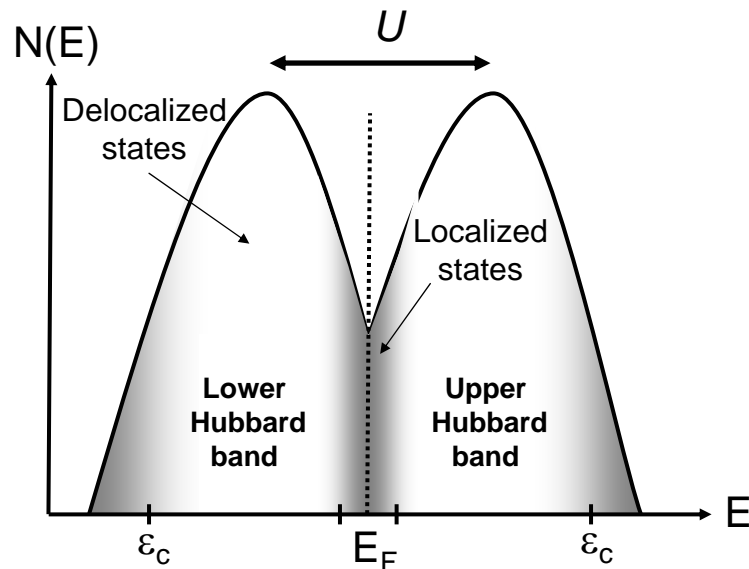


**Fig. 4.7** Schematic density of states  $N(E)$  distribution of the Hubbard bands showing the influence of the Anderson localization. Due to the disorder that is introduced into this system localized states appear at the sides of the Hubbard bands. The Fermi level resides in a region of localized states although the Hubbard bands overlap.  $\epsilon_c$  represents the mobility edge.

different amounts of total impurities, offer an elegant way to investigate the influence of disorder. The results of these experiments show that for a small compensation ratio (little disorder) the critical concentration for the metal-insulator transition  $N_C$  agrees well with the results shown above for  $N_{\text{Mott}}$  in Si and Ge according to Eq. 4.6. However, as the compensation ratio increases (more disorder)  $N_C$  can become significantly larger than  $N_{\text{Mott}}$ . This effect is caused by the Anderson localization [123] that describes the localization of delocalized states by disorder introduced into the system. Fig. 4.7 shows how the Anderson localization causes each of the Hubbard bands to contain regions, in the density of states diagram, where localized states appear. As a result, the Fermi level in the figure is positioned at a region of localized states and the system exhibits an insulator character although the Hubbard bands overlap. Due to the Anderson localization the metal-insulator transition occurs for  $N_C > N_{\text{Mott}}$  first when the mobility edge  $\epsilon_c$  of the upper and lower Hubbard band coincide.

The Mott-Hubbard metal-insulator transition and the Anderson localization are both possible models to explain the decrease in conductivity upon plasma hydrogenation presented in Fig. 3.20. A decrease in the dangling-bond concentration due to the passivation of defects by hydrogen might cause the defect concentration to decrease below  $N_C$  and induce a Mott-Hubbard transition. On the other hand, the incorporation of hydrogen might enhance the disorder at the grain boundaries and suppress their electrical activity due to the Anderson localization. Another possibility related to the Anderson localization is that the incorporation of hydrogen might cause the Fermi level to shift from a region of delocalized states over a mobility edge to a region of localized states. The more plausible of these explanations, however, is the passivation of dangling bonds because the ESR DB signal and the sub-band-gap optical absorption decrease upon hydrogenation.

The sub-band-gap absorption peak observed for laser-crystallized poly-Si<sub>0.5</sub>Ge<sub>0.5</sub> might provide an insight into the dangling-bond properties and the influence of hydrogen. It is unlikely that this absorption peak can be associated with optical transitions between valance and conduction band-tail states due to the following arguments. Firstly, the optical transition energy that corresponds to the absorption peak can become as small as 0.21 eV below the optical band-gap energy. The optical band-gap is believed to be determined by transitions from valance band-tail states to delocalized conduction states or delocalized valance band states to conduction band-tail states [89]. Therefore, a significant amount of tail states needs to exist 0.21 eV above the valance or below the conduction band to explain the absorption

peak. This, however, is not plausible if one considers that the commonly observed width of the exponential tail, known as the Urbach energy, is in the range of 50-120 meV for a-Si:H [124], a-SiGe:H [125], and poly-Si [126]. Secondly, there is little chance of finding localized valance and conduction tail states in the same region of space and therefore optical transitions between such states are less probable than transitions that involve delocalized states [89].

A possible origin of the sub-band-gap absorption peak is the optical transition between the dangling-bond  $D^+/D^0$  states and the delocalized conduction states. Such an interpretation suggests that the dangling-bond states should be positioned at the lower half of the band-gap. This position is consistent with theoretical [127] and experimental [128] studies, which assign lower energies to dangling-bond states in Ge compared to Si. Fig. 4.8 shows a schematic diagram of the density of states before and after a H-treatment, as follows from associating the sub-band-gap absorption peak to a  $D^+/D^0 \rightarrow E_C$  transition (hollow arrow). The values depicted in the figure are from poly-Si<sub>0.5</sub>Ge<sub>0.5</sub> samples crystallized with a single laser pulse. The reduction in the sub-band-gap absorption peak intensity upon hydrogenation (see Fig. 3.26) is caused, according to this model, by the decrease in the dangling-bond concentration.

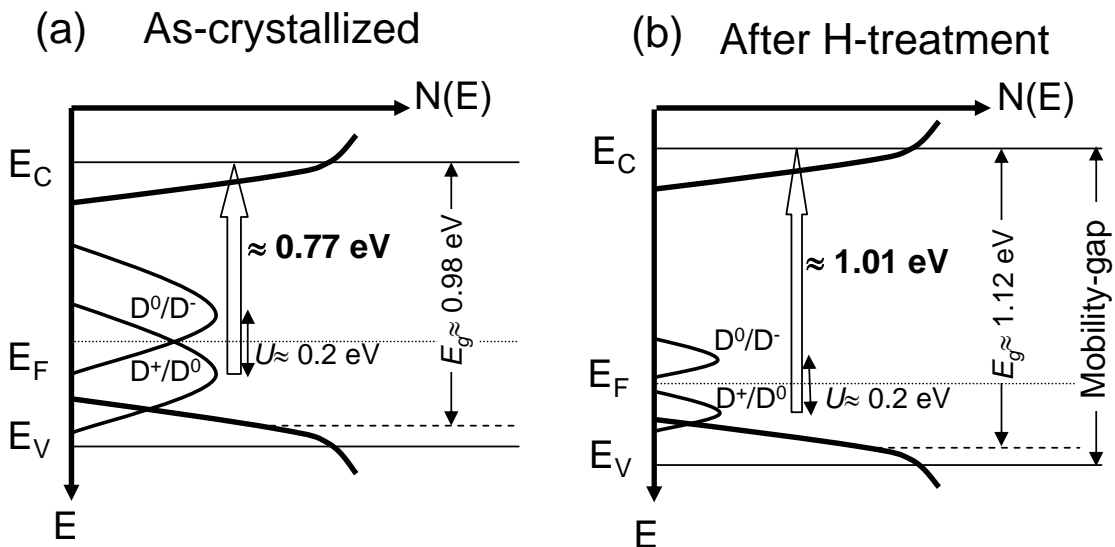


**Fig. 4.8** Schematic density of states  $N(E)$  distribution for poly-Si<sub>0.5</sub>Ge<sub>0.5</sub> crystallized with a single laser pulse. (a) represents the as-crystallized sample that exhibits metallic-like conductivity, whereas (b) represents the H-treated sample that exhibits insulator-like conductivity. The shape of  $N(E)$  and the values indicated were estimated from the optical absorption results. The correlation energy value  $U \approx 0.2$  was extrapolated from the work of Stutzmann et al. [129]. The hollow arrow represents the optical transition assigned to the sub-band-gap absorption peak in Fig. 3.26.

The observation that metallic-like conductivity mostly occurs for SiGe specimens with a high Ge content can have two explanations. The first originates directly from the larger effective Bohr radius of a DB defect in Ge ( $\approx 4.4$  nm) in comparison to Si ( $\approx 1.6$  nm) [120]. This difference can also be expressed in terms of a smaller correlation energy for Ge ( $\approx 0.1$  eV) compared to Si ( $\approx 0.3$  eV) [129] since it depends inversely on the distance between the two electrons on the same defect. As a result, the metal-insulator transition occurs according to Eq. 4.6 at a lower defect concentration for Ge. The second explanation suggested by Mataré [130] is that Si tends to form grain boundaries with lower interfacial energy, e.g. low-angle twin boundaries of the type  $\Sigma 3$ , compared to Ge during solidification. Such grain boundaries are expected to have a lower concentration of dangling bonds. It should be mentioned, however, that this explanation is not supported by the ESR data presented in Fig. 3.14.

According to the metal-insulator transition models considered above, the grain boundaries become electrically inactive when the defect concentration in this region decreases below  $N_C$ . In such a case, the conduction should be dominated by thermally excited carriers at the valence band. However, close inspection of the conductivity behavior suggests that near the metal-insulator transition on the insulator side, conductance might still prevail along dangling bonds by hopping. According to this transport mechanism the conductivity is given by [131]

$$\sigma_D(T) = \sigma_0 \cdot \exp\left(\frac{T_0}{T}\right)^{1/4}, \quad (4.7)$$

where  $\sigma_0$  and  $T_0$  are constants. The data presented in Fig 3.20 of laser-crystallized poly-Si<sub>0.5</sub>Ge<sub>0.5</sub> is replotted in Fig. 4.9 according to Eq. 4.7 as  $\ln\sigma_D$  against  $1/T^{1/4}$ . The straight line that appears supports the interpretation that hopping conductivity takes place when the defect concentration decreases below  $N_C$ .

Despite the fact that the fit to the data in Fig. 4.9 can be extended over the entire temperature range, it is expected that at high temperatures ( $T > 100$  K) the electrical transport will occur primarily at the valence band. At this temperature range the data can also be fitted to a straight line in a  $\ln\sigma_D$  against  $1/T$  presentation type (see Fig. 3.20). Therefore, the overall conductance through the sample is a combination of transport along path 1, 2, and 3 in Fig. 4.5. At low temperatures, conductance along path 1 is dominant and might have a metallic or

hopping character depending on the DB defect concentration and Ge content. At higher temperatures conductance along path 2, and 3 becomes more significant. Differentiating between path 2 and 3 is not possible according to the experimental data because the barrier introduced by the band bending on the grain boundary is smaller than the activation energy  $E_F - E_V$ .

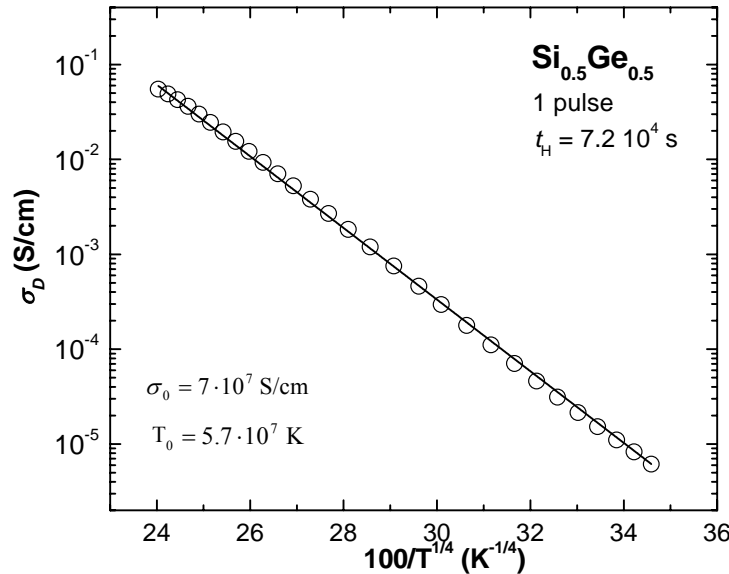


**Fig. 4.9** Electrical conductivity  $\sigma_D$  as function of  $1/T^{1/4}$  for a laser-crystallized poly-Si<sub>0.5</sub>Ge<sub>0.5</sub> film that was exposed to hydrogen plasma treatment for  $t_H = 72 \times 10^3$  s. The fit to the data according to Eq. 4.7 yields the indicated  $\sigma_0$  and  $T_0$  values.

In summary, the unexpected high metallic-like conductivity observed for Ge-rich laser-crystallized poly-SiGe samples is believed to occur due to conductance along dangling-bond defects at the grain boundaries. This kind of conductivity occurs mostly for Ge-rich specimens probably due to the more extended electron wave function of a dangling-bond defect in Ge compared to Si. The suppression of the electrical activity of the grain boundaries by a hydrogen plasma treatment is attributed to the reduction of the dangling-bond defect concentration below a critical metal-insulator transition value.

## 4.2.2 Hydrogen-induced defects

The discussion in the previous section concluded that the incorporation of hydrogen results in the passivation of dangling-bond defects at the grain boundaries. This beneficial process is commonly used to obtain device-grade material. However, this is probably not the only effect of H incorporation. The decrease in photoconductivity observed upon hydrogenation (see Fig. 3.24) suggests that H also generates some sort of defects. In this section a possible formation mechanism for these defects is suggested.

Incorporating hydrogen into a host material can result in various forms of damage and defect formation. The implantation of high energy  $H^+$  ions into Si [132] and Ge [133] has been reported to induce vacancies that grow into micro-voids and cracks. The formation mechanism behind this effect was suggested by Van de Walle et al. [134] to be hydrogen-assisted ejection of a threefold- or twofold coordinated Si atom, which is an enlargement of a preexisting defect. Such implantation damage, however, is unexpected for H plasma treatments using an optically isolated remote plasma [135, 136] and therefore it is assumed that in our case the formation of vacancy-hydrogen defect structures is not significant.

Since the concentration of dangling bonds (less than  $10^{19} \text{ cm}^{-3}$ ) is much smaller than the concentration of hydrogen (typically in the range of  $\approx 10^{21} \text{ cm}^{-3}$ ), the majority of hydrogen is not bonded to DB defects in the SiGe-network. Possible bonding configurations for hydrogen, which are often considered in the literature for Si, are shown in Fig. 4.10. A single H atom accommodated at the bond centered (BC) site and the interstitial tetrahedral ( $T_d$ ) site is shown in Fig. 4.10(a) and (b), respectively. Hydrogen at the BC site has a charge state  $q = +1$  and at the  $T_d$  site a charge state  $q = -1$ . In both cases, hydrogen can introduce states in the band-gap [137] as discussed below. It has been argued that hydrogen tends to pair in the Si-network due to a negative correlation energy for hydrogen atoms [138]. Two possible pairing configurations are the interstitial molecular  $H_2$  (Fig. 4.10(c)) and the  $H_2^*$  complex (Fig. 4.10(d)). Since some evidence has been raised against the formation of molecular  $H_2$  in a-Si:H [139], Johnson et al. has suggested that the  $H_2^*$  might comprise the building block for the majority of H in Si.

The  $H_2^*$  structure can be extended to form an aggregated  $H_2^*$  complex, which is known as a platelet (Fig. 4.10(e)). By stacking up  $H_2^*$  complexes strain can be reduced by as much as

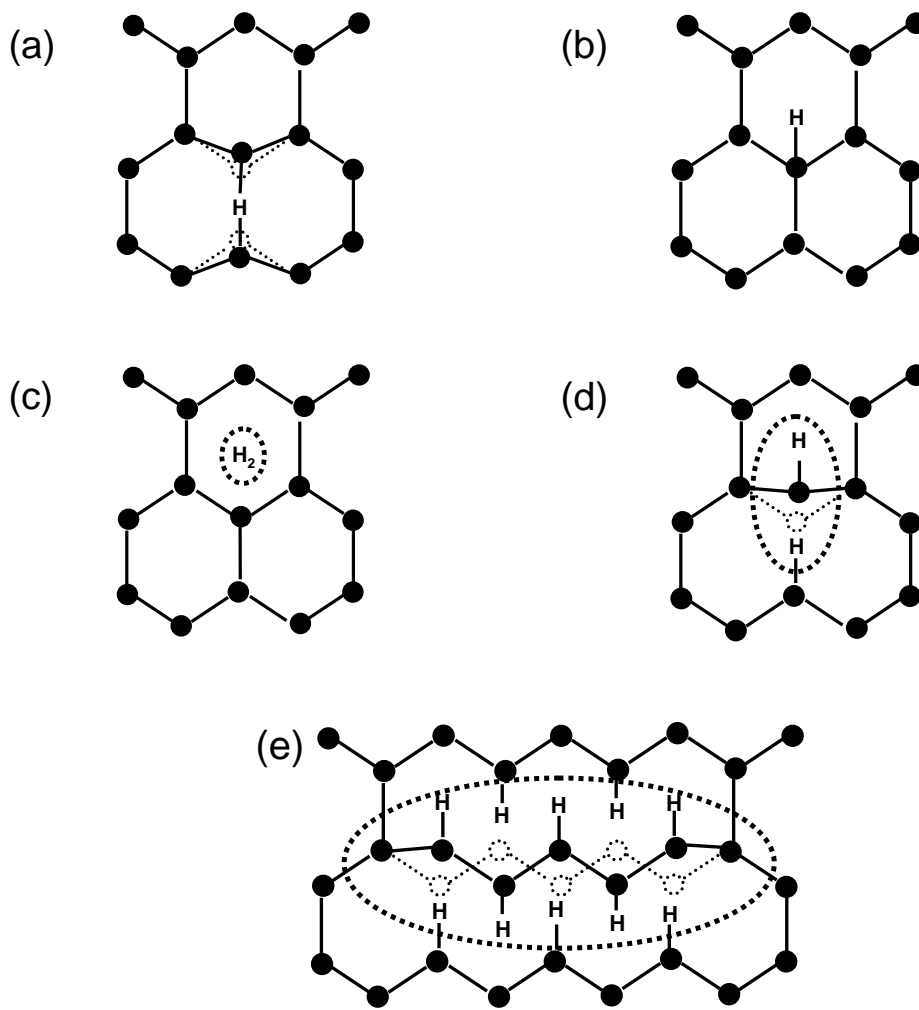


**Fig. 4.10** Possible hydrogen configurations in elemental semiconductors: (a) H at a bond-centered site, (b) H at a  $T_d$  site, (c) interstitial molecular  $H_2$ , (d) bond-centered-antibonding pair ( $H_2^*$ ), and (e) aggregated  $H_2^*$  complex known as platelet [140].

0.4 eV per hydrogen pair in silicon [139]. Platelet structures were originally observed in n-type crystalline Si by transmission electron microscopy (TEM) [36]. These structures are restricted to within  $\approx 0.1 \mu\text{m}$  from the exposed surface and are predominantly oriented along the  $\{111\}$  crystallographic planes. They mostly appear at regions of high H concentrations ( $> 10^{17} \text{ cm}^{-3}$ ) and for hydrogenation temperatures below  $300^\circ\text{C}$ . Under favorable conditions for platelet formation it was possible to observe structures as long as  $150 \text{ nm}$  [141]. Moreover, Johnson et al. were able to show that platelets introduce electrically active states into the band-gap [36].

In-situ conductivity measurements performed by Nickel et al. [142] on polycrystalline Si during remote plasma hydrogenation show an initial increase in conductivity that goes through a maximum and decreases at longer times of about  $10^4$  s until an equilibrium is reached. This behavior was attributed to a trade-off between grain boundary defect passivation and the formation of new defects that are probably platelets. For short times the former process dominates whereas for longer times, the latter process becomes more pronounced until a steady state is reached. The specimens exposed to prolonged hydrogenation also exhibited a change from n- to p-type conductivity, which was attributed to hydrogen-induced acceptor-like defect states in the band-gap.

A more recent study [37] performed on laser-crystallized poly-Si also suggests that once hydrogen becomes mobile in this material an equilibration between DB defect passivation and platelet formation can take place. In this study, the DB ESR signal decreased upon annealing, pointing to the passivation of defects, while at the same time the H density of states derived from H effusion measurements formed a remarkable peak at  $E \approx -3$  eV, which can be attributed to the formation of platelets. Therefore, it seems plausible that the post-hydrogenation of laser-crystallized poly-SiGe carried out in this study may have resulted in some equilibrium between DB defect passivation and platelet formation. The electrically active states introduced into the band gap by platelets are expected to serve as recombination centers and eventually, for a non-optimized H treatment, reduce the photoconductivity.

In order to elucidate how platelets may nucleate in the host material it is useful to look at the properties of single isolated interstitial H atoms. Fig. 4.11 shows the formation energy for  $H^q$  ( $q = +1, 0, \text{ or } -1$ ) as a function of the Fermi level for Si [143] and for Ge [127] calculated on the basis of density-functional theory (DFT) in the local density approximation (LDA). The formation energy is the energy needed to incorporate  $H^q$  in the host material. The transition level  $\varepsilon(q+1/q)$  is defined as the Fermi level position for which the formation energies of these charge states are equal. For Si,  $\varepsilon(+/-)$  is in the upper half of the band-gap, indicating that for n-type Si the stable charge state is  $H^-$  whereas for p-type Si it is  $H^+$ . This demonstrates the amphoteric character of hydrogen and its tendency to counteract the conductivity caused by extrinsic dopants. The transition levels  $\varepsilon(+/0)$  and  $\varepsilon(0/-)$  indicate the donor and acceptor states introduced into the band-gap by  $H^+$  and  $H^-$ , respectively. Since  $H^0$  is never the lowest energy state, the level  $\varepsilon(+/0)$  lies above  $\varepsilon(0/-)$ , which is characteristic for a

negative  $U$  system. The positions of these transition levels were also determined experimentally by Johnson et al. [137], who found good agreement with the theory.

In Ge, on the contrary, Fig. 4.11(b) shows that  $\epsilon(+/-)$  is in the valance band. This result indicates that hydrogen in Ge tends to reside in the  $T_d$  site in the negatively charged state, which is also consistent with calculations performed by Estreicher et al. [144]. It should be mentioned, however, that one deficiency of the DFT-LDA calculations is that they underestimate the band-gap energy, which might eventually cause large errors in determining the position of  $\epsilon(+/-)$ . Nevertheless, the qualitative behavior expected for SiGe alloys is a shift of  $\epsilon(+/-)$  towards the valance band with increasing Ge content.

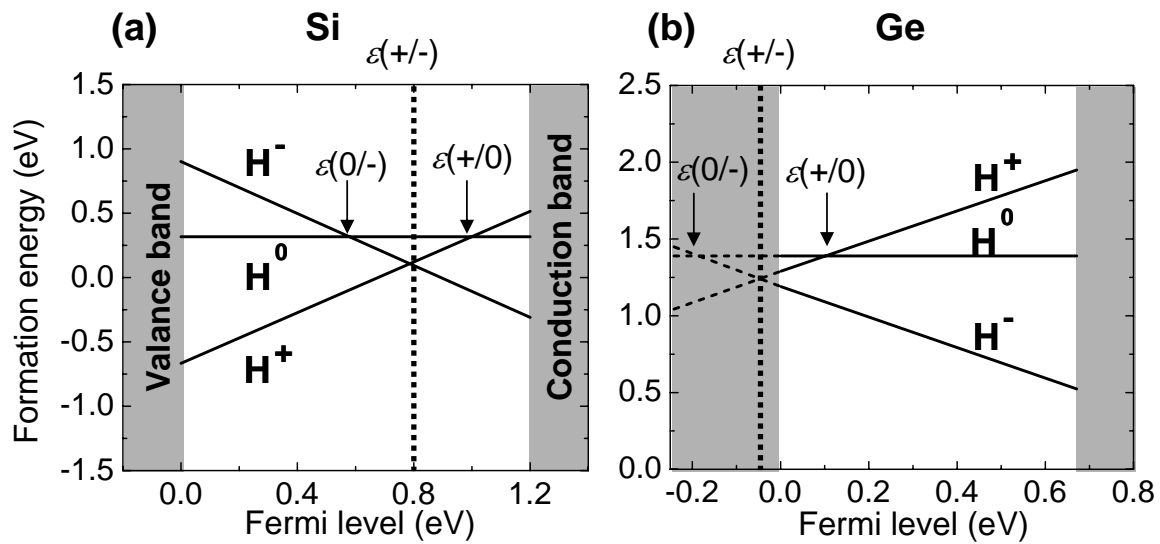


**Fig. 4.11** Formation energy of  $H^q$  in the charge state  $q = -1, 0$ , or  $+1$  as function of the Fermi level derived from DFT-LDA calculations. (a) represents results reported for c-Si [143] and (b) represents results reported for c-Ge [127]. The transition level  $\epsilon(q+1/q)$  is defined in the text.

As mentioned above, the  $H_2^*$  complex might serve as a nucleation site for additional hydrogen, causing the formation of a platelet. Since the  $H_2^*$  complex consists of a  $H^+$  at the BC and  $H^-$  at the  $T_d$  site (see Fig. 4.10(d)), both positively and negatively charged H atoms are required for the formation of this complex. This condition is best fulfilled when the Fermi level is close to the  $\epsilon(+/-)$  transition level. As pointed out by Nickel et al. [35], this condition for  $H_2^*$  formation is satisfied at a critical distance from the sample surface or the grain boundary due to the band bending at this region. Fig. 4.12 illustrates this idea; at the grain boundary where  $E_F < \epsilon(+/-)$ , hydrogen has a positive charge state whereas at the interior of the grain where  $E_F > \epsilon(+/-)$ , hydrogen has a negative charge state. At the location where  $E_F$  and  $\epsilon(+/-)$  cross, both  $H^+$  and  $H^-$  species exist and the  $H_2^*$  complex can form.



## 5 Summary

In this thesis, structural, electrical, and optical properties of laser-crystallized polycrystalline  $\text{Si}_{1-x}\text{Ge}_x$  thin films with  $0 < x < 1$  were investigated. The most important results and conclusions are summarized below:

- Laser crystallization of amorphous  $\text{Si}_{1-x}\text{Ge}_x$  thin films with  $0.3 < x < 0.7$  can result in a self-organized pattern of hillocks or ripples on the surface of the film, which is directly coupled to a periodic compositional variation. The elevated areas of the hillocks and ripples are enriched with Ge whereas the lowered areas are depleted of Ge.
- Amorphous SiGe samples that are exposed to a single laser pulse exhibit a ripple structure that evolves into a hillock structure when the samples are irradiated with additional laser pulses. The periodicity length of the structure after a single laser pulse is in the range of 0.3 to 1.1  $\mu\text{m}$ , depending on Ge content, layer thickness, and laser fluence and grows rapidly with increasing number of laser pulses. Moreover, the periodicity length exhibited no correlation with the grain size in these layers, which was typically 0.1  $\mu\text{m}$ .
- It is maintained that the main mechanism behind the structure formation is an instability of the propagating solid-liquid interface during solidification. Calculations made according to the Mullins-Sekerka instability theory for  $\text{Si}_{1-x}\text{Ge}_x$  with  $x < 0.5$  reveal that in the solidification velocity range of 0.02 to 3 m/s, the system is expected to be unstable for sufficient amounts of Ge in the alloy. This result is in good agreement with solidification velocities that were experimentally determined in this study for SiGe films on glass from transient conductivity measurements. Moreover, the suppression of the self organization for SiGe films on stainless steel and molybdenum-coated glass substrates is in accordance with this model, since these substrates have a higher thermal conductivity that causes the solidification velocity to increase.
- The study of defects with electron spin resonance showed that laser-crystallized poly- $\text{Si}_{1-x}\text{Ge}_x$  thin films with  $0 < x < 0.84$  have a dangling-bond concentration of about  $N_s = 4 \times 10^{18} \text{ cm}^{-3}$ , which is roughly independent of the crystallization method and Ge

content. The defect density for solid-phase crystallized SiGe films was lower and amounted to  $N_s = 7 \times 10^{17} \text{ cm}^{-3}$ .

- Germanium-rich laser-crystallized poly-SiGe thin films exhibited mostly a broad atypical electric dipole spin resonance (EDSR) signal that was accompanied by a nearly temperature-independent electrical conductivity in the range 20 - 100 K. The analysis of the angle dependence of the EDSR signal suggests that these effects stem from a high metallic-like conductance along grain boundaries.
- Most likely, the origin of the grain boundary conductance is due to dangling-bond defects and not impurities. Metallic-like conductance occurs when the dangling-bond defect density is above a critical value of about  $N_C \approx 10^{18} \text{ cm}^{-3}$ . Below this value the conductance along the grain boundary is significantly reduced but may still exist due to hopping between localized defect states. The appearance of metallic-like conductance for Ge-rich SiGe alloys is viewed as an intrinsic property of Ge compared to Si rather than a property related to the details of the grain boundary structure.
- Laser crystallized poly-Si<sub>1-x</sub>Ge<sub>x</sub> thin films with  $x \geq 0.5$  exhibit optical absorption behavior that is characteristic for disordered SiGe, implying that the absorption occurs primarily at the grain boundaries. A sub-band-gap absorption peak was found for laser-crystallized poly-Si<sub>0.5</sub>Ge<sub>0.5</sub> films that can be attributed to an optical transition between  $D^+/D^0$  dangling-bond states and the conduction band minimum.
- The incorporation of hydrogen into the laser-crystallized poly-SiGe films by remote plasma post-treatment modified remarkably the material properties. On the one hand, it caused a transition from metallic to insulator-like conductance and reduced the ESR and the sub-band-gap absorption signals indicating that dangling-bond defects at the grain boundaries were passivated. On the other hand, it reduced the photoconductivity signal pointing to the formation of some new electrically active defects. It is suggested that these defects might be aggregated  $\text{H}_2^*$  complexes known as platelets.

## 6 References

- [1] M. Lee and S.-J. Moon, *J. Appl. Phys.* **88**, 4994 (2000).
- [2] P. Lengsfeld, Dissertation, Technische Universität Berlin (2001).
- [3] K. Ishikawa, M. Ozawa, C.-H. Oh, and M. Matsumura, *Jpn. J. Appl. Phys.* **73**, 731 (1998).
- [4] J. M. Poate and J. W. Mayer, in *Laser Annealing of Semiconductors* (Academic Press, 1982).
- [5] C. W. White, S. R. Wilson, B. R. Appleton, F. W. Young, and J. Narayan, *J. Appl. Phys.* **51**, 738 (1980).
- [6] D. P. Brunco, M. O. Thompson, D. E. Hoglund, M. J. Aziz, and H.-J. Gossmann, *J. Appl. Phys.* **78**, 1575 (1995).
- [7] R. Reitano, P. M. Smith, and M. J. Aziz, *J. Appl. Phys.* **76**, 1518 (1994).
- [8] S. D. Brotherton, J. R. Ayres, M. J. Edwards, C. A. Fisher, C. Glaister, J. P. Gowers, D. J. McCulloch, and M. Trainor, *Thin Solid Films* **337**, 188 (1999).
- [9] R. B. Bergmann, *Appl. Phys. A* **69**, 187 (1999).
- [10] R. B. Bergmann, G. Oswald, M. Albrecht, and V. Gross, *Sol. Energ. Mat. Sol. C.* **46**, 147 (1997).
- [11] N. Yamauchi and R. Reif, *J. Appl. Phys.* **75**, 3235 (1994).
- [12] S. R. Herd, P. Chaudhari, and M. H. Brodsky, *J. Non-Cryst. Solids* **7**, 309 (1972).
- [13] P. Reinig, B. Selle, F. Fenske, W. Fuhs, V. Alex, and M. Birkholz, *J. Vac. Sci. Technol.* **20**, 2004 (2002).
- [14] R. Lechner, Dissertation, Technische Universität München (2003).
- [15] C. Eisele, Dissertation, Technische Universität München (2002).
- [16] D. E. Aspnes, in *Properties of Crystalline Silicon*, edited by R. Hull (INSPEC, London, 1999), p. 679.
- [17] H. R. Philipp and H. Ehrenreich, in *Semiconductors and Semimetals*, edited by R. K. Willardson and A. C. Beer (Academic Press, 1967), Vol. 3, p. 93.
- [18] J. B. Boyce, P. Mei, R. T. Fulks, and J. Ho, *phys. stat. sol. (a)* **166**, 729 (1998).
- [19] G. Aichmayer, D. Toet, M. Mulato, P. V. Santos, A. Spangenberg, S. Christiansen, M. Albrecht, and H. P. Strunk, *J. Appl. Phys.* **85**, 4010 (1999).
- [20] A. Marmorstein, A. T. Voutsas, and R. Solanki, *J. Appl. Phys.* **82**, 4303 (1997).
- [21] P. Mei, J. B. Boyce, M. Hack, R. Lujan, S. E. Ready, D. K. Fork, and R. I. Johnson, *J. Appl. Phys.* **76**, 3194 (1994).

- [22] P. Mei, J. B. Boyce, M. Hack, R. Lujan, R. I. Johnson, G. B. Anderson, and D. K. Fork, *Appl. Phys. Lett.* **64**, 1132 (1994).
- [23] M. Nerding, R. Dassow, S. Christiansen, J. R. Köhler, J. Krinke, J. H. Werner, and H. P. Strunk, *J. Appl. Phys.* **91**, 4125 (2002).
- [24] P. Lengsfeld, N. H. Nickel, and W. Fuhs, *Appl. Phys. Lett.* **76**, 1680 (2000).
- [25] A. T. Voutsas, A. Limanov, and J. S. Im, *J. Appl. Phys.* **94**, 7445 (1994).
- [26] M. Jyumonji, Y. Kimura, Y. Taniguchi, M. Hiramatsu, H. Ogawa, and M. Matsumura, *Jpn. J. Appl. Phys.* **43**, 739 (2004).
- [27] Y. F. Tang, S. R. P. Silva, and M. J. Rose, *Appl. Phys. Lett.* **78**, 186 (2001).
- [28] F. C. Voogt, R. Ishihara, and F. D. Tichelaar, *J. Appl. Phys.* **95**, 2873 (2004).
- [29] M. Hatano, S. Moon, M. Lee, K. Suzuki, and C. P. Grigoropoulos, *J. Appl. Phys.* **87**, 36 (2000).
- [30] J. S. Im and H. J. Kim, *Appl. Phys. Lett.* **64**, 2303 (1994).
- [31] W. W. Mullins and R. F. Sekerka, *J. Appl. Phys.* **35**, 444 (1964).
- [32] K. M. Bijan and S. R. Morrison, *J. Appl. Phys.* **55**, 3658 (1984).
- [33] A. Broniatowski, *Phys. Rev. B* **36**, 5895 (1987).
- [34] R. Rizk, X. Portier, G. Allais, and G. Nouet, *J. Appl. Phys.* **76**, 952 (1994).
- [35] N. H. Nickel, G. B. Anderson, N. M. Johnson, and J. Walker, *Phys. Rev. B* **62**, 8012 (2000).
- [36] N. M. Johnson, F. A. Ponce, R. A. Street, and R. J. Nemanich, *Phys. Rev. B* **35**, 4166 (1987).
- [37] K. von Maydell and N. H. Nickel, *Appl. Phys. Lett.* **90**, 132117 (2007).
- [38] S. M. Sze, *Physics of Semiconductor Devices* (John Wiley and Sons, New York, 1981).
- [39] F. Secco d'Aragona, *J. Electrochem. Soc.* **117**, 949 (1972).
- [40] A. F. Bogenschütz, *Ätzpraxis für Halbleiter* (Carl Hanser Verlag, München, 1967).
- [41] L. J. van der Pauw, *Philips Tech. Rev.* **20**, 220 (1958).
- [42] W. B. Jackson and N. M. Amer, *Phys. Rev. B* **25**, 5559 (1982).
- [43] M. Weizman, N. H. Nickel, I. Sieber, and B. Yan, in *Mater. Res. Soc. Symp. Proc.* (2005), Vol. 862.
- [44] P. A. Stolk, A. Polman, and W. C. Sinke, *Phys. Rev. B* **47**, 5 (1993).
- [45] Q. Yu, M. O. Thompson, and P. Clancy, *Phys. Rev. B* **53**, 8386 (1996).
- [46] S. Moon, M. Lee, and C. P. Grigoropoulos, *J. Heat Transfer* **124**, 253 (2002).
- [47] S. E. Huq, G. H. Grayer, and P. D. Prewett, *J. Vac. Sci. Technol. B* **15**, 2855 (1997).

- 
- [48] A. H. Jayatissa, F. Sato, N. Saito, K. Sawada, T. Masuda, and Y. Nakanishi, *J. Vac. Sci. Technol. B* **17**, 237 (1999).
- [49] Y. F. Tang, S. R. P. Silva, B. O. Boskovic, J. M. Shannon, and M. J. Rose, *Appl. Phys. Lett.* **80**, 4154 (2002).
- [50] A. A. Evtuka, *Thin Solid Films* **337**, 261 (1999).
- [51] F. C. K. Au, K. W. Wong, Y. H. Tang, Y. F. Zhang, I. Bello, and S. T. Lee, *Appl. Phys. Lett.* **75**, 1700 (1999).
- [52] Z. Shpilman, B. Philosoph, R. Kalish, S. Michaelson, and A. Hoffman, *Appl. Phys. Lett.* **89**, 252114 (2006).
- [53] L. Nilsson, O. Groening, C. Emmenegger, O. Kuettel, E. Schaller, L. Schlapbach, H. Kind, J.-M. Bonard, and K. Kern, *Appl. Phys. Lett.* **76**, 2071 (2000).
- [54] R. H. Fowler and L. Nordheim, in *Proc. Soc. London Ser. A* (1928), Vol. 119, p. 173.
- [55] S. M. Sze, *Semiconductor Devices - Physics and Technology* (John Wiley & Sons, 1985).
- [56] B. R. Chalamala, Y. Wei, and B. E. Gnade, *IEEE Spectrum* **35**, 42 (1998).
- [57] S. C. Lim, H. J. Jeong, Y. S. Park, D. S. Bae, Y. C. Choi, Y. M. Shin, W. S. Kim, K. H. An, and Y. H. Lee, *J. Vac. Sci. Technol. A* **19**, 1786 (2001).
- [58] K. Tshikiyo, *J. Appl. Phys.* **89**, 4917 (2001).
- [59] M. Stutzmann, R. J. Nemanich, and J. Stuke, *Phys. Rev. B* **30**, 3595 (1984).
- [60] A. C. Pineda and S. P. Karna, *J. Phys. Chem. A* **104**, 4699 (2000).
- [61] M. H. Brodsky and R. S. Title, *Phys. Rev. Lett.* **23**, 581 (1969).
- [62] O. H. Roh, W. J. Yun, and J.-K. Lee, *J. Appl. Phys.* **90**, 2786 (2001).
- [63] Y. Yafet, in *Solid State Physics*, edited by F. Seitz and D. Turnbull (Academic Press, New York, 1963).
- [64] N. M. Atherton, *Principles of Electron Spin Resonance* (Ellis Horwood Limited, Chichester, 1993).
- [65] F. Finger, W. Fuhs, G. Beck, and R. Carius, *J. Non-Cryst. Solids* **97-98**, 1015 (1987).
- [66] J.-K. Lee and E. A. Schiff, *J. Non-Cryst. Solids* **114**, 423 (1989).
- [67] M. Stutzmann, R. A. Street, C. C. Tsai, J. B. Boyce, and S. E. Ready, *J. Appl. Phys.* **66**, 569 (1989).
- [68] P. A. Fedders and A. E. Carlsson, *Phys. Rev. B* **37**, 8506 (1988).
- [69] N. H. Nickel, G. B. Anderson, and N. M. Johnson, *Phys. Rev. B* **56**, 12065 (1997).
- [70] N. H. Nickel, A. Yin, and S. J. Fonash, *Appl. Phys. Lett.* **65**, 3099 (1994).
- [71] R. N. Dexter, H. J. Zeiger, and B. Lax, *Phys. Rev.* **104**, 637 (1956).

- [72] M. Wattenbach, C. Kisielowski-Kemmerich, H. Alexander, V. Kveder, T. R. Mchedlidze, and Y. A. Osipyan, *phys. stat. sol. (a)* **158**, K49 (1990).
- [73] K. Schimpf, J. Palm, and H. Alexander, *phys. stat. sol. (a)* **144**, 195 (1994).
- [74] V. Kveder, T. Sekiguchi, and K. Sumino, *Phys. Rev. B* **51**, 16721 (1995).
- [75] D. H. Martin, in *Magnetism in solids* (MIT Press, Cambridge Mass., 1967), p. 138.
- [76] T. Makino and H. Nakamura, *Appl. Phys. Lett.* **35**, 551 (1979).
- [77] P. V. Santos and W. B. Jackson, *Phys. Rev. B* **46**, 4595 (1992).
- [78] N. H. Nickel, N. M. Johnson, and W. B. Jackson, *Appl. Phys. Lett.* **62**, 3285 (1993).
- [79] N. M. Johnson, D. K. Biegelsen, and M. D. Moyer, *Appl. Phys. Lett.* **40**, 882 (1982).
- [80] D. E. Carlson and C. W. Magee, *Appl. Phys. Lett.* **33**, 81 (1978).
- [81] P. G. Shewmon, *Diffusion in Solids* (McGraw-Hill, New York, 1973).
- [82] N. H. Nickel, W. B. Jackson, and J. Walker, *Phys. Rev. B* **53**, 7750 (1996).
- [83] N. H. Nickel and I. E. Beckers, *Phys. Rev. B* **66**, 075211 (2002).
- [84] W. Meyer and H. Neldel, *Z. Tech. Phys.* **18**, 588 (1937).
- [85] H. Overhof and P. Thomas, in *The Meyer-Neldel Rule, Defects and Diffusion Forum*, edited by D. J. Fisher (Trans Tech Publications, Switzerland, 2001), Vol. 192-193, p. 1.
- [86] R. Carius, F. Finger, U. Backhausen, M. Lysberg, P. Hapke, M. Otte, and H. Overhof, in *Mat. Res. Soc. Symp. Proc.* (1997), Vol. 467, p. 283.
- [87] J. Tauc, in *Amorphous and Liquid Semiconductors*, edited by J. Tauc (Plenum, London, 1974).
- [88] J. S. Kline, F. H. Pollak, and M. Cardona, *Helvetica Physica Acta* **41**, 968 (1968).
- [89] A. Davis and N. F. Mott, *Phil. Mag.* **22**, 903 (1970).
- [90] F. B. Ellis, R. G. Gordon, W. Paul, and B. G. Yacobi, *J. Appl. Phys.* **55**, 4309 (1984).
- [91] S. Knief and W. Von Niessen, *Phys. Rev. B* **59**, 12940 (1999).
- [92] F. Demichelis, E. Minetti-Mezzetti, A. Tagliaferro, E. Tresso, P. Rava, and N. M. Ravindra, *J. Appl. Phys.* **59**, 611 (1986).
- [93] M. Oron and G. Sorensen, *Appl. Phys. Lett.* **35**, 782 (1979).
- [94] Z. Guosheng, P. M. Fauchet, and A. E. Siegman, *Phys. Rev. B* **26**, 5366 (1982).
- [95] H. J. Leamy, G. A. Rozgonyi, and T. T. Sheng, *Appl. Phys. Lett.* **32**, 535 (1978).
- [96] S. I. Dolgaev, S. V. Lavishev, A. A. Lyalin, A. V. Simakin, V. V. Voronov, and G. A. Shafeev, *Appl. Phys. A* **73**, 177 (2001).
- [97] M. Y. Shen, C. H. Crouch, J. E. Carey, R. Younkin, E. Mazur, M. Sheehy, and C. M. Friend, *Appl. Phys. Lett.* **82**, 1715 (2003).
- [98] J. Narayan, *J. Appl. Phys.* **52**, 1289 (1981).

- 
- [99] D. E. Hoglund, M. J. Aziz, S. R. Stiffler, M. O. Thompson, J. Y. Tsao, and P. S. Peercy, *J. Cryst. Growth* **109**, 107 (1991).
- [100] L. D. Landau and E. M. Lifshitz, *Hydrodynamics* (Nauka, Moscow, 1988).
- [101] D. K. Fork, G. B. Anderson, J. B. Boyce, R. I. Johnson, and P. Mei, *Appl. Phys. Lett.* **68**, 2138 (1996).
- [102] D. E. Hoglund, M. O. Thompson, and M. J. Aziz, *Phys. Rev. B* **58**, 189 (1998).
- [103] M. J. Aziz and W. J. Boettinger, *Acta Metall. Mater.* **42**, 527 (1993).
- [104] H. Stör and W. Klemm, *Z. anorg. Chem.* **241**, 305 (1939).
- [105] J. P. Dismukes, L. Ekstrom, E. F. Steigmeier, I. Kudman, and D. S. Beers, *J. Appl. Phys.* **35**, 2899 (1964).
- [106] E. Kasper, in *Properties of strained and relaxed silicon germanium* (INSPEC, London, 1995), Vol. 12.
- [107] J. R. Abelson, T. W. Sigmon, K. B. Kim, and K. H. Weiner, *Appl. Phys. Lett.* **52**, 230 (1988).
- [108] F. Maier, M. Riedel, B. Mantel, J. Ristein, and L. Ley, *Phys. Rev. Lett.* **85**, 3472 (2000).
- [109] A. G. Tweet, *Phys. Rev.* **99**, 1182 (1955).
- [110] B. Reed, O. A. Weinreich, and H. F. Matare, *Phys. Rev.* **113**, 454 (1959).
- [111] Y. Hamakawa and J. Yamaguchi, *Jpn. J. Appl. Phys.* **1**, 334 (1962).
- [112] A. K. Fedotov, A. V. Mazanik, T. Figielski, A. Makosa, and Y. M. Ilyashuk, *J. Phys.: Condens. Matter* **14**, 13111 (2002).
- [113] R. K. Mueller and K. N. Maffitt, *J. Appl. Phys.* **35**, 743 (1963).
- [114] T. Gu, J. Qin, C. Xu, and X. Bian, *Phys. Rev. B* **70**, 144204 (2004).
- [115] M. J. Powell and S. C. Deane, *Phys. Rev. B* **48**, 10815 (1993).
- [116] K. Winer, *Phys. Rev. Lett.* **63**, 1487 (1989).
- [117] J. Hubbard, *Proc. R. Soc. Lon. Ser-A* **276**, 238 (1963).
- [118] N. F. Mott, *Metal-Insulator Transitions* (Taylor & Francis, London, 1990).
- [119] N. W. Ashcroft and N. D. Mermin, *Solid State Physics* (Thomson Learning, Toronto, 1976).
- [120] D. F. Holcomb, in *Metal-Insulator Transitions Revisited*, edited by P. P. Edwards and C. N. Rao (Taylor & Francis, 1995), p. 65.
- [121] U. Thomanschefsky and D. F. Holcomb, *Phys. Rev. B* **45**, 13356 (1992).
- [122] H. Fritzsche, *Phil. Mag. B* **42**, 835 (1980).
- [123] P. W. Anderson, *Phys. Rev.* **109**, 1492 (1958).

- [124] G. D. Cody, T. Tiedje, B. Abeles, B. Brooks, and Y. Goldstein, *Phys. Rev. Lett.* **47**, 1480 (1981).
- [125] S. D. Della, C. Reita, G. Conte, F. Galluzzi, and G. Grillo, *J. Appl. Phys.* **67**, 814 (1990).
- [126] W. B. Jackson, N. M. Johnson, and D. K. Biegelsen, *App. Phys. Lett.* **43**, 195 (1983).
- [127] J. R. Weber, A. Janotti, P. Rinke, and C. G. Van de Walle, *Appl. Phys. Lett.* **91**, 142101 (2007).
- [128] H. F. Matare, *Defect Electronics in Semiconductors* (Wiley, New York, 1971).
- [129] M. Stutzmann, D. K. Biegelsen, and R. A. Street, *Phys. Rev. B* **35**, 5666 (1987).
- [130] H. F. Matare, *J. Appl. Phys.* **59**, 97 (1985).
- [131] N. F. Mott and E. A. Davis, *Electronic Processes in Non-Crystalline Materials* (Oxford University Press, Oxford, 1979).
- [132] M. K. Weldon, V. E. Marsico, Y. J. Chabal, A. Agarwal, D. J. Eaglesham, J. Sapjeta, W. L. Brown, D. C. Jacobson, Y. Caudano, S. B. Christman, and E. E. Chaban, *J. Vac. Sci. Technol. B* **15**, 1065 (1997).
- [133] J. M. Zahler, A. Fontcuberta i Morral, M. J. Griggs, H. A. Atwater, and Y. J. Chabal, *Phys. Rev. B* **75**, 035309 (2007).
- [134] C. G. Van de Walle, Y. Bar-Yam, and S. T. Pantelides, *Phys. Rev. Lett.* **60**, 2761 (1988).
- [135] N. H. Nickel, G. B. Anderson, and J. Walker, *Solid State Commun.* **99**, 427 (1996).
- [136] S. Kar, J. I. Pankove, and Y. S. Tsuo, *Appl. Phys. Lett.* **59**, 718 (1991).
- [137] N. M. Johnson, C. Herring, and C. G. Van de Walle, *Phys. Rev. Lett.* **73**, 130 (1994).
- [138] S. Zafar and E. A. Schiff, *Phys. Rev. B* **40**, 5235 (1989).
- [139] W. B. Jackson and S. B. Zhang, in *Advances in Disordered Semiconductors*, edited by H. Fritzsche (World Scientific, Singapore, 1990), Vol. 3.
- [140] S. B. Zhang and W. B. Jackson, *Phys. Rev. B* **43**, 12142 (1991).
- [141] N. M. Johnson, C. Herring, C. Donald, J. Walker, G. B. Anderson, and F. Ponce, *Mat. Sci. Forum* **83-87**, 33 (1992).
- [142] N. H. Nickel, N. M. Johnson, and J. Walker, *Phys. Rev. Lett.* **75**, 3720 (1995).
- [143] C. G. Van de Walle, P. J. H. Denteneer, Y. Bar-Yam, and S. T. Pantelides, *Phys. Rev. B* **39**, 10791 (1989).
- [144] S. K. Estreicher, M. A. Roberson, and D. M. Maric, *Phys. Rev. B* **50**, 17018 (1994).

---

## List of abbreviations

AFM	atomic force microscopy
a-SiGe	amorphous silicon germanium
a-SiGe:H	hydrogenated amorphous silicon germanium
at. %	atomic percent
c-Si	crystalline silicon
c-Ge	crystalline germanium
D	deuterium
EDSR	electric dipole spin resonance
EDX	energy dispersive X-ray
ESR	electron spin resonance
Ge	germanium
H	hydrogen
LC-SiGe	laser-crystallized silicon germanium
$\mu\text{c-Si}$	microcrystalline silicon
Mo	molybdenum
PDS	photothermal deflection spectroscopy
Poly-SiGe	polycrystalline silicon germanium
SEM	scanning electron microscopy
Si	silicon
$\text{Si}_{1-x}\text{Ge}_x$	silicon germanium alloy with a germanium atom fraction x (mostly x is simply referred to as germanium content)
SIMS	secondary ion mass spectrometry
SPC	solid phase crystallization
TEM	transmission electron microscopy

## List of author publications

- M. Weizman, N. H. Nickel, I. Sieber, W. Bohne, J. Röhrich, E. Strub, and B. Yan, Phase segregation in laser crystallized polycrystalline SiGe thin films, *Thin Solid Films* **487**, 72 (2005).
- M. Weizman, N. H. Nickel, I. Sieber, and B. Yan, Formation of a miscibility gap in laser-crystallized poly-SiGe thin films, *Mater. Res. Soc. Symp. Proc.* **862** (2005).
- M. Weizman, N. H. Nickel, I. Sieber, B. Yan, Successive segregation in laser-crystallized poly-SiGe thin films, *J. Non-Cryst. Solids*, **352**, 1259 (2006).
- N. H. Nickel, M. Weizman, I. Sieber, B. Yan, Influence of compositional and structural changes on hydrogen bonding in silicon and silicon–germanium alloys, *J. Non-Cryst. Solids*, **352**, 1037 (2006)
- M. Weizman, N. H. Nickel, I. Sieber, B. Yan, Laser-induced self organization in silicon-germanium thin films, *J. Appl. Phys.* **103**, 093536 (2008)
- M. Weizman, N. H. Nickel, I. Sieber, B. Yan, K. Fostiropoulos, Laser-induced self organization of silicon-germanium hillocks for field emission displays, to be published in *phys. stat. sol.*

---

## Acknowledgments

I would like to express my thanks to all the people who helped me prepare this thesis and encouraged me, each in his own way, through the last three years:

**Dr. Norbert H. Nickel** for assigning me this fascinating topic and guiding me skillfully through the different stages of this study. He provided me with constructive ideas and suggestions while at the same time allowing me the freedom to pursue my own tendencies. His deep understanding of solid-state physics and hydrogen related issues inspired me in my endeavors. I am also grateful for his instructions in how to prepare a scientific manuscript.

**Prof. Dr. Michael Kneissl** who showed interest in this study and agreed to be the second evaluator.

**Prof. Dr. Walther Fuhs** for supporting my research and helping me to get a Ph.D scholarship.

**Prof. Dr. Bernd Rech** for encouraging cooperation between the members of SE1 and creating a pleasant work atmosphere.

**Lars-Peter Scheller** with whom I greatly enjoyed collaborating on the electrical characterization of the laser-crystallized SiGe films. His enthusiasm and sharp research instincts made our discussions extremely fruitful. I am also in debt for his effort to translate and correct some of the text in this thesis

**Ekaterina Terukova** with whom I collaborated on the optical characterization of the SiGe samples with PDS. The high motivation and interest she showed in this research was inspiring.

**Ina Sieber** who performed a great amount of EDX and SEM measurements on the SiGe samples. I am grateful for the exhausting work she did, which is a major part of the results presented in this thesis.

**Dr. Baojie Yan** from United Solar Systems Corp. in the USA for providing the a-SiGe:H layers used as the starting material for the crystallization experiments and for always being prepared to supply additional samples at short notice.

**Dr. Wolfgang Bohne, Dr. Jörg Röhrich, and Dr. Erik Strub** for conducting and analyzing the ERDA measurements on the amorphous SiGe samples.

**Dr. Klaus Lips** who pointed out some critical issues concerning ESR measurements and their interpretation. His input improved this part of the thesis considerably.

**Benjamin Gorka** with whom it was a pleasure to work on hydrogen plasma treatments.

**Pinar Dogan** for being always prepared to help. Our cooperation on the fabrication of solar cells rewarded me with some food for thought.

**Dr. Christian Schubert** for assisting me with many technical issues

**Carola Klimm** for SEM measurements

**Kerstin Jacob** who assisted me with etching and surface cleaning experiments

**Dr. Iris Didschuns** for helping me with the LABVIEW program

**Martin Muske** for helping me with ellipsometry measurements.

**Erhard Conrad** for assisting me with the deposition of some SiGe films

**Stefan Common** for his pleasant company and assistance in correcting texts in German.

**Marion Krusche** for helping me with administrative matters, which allowed me to focus on my scientific work.

**Gerhard Winkler and Andreas von Kozierowski** for technical support.

**Dr. Bert Stegemann, Dr. Rolf Stangl, Jan Behrends, Dr. Christiane Becker** for making the Wednesday running activity such a joyful event.

**All the other members of SE1 in HMI** for a pleasant work atmosphere.

**Deutsche Bundesstiftung Umwelt (DBU) and my instructor Christiane Grimm** for the financial support and the wonderful annual meetings which gave me an awareness of many burning environmental issues.

**Elke Schmid** for her support especially during the last stage of writing this thesis.

**Noa Schmid**, my daughter, who fills my life with joy and happiness.

**Yitzhak and Janet Weizman**, my parents, who taught me faith and love. An extra thank you goes to my mother who went over all my manuscripts and corrected the grammar and spelling mistakes.